AN ABSTRACT OF THE DISSERTATION OF

Andrea M. Balbas for the degree of Doctor of Philosophy in Geology presented on May 5, 2016.

Title: Application of Cosmogenic Nuclides and Argon Geochronology to Paleoclimate, Paleomagnetism, and Paleohydrology

Abstract approved: ____

Peter U. Clark

This dissertation uses argon geochronology and cosmogenic nuclide surface exposure dating methods to address three research questions. The first question concerns a geomagnetic instability recorded in lava flows on the island of Floreana in the Galapagos Archipelago. Changes in the Earth's magnetic field (intensity and orientation) occur frequently throughout geologic time for reasons not yet fully understood. Accurately dating these changes is important because these events provide critical stratigraphic markers in many natural archives, and constraints on the timing of geomagnetic change help better our understanding of the geodynamo. The lava flow on Floreana records an 86% reduction in field strength and intermediate virtual geomagnetic pole (VGP) orientations. Our age determination of 925.7 ± 4.6 ka (2σ; n = 6; Mean Squared Weighted Deviation [MSWD] = 1.23) indicates that this flow, and the flows, associated with it that record nearly identical VGP's, record the Santa Rosa Excursion. We confirm that this site records the second reported non-marine evidence of this geomagnetic excursion. Our age is in agreement with sediment records, which indicate this event spanned 3 kyrs. The Santa Rosa

Excursion can now be characterized as a global short-lived geomagnetic anomaly associated with an 86% reduction (relative to modern day) in field strength in equatorial regions. Similarities between the Santa Rosa and Laschamp excursions illustrate that such events can occur when the geomagnetic field is either in its reversed or normal polarity state.

The second research question addresses the timing of the most recent polarity transition of Earth's magnetic field. The Matuyama-Brunhes (M-B) transition is the most well-studied of all polarity transitions however it's timing remains in debate. A ~10 kyrs mismatch between volcanic and sedimentary archives that record the reversal have been reported. Important geodynamic insights can be gained by examining the structure of a reversing field through time, and the reliability of such studies requires accurate and precise timing of geomagnetic change. We use argon geochronology to date 13 Tahitian lava flows known to record the M-B reversal. A reconciliation between our new ages and those from previous literature from sedimentary and volcanic archives resolves this apparent temporal mismatch and suggests ~35 kyrs of instability and millennial to centennial timescale changes in VGP orientations prior to the Brunhes chron. This new illustration of the structure of a reversing field through time offers new insights into the short precursor history of a reversing field and the rapid -- if not erratic -- changing field dynamics during periods of low-dipole intensity.

The final research question involves establishing the timing of intermittent catastrophic drainage of Glacial Lake Missoula in Montana and the associated large-scale flooding across the Columbia Basin and down the Columbia River to the Pacific

Ocean during the last ice age. During the period from ~22,000 to ~13,000 years ago, there were perhaps 100 such flooding events that each lasted perhaps several weeks, with the amount of water in each flood being equivalent to ~20 times all of the world's river flow combined. Surface exposure ages of boulders deposited by such floods at key geomorphic features can be used to determine flood routing, timing, and magnitude. This data may also suggest a source region of floods through time and help constrain the timing of Okanogan Lobe retreat. Eleven new site ages for flood related geomorphic features reveal the interplay between the Cordilleran Ice Sheet and the megafloods. We show that a large megaflood occurred at ~17.2 ka and traveled through an open northern Columbia River throughway before the advance of the Okanogan Lobe and impoundment of Glacial Lake Columbia. Okanogan Lobe retreat occurred between 14.0 to 14.8 ka and floods that occurred after Okanogan retreat were not as large as those before blockage of the northern Columbia. The relatively late retreat of the Okanogan Lobe as compared to the Puget Lobe may reflect independent controls on ice-sheet behavior. Radiocarbon ages indicating the minimum age of human occupation of the Pacific Northwest of the United States in combination with our most recent site ages suggest humans may have witnessed some of the youngest megafloods, the dramatic character of which likely influenced their oral traditions.

Application of Cosmogenic Nuclides and Argon Geochronology to Paleoclimate, Paleomagnetism, and Paleohydrology

by
Andrea M. Balbas

A DISSERTATION

submitted to

Oregon State University

in partial fulfillment of
the requirements for the
degree of

Doctor of Philosophy

Presented May 5, 2016
Commencement June 2016

Doctor of Philosophy dissertation of Andrea M. Balbas presented on May 5, 2016

APPROVED:

Major Professor, representing Geology

Dean of the College of Earth, Ocean, and Atmospheric Sciences

Dean of the Graduate School

I understand that my dissertation will become part of the permanent collection of Oregon State University libraries. My signature below authorizes release of my dissertation to any reader upon request.

Andrea M. Balbas, Author

ACKNOWLEDGEMENTS

While no family is perfect, my family certainly got the big stuff right. I know the power of kindness, empathy, respect, dedication, courage and love. This is in no small part due to the various examples set by the amazing, spirited, compassionate, empathetic, generous, passionate and steadfast members of my family. There is not a wuss among them. To them, I owe a million thanks. To my baby sister Erika, thanks for always being my biggest fan and never questioning my need to rise-up. You will always be my pot-bellied, round-faced, sweet baby girl. I love you from the beginning to always. To my protective big sister Jennifer for teaching me the power of loyalty. To my Mom for always telling me that I could do anything and actually meaning it. To my Dad for always telling me, “where there is a will, there is a way, baby” and actually meaning it. To my Uncle Paul for taking me on vacation every summer and allowing me to take 20 minutes to pick out a candy bar and never getting mad no matter how many times I asked, “Why?” To my sweet Auntie Sharon who always made me stop and ask myself, “Well, how would you feel? If that were you, how would you feel?” To my perfect cousins Tony and Blue who never shied away from being my partners in science and adventure no matter how dangerous and ill-advised such childhood explorations can be. To my dogs Bubba and Minerple who showed me that my fierceness was just as valuable as my kindness. To my kitty cats, for all the love.

To my patient husband Kevin for helping me and believing in me when I felt that no one could or should. Thank you sooooo much for all your help and support.

To Christene and Birgit for being friends that always wished for my peace and fulfillment.

To Peter, well here we are. There really are no words. I assume you know that you changed my life. I assume you know that among all your many gifts, it is your kindness I treasure most. I assume you know that I'm amazed I found you of all the many advisers possible. Thanks for always being upfront and honest. Thanks for your loyalty, support, and guidance. You are my greatest champion, thank you for being a great warrior with me and for me. I would charge into battle along side you any day and you must realize that is my highest compliment. To Jorie and Luca-baby thanks for all the joy and love.

To Ed, hi Ed. I have no idea why you are always looking out for me, but I will never forget it as long as I live. You make the world a better place by going to the front lines and speaking up. You might think such activity is inconsequential but it is what true inclusiveness is all about. You make the world a better place, Ed. I'm proud to know you. Just the sight of you makes me smile.

To Anthony, I bet you wish you ran long and fast at first sight of me. I don't blame you. At every turn, I asked of you and at every turn, you were there to give. Your positive optimistic attitude makes good research possible. Your scientific enthusiasm is infectious. While your stoic Dutch exterior may fool some people, I know you have a heart of gold. Even when your back is straight and you are yelling at me, I know your intentions are always the very best. I appreciate the time you have taken to share with me your superior technical understanding of argon geochronology, but nothing has been more valuable than your belief in me as a scientist. Thank you for being my Samwise Gamgee the Brave.

To Joe, well you saved me Joe. You saved me. I will never forget the look on your face when I informed you one day after my orals that I would be taking my masters and leaving academia. I still feel bad, as it seemed to take years off your life. Those emails you sent and your unyielding support of me is why I made it to this point. Without your time and care and thoughtfulness in that extremely difficult time, I would not have made it. Thanks for being so enthusiastic about the geomagnetic field and talking crazy science ideas with me. It's the best, just like you.

I sincerely could not imagine having a better committee. Every single one of you is irreplaceable. I don't know how I got so lucky.

To Shaun Marcott and Aaron Barth for always being supportive, level-headed, generous and acutely entertaining. To Joshua Cuzzone for always holding me up when I don't want to stand.

To all my buddies in Quat Tea thanks for the support. Brendan, you're my ace in the hole. Nilo Bill, Jon Edwards, Thomas Bauska and Christo thanks for laughing with me when I really needed it.

To all my buddies in the argon lab including Dan Miggins. Susan Schnur, Daniel Heaton, and Julie Klath, you buoyed me when analytical times were toughest (which is really saying something).

To all the ladies that keep me afloat Henri Seville, Stacey Schulte, Melinda Jensen, Renee Freeman, Julia Rosen, Ado Mucek, where would I be without you?

To Dave Graham, Bob Duncan, Adam Kent, Frank Tepley, Anita Grunder and John Dilles for all the times you stopped in the hallway to help me, it was more appreciated than you know.

To Vic Baker, Jim O'Connor, Dennis Kent, Rob Coe, Robert Butler, Bruce Bjornstad and Marco Vaca, without your generous souls, I'd have been dead in the water. You were all so patient with me through difficult learning curves. You didn't need to help me, but you did, and it made a world of difference. I will never forget your kindness. Vic your infectious enthusiasm for all things megaflood related is inspirational and you have always been so generous with your time, I cannot thank you enough. Your faith in me has pushed me forward. James E. O'Connor, I went in the field with you so I might share my sample sites with one of few people I thought may appreciate them as much as I do. On that trip, I hoped I might find a postdoctoral adviser but found a best buddy instead. What a wonderful surprise. You amaze me at every turn. Dennis Kent, your support of me has been unyielding since my undergraduate studies and I love working with you. Robert Coe, your patience has been remarkable, thank you for always being there. Robert Butler, who gives someone expensive field equipment and teaches them how to use it after only a brief interaction? You do! It is still shocking to me. I am in your debt forever. Bruce Bjornstad, thank you so much for being so generous with your immense field knowledge, and entertaining travel time in the field. Thank you to Marco Vaca for your outstanding fieldwork.

Thank you to Marc Caffee and the Purdue Rare Isotope Measurement Laboratory for support of our Missoula Flood project including multiple measurements from the seed program.

To my undergraduate mentor Dr. Hannes Brueckner who looked me straight in the eye and said, “Well, you have the creative portions of science down, now you just need to work on the rest of it.” I hope I made you proud.

CONTIRBUTION OF AUTHORS

Chapter 2—Anthony A. P. Koppers and Dennis V. Kent oversaw measurement campaigns for the $^{40}Ar/^{39}Ar$ analyses and paleomagnetic analyses respectively. Kevin Konrad assisted with field mapping, sample selection and project design. Peter U. Clark assisted with project design. All authors provided input for the manuscript.

Chapter 3—Anthony A. P. Koppers and Robert S. Coe oversaw measurement campaigns for the $^{40}Ar/^{39}Ar$ analyses and paleomagnetic analyses respectively. Peter U. Clark assisted with project design and data interpretation. Brendan T. Reilly and Joseph Stoner assisted with data interpretation. Kevin Konrad assisted with field mapping, sample selection and project design. All authors provided input for the manuscript.

Chapter 4—Aaron Barth assisted with sample preparation including processing samples for $^{10}Be/^{9}Be$ measurements. Peter U. Clark assisted with project design and data interpretation. Jorie Clark assisted with proposal preparation. James E. O'Connor and Victor R. Baker assisted with project design, sample selection, sampling boulders and data interpretation. Kevin Konrad assisted with field mapping, sample selection and boulder sampling. Marc Caffee oversaw measurement campaigns for ^{10}Be analyses. All authors provided input for the manuscript.

TABLE OF CONTENTS

TABLE OF CONTENTS (Continued)

LIST OF FIGURES

LIST OF APPENDICES

LIST OF APPENDIX FIGURES

LIST OF APPENDIX FIGURES (Continued)

LIST OF APPENDIX FIGURES (Continued)

LIST OF APPENDIX TABLES

For my grandmas, Geneva and Rose

Application of Cosmogenic Nuclides and Argon Geochronology to Paleoclimate, Paleomagnetism, and Paleohydrology

Chapter 1

Introduction

1.1 Forward

The realization that decay and spallagenic products from various chemical constituents can be used to constrain the timing of natural processes recorded in several natural archives has dramatically advanced our understanding of many climatic, volcanic, geomagnetic, and hydrologic processes (Aldrich and Nier, 1948; Gentner et al., 1953; Kurz, 1986; Merrihue and Turner, 1966; Pahl et al., 1950). Subsequent advances in scientific methodology have resulted in the now widely used geochronological tools of argon geochronology and cosmogenic nuclide surface exposure dating. The accuracy and precision of these methods have improved with technological advancement and currently report ages in good agreement with astrochronologically tuned records (Balbas et al., 2016; Laj et al., 2014; Lascu et al., 2016). Age determinations constraining glacier retreat, basalt formation, and erosional processes have been particularly valuable for resolving events that occurred in the Quaternary largely because natural archives associated with this period are better preserved and more accessible. For example, a compilation of surface exposure dated boulders associated with globally distributed moraines suggests that significant climate change can happen on centennial to millennial timescales and global glacial retreat is likely associated with increased greenhouse gas concentrations in the atmosphere (Shakun et al., 2015). With respect to geomagnetic processes, ^{40}Ar/^{39}Ar age determinations of lava flows associated with paleomagnetic anomalies (polarity reversals and excursions) have placed better constraints on important stratigraphic markers (Singer, 2014), and improved our understanding of geodynamic processes (Valet and Fournier, 2016). Such successes underscore the capacity for these methods to resolve the timing of important natural processes and improve our understanding of the mechanisms that control them.

Climate variability plays a large role on the evolution of human civilizations (Büntgen et al., 2011; D'Andrea et al., 2011). In particular, abrupt climate change has likely provoked civilization decline in the past (Zhang et al., 2007). Our understanding of the forcings and feedbacks of past climate systems improves with increases in the temporal resolution of climate records. Our ability to characterize past and future climate is limited by our understanding of the timing of climatic events. Glaciers are particularly sensitive to climate change and their retreat is considered to be a robust signal of climate warming (Shakun et al., 2015). Better constraints on the timing of glacier retreat and the hydrologic processes associated with glacier retreat help us understand past climate warming (Shakun et al., 2015).

Earth's magnetic field is relied upon by various organisms for migration as well as human navigation (Jonkers et al., 2003; Kirschvink et al., 2013; Stern, 2002; Yilmaz et al., 2010). The geomagnetic field also shields our planet's organisms and society's modern electronics from cosmic ray bombardment (Gosse and Phillips, 2001). Yet questions remain regarding the processes in the geodynamo that give rise to changes in field strength and orientation. Our current understanding of geomagnetic change is largely derived from natural records of its past behavior and dependent on how well we define the timing of such behavior. Basaltic lava flows with abundant K are excellent candidates for age determinations using ^{40}Ar/^{39}Ar geochronology. Such lava flows also record the character of Earth's magnetic field (strength and orientation) upon formation. Well-dated sequences of such flows are excellent natural archives of geomagnetic change, which offer a series of "snap shots" of the geomagnetic field through time. Recent improvements to the precision and accuracy of ^{40}Ar/^{39}Ar geochronology offer improved temporal resolution of the structure of a reversing field, especially when combined with data derived from sedimentary archives. Reconciliation of data from both archives puts valuable constraints on the timing of paleomagnetic events and allows for their more accurate placement within the geomagnetic instability timescale.

1.2 Project objectives

This dissertation uses advancements in geochronology to better understand the timing and processes associated with significant paleomagnetic change, climate transitions associated with the last ice age, and hydrologic processes related to the retreat of the Cordilleran ice sheet. Specifically, I use ^{40}Ar/^{39}Ar geochronology to address two questions related to recent changes in Earth's magnetic field. I also use surface exposure dating with cosmogenic nuclides to better constrain the history of one of Earth's most dramatic events – the late Pleistocene Missoula floods.

In Chapter 2, we investigate the timing and extent of a geomagnetic anomaly recorded in basaltic lava flows on the island of Floreana in the Galapagos

Archipelago. An initial K/Ar age determination of 720 ± 400 ka (Cox and Dalrymple, 1966) was reported for a flow associated with this anomaly. Intermediate virtual geomagnetic pole orientations recorded at this site have led some to suggest that it records the Matuyama-Brunhes reversal (Gromme et al., 2010). More recent studies highlight the paleomagnetic significance of the event recorded in these flows, which indicate it had a field strength reduction of 86% as compared to the modern day field (Wang and Kent, 2013). Given the large error of the initial age determination on this flow, new analyses are required to determine the placement of this event within the geomagnetic instability timescale. Here we seek to define the timing of this event and place this large decrease in field strength within temporal perspective to better define its paleomagnetic significance.

In Chapter 3, we explore the timing and structure of Earth's most recent geomagnetic polarity transition. The mechanisms that provoke and govern the seemingly stochastic occurrence of geomagnetic reversals are not well understood. The transition from the Matuyama reversed chron to the Brunhes normal chron is perhaps the most well studied of all past reversals of Earth's magnetic field, in large part because it is the most recent and thus well-preserved in several types of natural archives (e.g. sediment cores, ice cores, lava flows, speleothems, loess) (Lascu et al., 2016; Raisbeck et al., 2006; Valet and Fournier, 2016; Yang et al., 2010). Yet the timing of this event still remains uncertain with many suggesting that the apparent mismatch between ages recorded in sediment archives as compared to those in volcanic archives results from an erroneous normalizing standard age or decay constant used in $^{40}Ar/^{39}Ar$ geochronology.

Chapter 3 seeks to provide new age determinations on the Matuyama-Brunhes reversal as recorded by several lava flows from the Punarru Valley, Tahiti. We aim to reconcile the apparent age discrepancy between these natural archives to better constrain the timing of the event and the structure of the reversing field. We seek new insights regarding the geodynamics associated with this significant paleomagnetic event. The methodologies used for this project include multiple incremental heating ^{40}Ar/^{39}Ar analyses on groundmass separated from several lava flows known to bracket the M-B reversal.

In Chapter 4 we examine the timing of the late Pleistocene megafloods, also known as the Missoula Floods, which are the largest floods known from the geologic record (Baker, 1978; Benito and O'Connor, 2003; Bretz, 1923, 1928; O'Connor and Baker, 1992). The late Pleistocene megafloods were caused by the rapid draining of Glacial Lake Missoula. Held back by an ice dam that failed intermittently, the rapid draining of Glacial Lake Missoula caused upwards of 89 megaflood events (Atwater, 1986). The point of release was northeast of Spokane, Washington, from which point floodwaters traveled southwest to the Columbia River and ultimately into the Pacific Ocean (Pardee, 1942). We aim to define the chronology and routing of the megafloods that flowed over large portions of the Pacific Northwest and to better constrain the timing of Cordilleran Ice Sheet deglaciation. The methodologies used to complete this project are geologic fieldwork/mapping and surface exposure dating of boulders deposited by several megaflood events.

1.3 References

Aldrich, L. T., and Nier, A. O., 1948, Argon 40 in potassium minerals: Physical Review, v. 74, no. 8, p. 876.

Atwater, B. F., 1986, Pleistocene glacial-lake deposits of the Sanpoil River Valley, northeastern Washington: USGPO.

Baker, V. R., 1978, Paleohydraulics and hydrodynamics of scabland floods, in Baker, V. R., and Nummedal, D., eds., The Channeled Scabland: Washington, D.C. , National Aeronautical Space Administration Planetary Geolology Program, p. 59-70.

Balbas, A., Koppers, A. A., Kent, D. V., Konrad, K., and Clark, P. U., 2016, Identification of the short-lived Santa Rosa geomagnetic excursion in lavas on Floreana Island (Galapagos) by 40Ar/39Ar geochronology: Geology, p. G37569. 37561.

Benito, G., and O'Connor, J. E., 2003, Number and size of last-glacial Missoula floods in the Columbia River valley between the Pasco Basin, Washington, and Portland, Oregon: Geological Society of America Bulletin, v. 115, no. 5, p. 624-638.

Bretz, J. H., 1923, The Channeled Scabland of the Columbia Plateau: Journal of Geology, v. 31, p. 617-649.

-, 1928, Channeled Scabland of eastern Washington: Geographical Review, v. 18, p. 446-477.

Büntgen, U., Tegel, W., Nicolussi, K., McCormick, M., Frank, D., Trouet, V., Kaplan, J. O., Herzig, F., Heussner, K.-U., and Wanner, H., 2011, 2500 years of

European climate variability and human susceptibility: Science, v. 331, no. 6017, p. 578-582.

Cox, A., and Dalrymple, G. B., 1966, Palaeomagnetism and potassium-argon ages of some volcanic rocks from the Galapagos Islands.

D'Andrea, W. J., Huang, Y., Fritz, S. C., and Anderson, N. J., 2011, Abrupt Holocene climate change as an important factor for human migration in West Greenland: Proceedings of the National Academy of Sciences, v. 108, no. 24, p. 9765-9769.

Gentner, W., Präg, R., and Smits, F., 1953, Argonbestimmungen an kalium-mineralien: II. Das alter eines kalilagers im unteren oligozän: Geochimica et Cosmochimica Acta, v. 4, no. 1, p. 11-20.

Gosse, J. C., and Phillips, F. M., 2001, Terrestrial in situ cosmogenic nuclides: theory and application: Quaternary Science Reviews, v. 20, no. 14, p. 1475-1560.

Gromme, S., Mankinen, E. A., and Prévot, M., 2010, Time-averaged paleomagnetic field at the equator: Complete data and results from the Galapagos Islands, Ecuador: Geochemistry, Geophysics, Geosystems, v. 11, no. 11.

Jonkers, A. R., Jackson, A., and Murray, A., 2003, Four centuries of geomagnetic data from historical records: Reviews of Geophysics, v. 41, no. 2.

Kirschvink, J. L., Jones, D. S., and MacFadden, B. J., 2013, Magnetite biomineralization and magnetoreception in organisms: a new biomagnetism, Springer Science & Business Media.

Kurz, M. D., 1986, Cosmogenic helium in a terrestrial igneous rock.

Laj, C., Guillou, H., and Kissel, C., 2014, Dynamics of the earth magnetic field in the 10–75 kyr period comprising the Laschamp and Mono Lake excursions: New results from the French Chaîne des Puys in a global perspective: Earth and Planetary Science Letters, v. 387, p. 184-197.

Lascu, I., Feinberg, J. M., Dorale, J. A., Cheng, H., and Edwards, R. L., 2016, Age of the Laschamp excursion determined by U-Th dating of a speleothem geomagnetic record from North America: Geology, v. 44, no. 2, p. 139-142.

Merrihue, C., and Turner, G., 1966, Potassium-argon dating by activation with fast neutrons: Journal of Geophysical Research, v. 71, no. 11, p. 2852-2857.

O'Connor, J. E., and Baker, V. R., 1992, Magnitides and implications of peak discharges from glacial Lake Missoula: Geological Society of America Bulletin, v. 104, p. 267-279.

Pahl, M., Hiby, J., Smits, F., and Gentner, W., 1950, Mass-Spectrometric Determinations of Argon in Potassium Salts: Zeitschrift fuer Naturforschung (West Germany) Divided into Z. Nautrforsch., A, and Z. Naturforsch., B: Anorg. Chem., Org. Chem., Biochem., Biophys., v. 5.

Pardee, J. T., 1942, Unusual currents in glacial lake Missoula, Montana: Geological Society of America Bulletin, v. 53, no. 11, p. 1569-1600.

Raisbeck, G. M., Yiou, F., Cattani, O., & Jouzel, J., 2006, ^{10}Be evidence for the Matuyama–Brunhes geomagnetic reversal in the EPICA Dome C ice core. Nature, 444(7115), 82-84.

Shakun, J. D., Clark, P. U., He, F., Lifton, N. A., Liu, Z., and Otto-Bliesner, B. L., 2015, Regional and global forcing of glacier retreat during the last deglaciation: Nature communications, v. 6.

Singer, B. S., 2014, A Quaternary geomagnetic instability time scale: Quaternary Geochronology, v. 21, p. 29-52.

Stern, D. P., 2002, A millennium of geomagnetism: Reviews of geophysics, v. 40, no. 3.

Valet, J. P., and Fournier, A., 2016, Deciphering Records of Geomagnetic Reversals: Reviews of Geophysics.

Wang, H. P., and Kent, D. V., 2013, A paleointensity technique for multidomain igneous rocks: Geochemistry Geophysics Geosystems, v. 14, no. 10, p. 4195-4213.

Yang, T., Hyodo, M., Yang, Z., Li, H., and Maeda, M., 2010, Multiple rapid polarity swings during the Matuyama-Brunhes transition from two high-resolution loess-paleosol records: Journal of Geophysical Research: Solid Earth, v. 115, no. B5.

Yilmaz, I., Gullu, M., Yilmaz, M., and Dereli, M. A., 2010, Compass roses on the Book of Navigation (Kitab-ı Bahriye): Declination data source for geomagnetic field models: Physics of the Earth and Planetary Interiors, v. 182, no. 3, p. 170-174.

Zhang, D. D., Brecke, P., Lee, H. F., He, Y.-Q., and Zhang, J., 2007, Global climate change, war, and population decline in recent human history: Proceedings of the National Academy of Sciences, v. 104, no. 49, p. 19214-19219.

Chapter 2

Identification of the short-lived Santa Rosa geomagnetic excursion in lavas on Floreana (Galapagos) by $^{40}Ar/^{39}Ar$ geochronology

Andrea Balbas[1], Anthony A.P. Koppers[1], Dennis V. Kent[2,3], Kevin Konrad[1], and Peter U. Clark[1]

[1]College of Earth, Ocean and Atmospheric Sciences, Oregon State University, Corvallis, Oregon 97331, USA

[2]Department of Earth and Planetary Sciences, Rutgers University, Piscataway, New Jersey 08854, USA

[3]Lamont-Doherty Earth Observatory, Columbia University, Palisades, New York 10964, USA

Accepted and Published in Geology

Balbas, A., Koppers, A. A., Kent, D. V., Konrad, K., & Clark, P. U. (2016). Identification of the short-lived Santa Rosa geomagnetic excursion in lavas on Floreana Island (Galapagos) by $^{40}Ar/^{39}Ar$ geochronology. *Geology*, *44* (5), 359-362.

2.1 Abstract

A set of closely related basaltic lava flows (GA-X) on Floreana Island in the Galapagos Archipelago has a published record of an excursional or transitional direction (virtual geomagnetic pole located at 153.1°E, 54.2°S with $\alpha_{95} = 5.0°$) and a geomagnetic field strength (1.1×10^{22} Am^2) that is only ~14% of the strength of the modern magnetic field (7.8×10^{22} Am^2). The very large age uncertainty of previous dating of a lava flow (G43) from this set, however, has prevented placing this event in the geomagnetic polarity timescale. Here we report highly reproducible and precise ^{40}Ar/^{39}Ar ages on the lava flow that indicate that the distinct geomagnetic excursion is 925.7 ± 4.6 ka (2σ; n = 6; MSWD = 1.23). This shows that this dramatic weakening of the geomagnetic field is associated with the Santa Rosa Excursion instead of the Matuyama-Brunhes polarity reversal. Our high-precision ^{40}Ar/^{39}Ar ages for Floreana provide evidence for the global significance of the Santa Rosa Excursion.

2.2 Introduction

Large geomagnetic field disruptions known as excursions are characterized by reduced field strengths and intermediate magnetic pole locations and have occurred stochastically through geologic time. Understanding such anomalous geomagnetic behavior is important for further refining the geomagnetic polarity time scale (Berggren et al., 1995; Channell et al., 2002; Singer, 2014) as well as unraveling the complexities of the geodynamo, which controls the stability of Earth's magnetic field (Merrill et al., 1996). The age, duration, global distribution, magnitude and mechanism of geomagnetic field excursions, however, remain poorly understood.

Existing age constraints suggest that the Santa Rosa Excursion (SRE) occurred sometime between 920 ka and 935 ka (Singer, 2014). Thus far, it has only been identified in the Santa Rosa rhyolite dome (SRRD) in New Mexico (Doell and Dalrymple, 1966) and in sediment cores from the Philippine Sea (Horng et al., 2002) and the Iceland Basin (Channell et al., 2002). The limited manifestation of this excursion in geological records may result from variable regional changes in the geomagnetic field at the time. Alternatively, the SRE was extremely short-lived and is thus hard to recognize elsewhere, especially in sporadic volcanic successions and low-sedimentation-rate sedimentary sequences. Here we identify a new low-latitude record of the SRE based on our dating of a basaltic lava flows from Floreana Island in the Galapagos Archipelago that was reported (Wang and Kent, 2013) to be characterized by an extremely low geomagnetic field intensity and transitional field directions.

2.2.2 The Geomagnetic Excursion on Floreana Island, Galapagos

Cox and Dalrymple (1966) examined the paleomagnetism and geochronology of basaltic lava flows from Floreana Island. Of the nine sampled sites, five (G37–G41) were assigned to the Brunhes normal polarity chron and four (G42–G45) to the Matuyama reverse polarity chron. Initial K-Ar ages on one of these lava flows (site G43) yielded a mean age of 720 ± 400 ka (Cox and Dalrymple, 1966). Subsequent studies determined that some of these flows have intermediate virtual geomagnetic poles (VGPs), indicating a potential transitional behavior of the geomagnetic field (Rochette et al., 1997; Gromme et al., 2010; Kent et al., 2010). Gromme et al. (2010)

reanalyzed the samples collected by Cox and Dalrymple (1966) and reported tabulated results using a blanket cleaning method (generally alternating fields at 10 mT) from a total of 186 sites from 16 Galapagos Islands, including Floreana. Two of the original four reverse-polarity sites (G44 and G45) were now characterized as having intermediate VGPs and, in conjunction with the nearby reverse polarity sites (G42 and G43), were interpreted as possibly associated with the Matuyama-Brunhes polarity transition (Gromme et al., 2010). Kent et al. (2010) used progressive thermal demagnetization to study 400+ specimens remaining from the Rochette et al. (1997) sample collection and reported a grand average of four Floreana sites (GA78, GA79, GA84, and GA85) with a closely grouped intermediate VGP (153.1°E, 54.2°S, a95 = 5.0°, n = 4). Wang and Kent (2013) subsequently analyzed multiple specimens from these four sites collectively referred to as GA-X using three standard Thellier methods as well as a new multidomain correction method, yielding a paleoinstensity of 4.23 ± 1.29 mT (2s, n = 11) that is only ~14% of the modern-day geomagnetic field strength. The concordant paleointensity lows and excursional directions in four separate lava flows makes it likely that four similar-age eruptions were sampled and that the paleomagnetic results are unlikely a secondary artifact (e.g., lighting strike). The combination of intermediate directions with very low paleointensities in the four GA-X sites is consistent with a record of either a polarity transition or an excursion.

2.3 Methods and Results

We resampled Floreana lava flow GA79 (1.273°S, 90.488°W) described by Rochette et al. (1997) and Kent et al. (2010) that corresponds to site G44 from Cox and Dalrymple (1966) in order to obtain new $^{40}Ar/^{39}Ar$ ages. We verified that we resampled site GA79 by obtaining a paleomagnetic direction from this set of newly collected samples, resulting in an inclination/declination of –30.5°/215.7° (n = 42, a95 = 4.8°) that corresponds to an intermediate VGP located at 151.3°E, 50.6°S nearly identical with the VGP (153.1°E, 54.2°S) for supersite GA-X as reported by Kent et al. (2010). Lava flow GA79 is vertically stratified and varies between 5 m and 7 m in thickness. It consists of a dense, holocrystalline, non-vesicular basalt at its base, grading upward into a finer-grained, oxidized, highly-vesicular basalt; the upper ~1.25 m has a red-colored frothy appearance. In order to test how ^{40}Ar/^{39}Ar age spectra, plateau ages and mean squared weighted deviation (MSWD) statistics vary depending on the physical volcanology of lava flow GA79, we collected nine samples from three vertical flow sections, each spaced ~4 m apart. We distinguish layer A that represents the least-altered, holocrystalline and non-vesicular base of the flow, layer B that represents an intermediately altered and vesicular section, and layer C that represents the frothy fine-grained altered top of the flow. A thin soil horizon overlays the flow in the sampling area, indicating we have captured the full height and top boundary of the flow.

Six samples selected from lava flow GA79 for ^{40}Ar/^{39}Ar geochronology (three from layer A, two from layer B, and one from layer C) were crushed and sieved to a grain size between 106 and 180 mm to avoid the inclusion of phenocrysts and potential xenocrysts. Predominantly crystalline groundmass phases were separated and analyzed in order to directly determine the eruption age of the lava flow and to avoid magmatic crystal residence bias (e.g., Hora et al., 2010) and/or excess 40Ar issues (McDougall and Harrison, 1999). The groundmass was magnetically separated from the mineral phases and acid leached following previously defined methods (Koppers et al., 2011). Pure groundmass was then handpicked under a binocular microscope to remove any remaining alteration and/or adhering pieces of the coarser mineral phases.

When possible, groundmass splits of 15 and 25 mg were analyzed from each sample (Table DR1 in the GSA Data Repository1; see the Data Repository for analytical data) using a multi-collector ARGUS-VI mass spectrometer at Oregon State University (Corvalis, Oregon, USA) outfitted with five 10^{12} Ohm Faraday collectors and one ion-counting CuBe electron multiplier. The ages and uncertainty estimates include corrections for baselines, blanks, irradiation production ratios, radioactive decay, mass fractionation and the multiplier/Faraday collector calibration on mass 36. Ages were calculated using ArArCALC v2.7.0 (Koppers, 2002) with a Fish Canyon Tuff (FCT) sanidine age of 28.201 ± 0.046 Ma (2σ; Kuiper et al., 2008) and a corrected decay constant of $5.530 \pm 0.097 \times 10^{-10}$ yr^{-1} (2σ) as reported by Min et al. (2000). Reproducibility of Alder Creek AC-2 sanidine analyses is excellent with mean ages of 1176.3 ± 3.9 ka and 1184.0 ± 3.9 ka (internal error, 2σ; MSWD = 5.68; n = 132/143) against FCT sanidine age of 28.02 Ma of Renne et al. (1998) and 28.201 Ma of Kuiper et al. (2008), respectively.

The three GA79 intra-flow layers measured gave slightly different ages that are statistically distinguishable, given the high precision achievable by using ARGUS-VI multi-collector mass spectrometry. We suggest that these small age variations are a function of alteration and oxidation, which is greatest in the upper frothy and finer-grained (more glassy) part, whereas the base layer (layer A) is less susceptible due to its higher groundmass crystallinity (a function of slower cooling near the base). Consequently, we define our age using layer A samples (see supplemental document for layers B and C). Three separate samples from layer A (44-Ar-2; 44-Ar-3; 44-Ar-5) were measured twice and produced concordant ages within the 1σ and 2σ confidence intervals (Fig. 2.1). Their age spectra exhibit long plateaus (46%–71%) characterized by radiogenic ^{40}Ar components >50% and 2σ uncertainties <1.4% that range between 9.3 and 11.8 ka (for 15 mg splits) and 7.9–10.2 ka (for 25 mg splits). The low-temperature higher apparent ages are readily explained by ^{39}Ar[k] recoil (e.g., Koppers et al. 2004) and can be related to some remaining submicroscopic alteration in the groundmass samples, even after careful acid-leaching and handpicking. However, the age plateaus show no scatter beyond what is expected from analytical scatter alone, as implied by low MSWD's ranging from 0.7 to 1.4 (n = 5) and 2.4 (n = 1). We conclude that the layer A holocrystalline groundmasses fulfill our quality criteria and display no significant recoil effects in the age plateaus within quoted 2σ uncertainty bounds. Because all six layer A groundmass analyses are extremely reproducible, even at 1σ confidence levels, their overall average age provides us with an eruption age of 925.7 ± 4.6 ka (internal error including the uncertainty on the J-curve, 2σ, n = 6) for lava flow GA79, corresponding to a total of 99 incremental heating steps and yielding a satisfactorily low MSWD of 1.23. The external error on this age is 21.4 ka (2σ), which includes the error on the decay constant and age of the FCT standard. The combined layer A analyses also yield a concordant inverse isochron age (930.7 ± 6.4 ka) with an intercept of 291.3 ± 3.8 (slightly below the atmospheric value of 295.5) and a

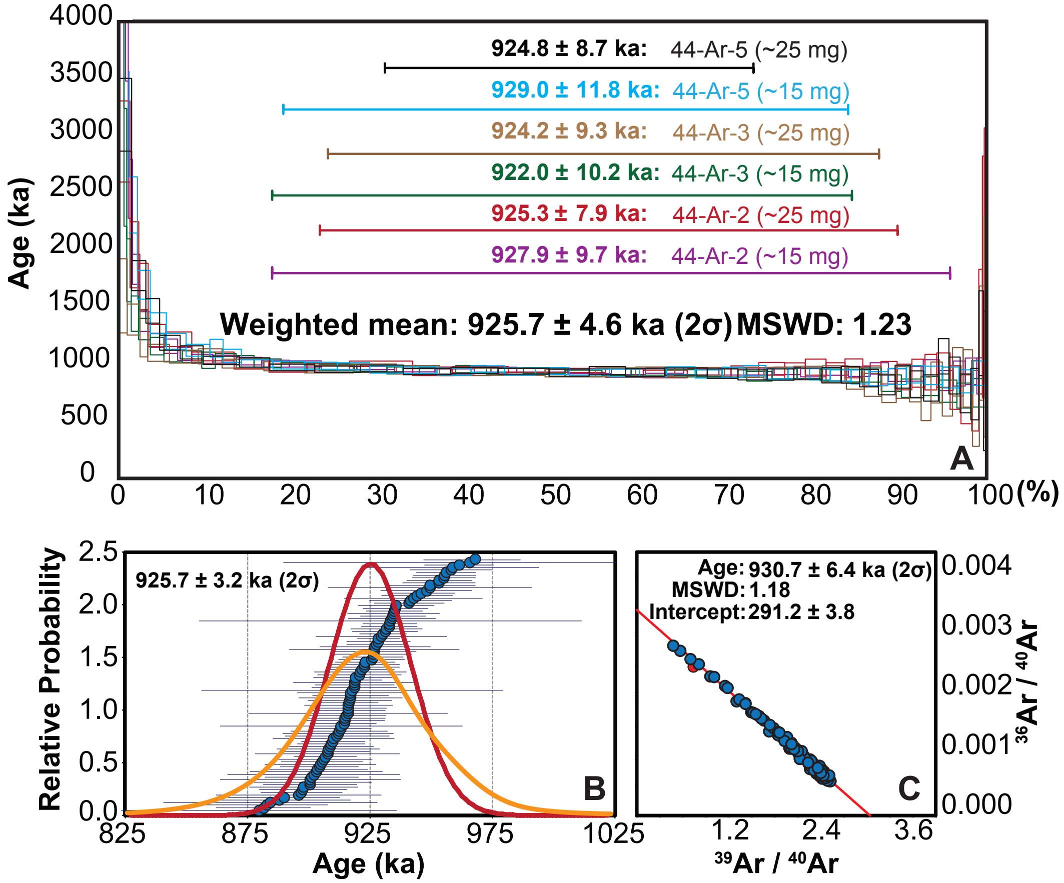

Figure 2.1. ^{40}Ar/^{39}Ar age results for the layer A basalt samples. A: Stacked ^{40}Ar/^{39}Ar incremental heating plateau. Ages for the individual samples and splits are indicated along with the weight of sample analyzed. B: Ideogram of all selected incremental heating steps. The red line represents a normal distribution curve and the orange line represents a probability density curve based on the results. C: Inverse isochron for all selected incremental heating steps (blue circles). Red circle represents the ‘total fusion’ value for all combined steps.

concordant ideogram age (925.7 ± 3.2 ka), reinforcing the high quality layer A analyses.

2.4 Discussion

2.4.1 Age of the Santa Rosa Excursion

Chronological and paleomagnetic studies of the SRRD (Santa Rosa Dome I) in New Mexico began as early as 1966 (Doell and Dalrymple, 1966). For ease of comparison to these previous studies, we have recalibrated all $^{40}Ar/^{39}Ar$ ages to the FCT sanidine age of 28.201 Ma (Kuiper et al., 2008) and the Min et al. (2000) decay constants, and we report all ages with an uncertainty of 2σ. Intermediate VGPs recorded in the SRRD were first dated to 922 ± 56 ka using K-Ar methodology and initially interpreted as recording the termination of the Jaramillo normal polarity chron (Doell and Dalrymple, 1966; Doell et al., 1968). Using $^{40}Ar/^{39}Ar$ total fusion analysis of single sanidine crystals, Spell and Harrison (1993) re-analyzed this flow to provide an inverse isochron age of 925 ± 8 ka. Izett and Obradovich (1994) also used total fusion analyses of single sanidine crystals to provide an age of 938 ± 34 ka for the SRRD, which they tentatively distinguished from the Jaramillo reversal. Singer et al. (1999) first confirmed an older age for the termination of the Jaramillo and then took the mean of all previously published Santa Rosa ages, obtaining an age of 922 ± 12 ka, confirming that the SRRD was significantly younger than the termination of the Jaramillo and must have formed during a distinct geomagnetic excursion. This newly discovered event was named the Santa Rosa Excursion after the location of the only published terrestrial record of the event known at the time. Subsequent work by

Singer and Brown (2002) obtained an age of 942 ± 8 ka. A third attempt to date the SRRD resulted in a younger age of 932 ± 5.4 ka (Singer 2014). All sanidine ages from SRRD are affected by the presence of (minor) excess ^{40}Ar, as revealed in elevated ^{40}Ar/^{36}Ar trapped argon signatures and characteristic saddle-shaped incremental heating spectra for single sanidine crystals (Singer and Brown 2002). Therefore, these sanidine ages are likely somewhat older than the SRRD eruption age and thus overestimate the timing of the SRE.

The SRE was also recorded as a large directional change in a sediment core (MD972143) from the Philippine Sea (Horng et al., 2002) and as a directional change that appears to be related to a prominent decrease in relative geomagnetic paleointensity (RPI) in Ocean Drilling Program (ODP) cores at Sites 983 and 984 from the Iceland Basin (Channell et al., 2002). The astrochronologic age for the SRE recorded in core MD972143 is 920 ± 2 ka (Marine Isotope Stage 23/24; Horng et al., 2002). The higher sedimentation rates and corresponding higher resolution of ODP cores 983 and 984 provide an age of ca. 932 ka (top of Marine Isotope Stage 25) with a duration of 3 k.y. for the SRE (Channell et al., 2002). A stack of multiple astronomically tuned sedimentary archives of RPI (PISO1500) suggests that the SRE is a global feature associated with a virtual axial dipole moment (VADM) low at 926 ka (Channell et al., 2009). We regard the astrochronology of the global PISO1500 stack as providing the most reliable target age estimate of the SRE.

Our new ^{40}Ar/^{39}Ar ages suggest that the intermediate directions and very low absolute paleointensities in lava flows from supersite GA-X on Floreana Island, Galapagos (Wang and Kent, 2013) are associated with the SRE. We derived the most consistent and reliable age spectra from the groundmasses sampled at the base of lava flow GA79, which give an average age of 925.7 ± 4.6 ka (Fig. 2.1). As expected for the dating of holocrystalline groundmass samples, which reflect the eruption ages of the lava flows and are not affected by any residence time in a magma chamber, there is no significant sign of excess ^{40}Ar in the presented data, explaining our lower eruption age compared to the sanidine ages of the SRRD (Singer and Brown, 2002; Singer, 2014). Our age is in excellent agreement with the 926 ka age for the paleomagnetic minimum in the global PISO1500 stack (Channell et al., 2009) (Fig. 2.2).

2.4.2 Santa Rosa as a Short-Lived Global Geomagnetic Excursion

The close agreement of our new high-precision age for the Floreana lava flow with ages from high-latitude ODP Sites 983 and 984, as well as with the terrestrial SRRD in New Mexico, shows the global extent of the SRE, whereas VGP's and relative intensity data from ODP cores 983 and 984 suggest a reduction and recovery of the field within ~3 k.y. (Channell et al., 2002). These observations are validated in the basaltic lava flows on Floreana, which record a VADM value of $1.1 \pm 0.3 \times 10^{22}$ Am^2 (Fig. 2.2) that is as low as during any paleomagnetic reversal (e.g., Channell et al., 2009; Ziegler et al., 2011). During this time interval, the SRE resulted in the single lowest VADM value for all recognized and defined excursional events. The PADM2M stack for the last two million years displays a mean VADM of 5.32×10^{22} Am^2 compared to the mean (1.35×10^{22} Am^2) of the lowest intensities during polarity reversals, which closely corresponds to the Santa Rosa VADM value of $1.1 \pm 0.3 \times 10^{22}$ Am^2. Our new data demonstrate that geomagnetic field excursions can result in

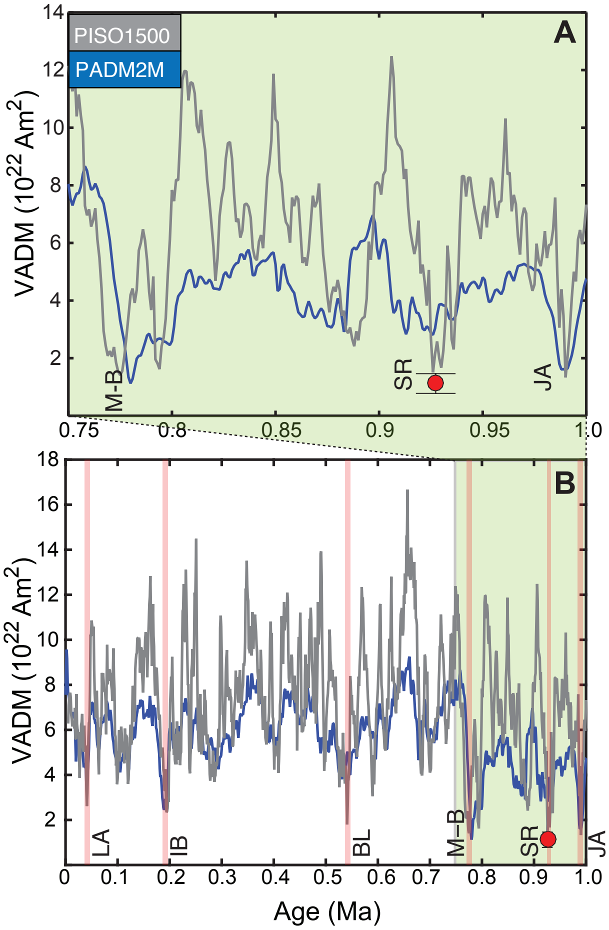

Figure 2.2. The paleomagnetic axial dipole moment (comparable to virtual axial dipole moment [VADM]) for 0–2 Ma (PADM2M) stack of Ziegler et al., (2011) is shown as a blue line. The PISO1500 stack of Channell et al., (2009) is shown as a gray line. VADM for Floreana (Galapagos Islands) lava supersite GA-X from Wang and Kent (2013) is shown with a red circle. The error for the Floreana lavas represents the measured error on the paleomagnetic intensity as well as the error on the age. A: Zoomed axis showing the age range of 0.75–1 Ma. B: VADM variation during the past 1 m.y. Some major paleointensity lows are highlighted in pink; LA—Laschamp, IB—Iceland Basin, BL—Big Lost, M-B—Matuyama-Bruhnes, SR—Santa Rosa, JA—end of Jaramillo.

field strength lows similar to known reversals. It further suggests that changes within the geodynamo can generate a global field strength reduction equal to an approximate 86% loss of the present-day field strength (7.8×10^{22} Am^2; Korte and Constable, 2005) in a time interval as short as 3 k.y.

Of the multiple excursions identified thus far, only a few have been studied in detail and even fewer have been confirmed as global events. The most widely studied geomagnetic excursion is known as the Laschamp Excursion (Bonhommet and Zahringer, 1969; Roperch et al., 1988; Gubbins, 1999). This excursion occurred at 41.2 ± 1.6 ka, extended over only 1,500 years, and had a VADM minimum of $1.2 \pm 0.1 \times 10^{22}$ Am^2 (Laj et al., 2014), which is comparable in field-strength reduction to the SRE record on Floreana. These two events indicate that excursions may have similar dynamics in terms of duration and minimum field strength independent of whether they occur within a normal polarity chron (e.g., Laschamp) or a reverse polarity chron (e.g., Santa Rosa).

2.5 Conclusions

We define a new $^{40}Ar/^{39}Ar$ age of 925.7 ± 4.6 ka (2σ) for the Santa Rosa Excursion that is recorded in lavas on Floreana Island in the Galapagos Archipelago. Our data illustrate a dramatic change in VGP and geomagnetic field strength during a similar time interval recorded in two volcanic and three sedimentary archives, identifying a global extent for the excursion. The published record from Floreana Island suggests an 86% reduction in absolute field intensity in the equatorial region. The PISO1500 stack illustrates a significant relative field strength reduction at this time (Channell et al., 2009) and the directional data from high-resolution ODP Sites 983 and 984 indicate a directional excursion lasting a few millennia that is synchronous with this event (Channell et al., 2002). Taken together, the sedimentary records and igneous-rock data are convincing evidence of global field behavior that deviated markedly from an axial geocentric dipole. These data suggest that the SRE was both a significant and short-lived geomagnetic anomaly, illustrating the potential for the geodynamo to dramatically alter the geomagnetic field in a few millennia. The global extent and short duration (sediment records) and the dramatic decrease in field intensity (igneous-rock data) of this excursion should thus place important constraints on models of the geodynamo. Finally, the equatorial record suggests that the dramatic reduction in field strength likely results in larger changes in the in-situ production rates of cosmogenic nuclides at lower latitudes, as a function of the changing dipole moment and co-latitude terms in the cut-off rigidity equation (Elsasser, et al., 1957). This underscores the importance of further work to constrain the relationship between low latitude field strength changes and the associated changes to in situ cosmogenic nuclide production rates.

2.6 Acknowledgments

We thank Marco Andres Almeida Vaca for his invaluable assistance in the field, Robert Butler for providing field equipment and invaluable guidance regarding paleomagnetic sampling techniques, and Daniel Miggins and Julia Klath for their hours of ^{40}Ar/^{39}Ar analytical assistance. We thank the Galapagos National Park for their permission and logistical support of sample collection. We thank one anonymous reviewer and James E.T. Channell for very helpful comments that improved the paper. This work was supported by a Ford Foundation Fellowship, a National Science Foundation (NSF) Graduate Fellowship, an NSF Doctoral Dissertation Improvement Grant. Lamont-Doherty Earth Observatory contribution #7982.

2.7 References

Berggren, W.A., Hilgen, F.J., Langereis, C.G., Kent, D.V., Obradovich, J.D., Raffi, I., Raymo, M.E., and Shackleton, N.J., 1995, Late Neogene chronology: New perspectives in high-resolution stratigraphy: Geological Society of America Bulletin, v. 107, p. 1272–1287, doi:10.1130/0016-7606(1995)107<1272:LNCNPI>2.3.CO;2.

Bonhommet, N., and Zahringer, J., 1969, Paleomagnetism and potassium argon age determinations of the Laschamp geomagnetic polarity event: Earth and Planetary Science Letters, v. 6, p. 43–46, doi:10.1016/0012-821X(69)90159-9.

Channell, J., Mazaud, A., Sullivan, P., Turner, S., and Raymo, M., 2002, Geomagnetic excursions and paleointensities in the Matuyama Chron at Ocean Drilling Program sites 983 and 984 (Iceland Basin): Journal of Geophysical Research: Solid Earth, v. 107, p. 1–14.

Channell, J., Xuan, C., and Hodell, D., 2009, Stacking paleointensity and oxygen isotope data for the last 1.5 Myr (PISO-1500): Earth and Planetary Science Letters, v. 283, p. 14–23, doi:10.1016/j.epsl.2009.03.012.

Cox, A., and Dalrymple, G.B., 1966, Palaeomagnetism and potassium-argon ages of some volcanic rocks from the Galapagos Islands: Nature, v. 209, p. 776–777, doi:10.1038/209776a0.

Doell, R.R., and Dalrymple, G.B., 1966, Geomagnetic polarity epochs: A new polarity event and the age of the Brunhes-Matuyama boundary: Science, v. 152, p. 1060–1061, doi:10.1126/science.152.3725.1060.

Doell, R.R., Dalrymple, G.B., Smith, R.L., and Bailey, R.A., 1968, Paleomagnetism, potassium-argon ages, and geology of rhyolites and associated rocks of the Valles caldera, New Mexico: Geological Society of America, v. 116, p. 211–248, doi:10.1130/MEM116-p211.

Elsasser, W.M.,1957, The Terrestrial Dynamo, Geophysics Symposium on Solar and Terrestrial Relationships, Proceedings of the National Academy of Sciences of the United States of America, v. 43, p. 14–24.

Gromme, S., Mankinen, E.A., and Prévot, M., 2010, Time-averaged paleomagnetic field at the equator: Complete data and results from the Galapagos Islands, Ecuador: Geochemistry Geophysics Geosystems, v. 11, Q11009, doi:10.1029/2010GC003090.

Gubbins, D., 1999, The distinction between geomagnetic excursions and reversals: Geophysical Journal International, v. 137, p. F1–F4, doi:10.1046/j.1365-246x.1999.00810.x.

Hora, J.M., Singer, B.S., Jicha, B.R., Beard, B.L., Johnson, C.M., de Silva, S., and Salisbury, M., 2010, Volcanic biotite-sanidine 40Ar/39Ar age discordances reflect Ar partitioning and pre-eruption closure in biotite: Geology, v. 38, p. 923–926, doi:10.1130/G31064.1.

Horng, C.-S., Lee, M.-Y., Palike, H., Wei, K.-Y., Liang, W.-T., Iizuka, Y., and Torii, M., 2002, Astronomically calibrated ages for geomagnetic reversals within the Matuyama chron: Earth, Planets, and Space, v. 54, p. 679–690, doi:10.1186/BF03351719.

Izett, G.A., and Obradovich, J.D., 1994, 40Ar/39Ar age constraints for the Jaramillo Normal Subchron and the Matuyama-Brunhes geomagnetic boundary: Journal of Geophysical Research: Solid Earth, v. 99, p. 2925–2934.

Kent, D.V., Wang, H., and Rochette, P., 2010, Equatorial paleosecular variation of the geomagnetic field from 0 to 3 Ma lavas from the Galapagos Islands: Physics of the Earth and Planetary Interiors, v. 183, p. 404–412, doi:10.1016/j.pepi.2010.08.010.

Koppers, A.A., 2002, ArArCALC—software for 40Ar/39Ar age calculations: Computers & Geosciences, v. 28, p. 605–619, doi:10.1016/S0098-3004(01)00095-4.

Koppers, A.A.P., Duncan, R.A., and Steinberger, B., 2004, Implications of a nonlinear 40Ar/39Ar age progression along the Louisville seamount trail for models of fixed and moving hot spots: Geochemistry Geophysics Geosystems, v. 5, Q06L02, doi:10.1029/2003GC000671.

Koppers, A.A., Gowen, M.D., Colwell, L.E., Gee, J.S., Lonsdale, P.F., Mahoney, J.J., and Duncan, R.A., 2011, New 40Ar/39Ar age progression for the Louisville hot spot trail and implications for inter–hot spot motion: Geochemistry Geophysics Geosystems, v. 12, Q0AM02, doi:10.1029/2011GC003804.

Korte, M., and Constable, C., 2005, The geomagnetic dipole moment over the last 7000 years—New results from a global model: Earth and Planetary Science Letters, v. 236, p. 348–358, doi:10.1016/j.epsl.2004.12.031.

Kuiper, K., Deino, A., Hilgen, F., Krijgsman, W., Renne, P., and Wijbrans, J., 2008, Synchronizing rock clocks of Earth history: Science, v. 320, p. 500–504.

Laj, C., Guillou, H., and Kissel, C., 2014, Dynamics of the earth magnetic field in the 10–75 kyr period comprising the Laschamp and Mono Lake excursions: New results from the French Chaîne des Puys in a global perspective: Earth and Planetary Science Letters, v. 387, p. 184–197, doi:10.1016/j.epsl.2013.11.031.

McDougall, I., and Harrison, T.M., 1999, Geochronology and Thermochronology by the 40Ar/39Ar Method: New York, Oxford University Press, 288 p.

Merrill, R.T., McElhinny, M.W., and McFadden, P.L., 1996, The Magnetic Field of the Earth: Paleomagnetism, the Core, and the Deep Mantle: San Diego, California, Academic Press, International Geophysics Series, 531 p.

Min, K., Mundil, R., Renne, P.R., and Ludwig, K.R., 2000, A test for systematic errors in 40Ar/39Ar geochronology through comparison with U/Pb analysis of a 1.1-Ga rhyolite: Geochimica et Cosmochimica Acta, v. 64, p. 73–98, doi:10.1016/S0016-7037(99)00204-5.

Renne, P.R., Swisher, C.C., Deino, A.L., Karner, D.B., Owens, T.L., and DePaolo, D.J., 1998, Intercalibration of standards, absolute ages and uncertainties in

40Ar/39Ar dating: Chemical Geology, v. 145, p. 117–152, doi:10.1016/S0009-2541(97)00159-9.

Rochette, P., Atig, F.B., Collombat, H., Vandamme, D., and Vlag, P., 1997, Low paleosecular variation at the equator: A paleomagnetic pilgrimage from Galapagos to Esterel with Allan Cox and Hans Zijderveld: Geologie & Mijnbouw, v. 76, p. 9–19, doi:10.1023/A:1003087802352.

Roperch, P., Bonhommet, N., and Levi, S., 1988, Paleointensity of the earth's magnetic field during the Laschamp excursion and its geomagnetic implications: Earth and Planetary Science Letters, v. 88, p. 209–219, doi:10.1016/0012-821X(88)90058-1.

Singer, B., and Brown, L.L., 2002, The Santa Rosa Event: 40Ar/39Ar and paleomagnetic results from the Valles rhyolite near Jaramillo Creek, Jemez Mountains, New Mexico: Earth and Planetary Science Letters, v. 197, p. 51–64, doi:10.1016/S0012-821X(01)00598-2.

Singer, B.S., 2014, A Quaternary geomagnetic instability time scale: Quaternary Geochronology, v. 21, p. 29–52, doi:10.1016/j.quageo.2013.10.003.

Singer, B.S., Hoffman, K.A., Chauvin, A., Coe, R.S., and Pringle, M.S., 1999, Dating transitionally magnetized lavas of the late Matuyama Chron: Toward a new 40Ar/39Ar timescale of reversals and events: Journal of Geophysical Research: Solid Earth, v. 104, p. 679–693.

Spell, T.L., and Harrison, T.M., 1993, 40Ar/39Ar Geochronology of Post-Valles Caldera Rhyolites, Jemez Volcanic Field, New Mexico: Journal of Geophysical Research: Solid Earth, v. 98, p. 8031–8051.

Wang, H., and Kent, D.V., 2013, A paleointensity technique for multidomain igneous rocks: Geochemistry Geophysics Geosystems, v. 14, p. 4195–4213, doi:10.1002/ggge.20248.

Ziegler, L., Constable, C., Johnson, C., and Tauxe, L., 2011, PADM2M: A penalized maximum likelihood model of the 0–2 Ma palaeomagnetic axial dipole moment: Geophysical Journal International, v. 184, p. 1069–1089, doi:10.1111/j.1365-246X.2010.04905.x.

Chapter 3

Millennial-Scale Instability in the Earth's Magnetic Field Prior to the Matuyama-Brunhes Reversal

Andrea Balbas[1], Anthony A.P. Koppers[1], Robert S. Coe[2], Peter U. Clark[1], Brendan Reilly[1], Joseph Stoner[1], Kevin Konrad[1]

[1]College of Earth, Ocean and Atmospheric Sciences, Oregon State University,

Corvallis, Oregon 97331, USA

[2]Earth and Planetary Science Department, University of California – Santa Cruz,

Santa Cruz, California 95064, USA

To be submitted to Science

3.1 Abstract

Well-dated and consistent paleomagnetic records derived from sedimentary and volcanic sequences can provide important constraints on the geodynamo processes that govern polarity reversals in the Earth's magnetic field. Here we report a paleomagnetic record from multiple well-dated lava flows on Tahiti that brackets the Matuyama-Brunhes (M-B) polarity reversal. Our high-precision $^{40}Ar/^{39}Ar$ ages constrain large and rapid changes in field orientation occurring up to ~35 kyr prior to the M-B reversal that are contemporaneous with changes in paleomagnetic directions and the onset of low-magnetic field strength identified in widely distributed sediment and lava-flow records. This prolonged 35-kyr period of geomagnetic instability supports models that show frequent centennial-to-millennial scale polarity changes in the presence of a strongly weakened dipole field.

3.2 Introduction

The last polarity reversal, from the reversed Matuyama Chron to the normal Brunhes Chron (M-B reversal), is a critical stratigraphic marker in the development of age models for late Cenozoic sequences (Channell et al., 2010). Most age determinations for the M-B reversal come from astrochronologically tuned sediment records that also identify a strong reduction in intensity of the magnetic field leading up to the reversal (Valet and Fournier, 2016). However, large directional changes associated with field variability may occur on timescales that cannot be resolved by many sediment records due to low sedimentation rates (Channell et al., 2012; Roberts and Winklhofer, 2004). Well-dated volcanic records by $^{40}Ar/^{39}Ar$ geochronology have the potential to capture such short-lived changes in the global and regional morphology of the Earth's magnetic field, but because these records are discontinuous, they require a large number of well-dated lava flows to constrain a more detailed structure of temporal changes in field behavior.

Applying these different geochronological approaches to the M-B reversal has led to a fundamental disagreement about its age, with constraints from $^{40}Ar/^{39}Ar$ dating of lava flows suggesting an older age than the astrochronological age derived from sediments. Accordingly, some have questioned the decay constant and the age of the standard used in the calculation of the $^{40}Ar/^{39}Ar$ ages (Channell et al., 2010; Singer, 2014). We note, however, that the same combination of methods provides concordant ages for other paleomagnetic events including the Laschamp (Lascu et al., 2016) and Santa Rosa (Balbas et al., 2016) excursions (Supplementary Information), suggesting another explanation for the apparent disagreement in the timing of the M-B reversal. Previous studies (Singer et al., 2005; Valet et al., 2014) suggest that the $^{40}Ar/^{39}Ar$ ages are correct and, as such, constrain a transitional phase of unstable field behavior prior to the M-B reversal. Sediment and ice-core records have long suggested that the period leading up to the M-B reversal had a complex structure. In these records, two phases of global low-dipole intensities are recognized, with the first low occurring ~15-20 ka before the M-B reversal, often referred to as the precursor event, and the second low occurring at the time of the reversal (Channell et al., 2009; Hartl and Tauxe, 1996; Kent and Schneider, 1995; Raisbeck et al., 2006).

3.3 Methods and Results

Here we assess these various hypotheses by developing a new chronology based on 46 high-precision ^{40}Ar/^{39}Ar ages on 13 basaltic lava flows from Tahiti that span the M-B reversal and several tens of millennia before it. We reoccupied the Punarruu Valley site to resample Tahitian lava flows A2-A29 and B1-B5 that were previously dated by ^{40}Ar/^{39}Ar (Mochizuki et al., 2011). Two or more basaltic groundmass samples were analyzed from each flow by ^{40}Ar/^{39}Ar incremental heating experiments, and age plateaus from multiple heating experiments from each flow were combined to derive the eruption age (Supplemental Materials). Our new ^{40}Ar/^{39}Ar ages were made against Fish Canyon Tuff sanidine (FCT) as a flux monitor with an age of 28.201 ± 0.046 Ma (Kuiper et al., 2008) and calculated using updated equations and ^{40}K decay constant (Min et al., 2000). Our ages on the Tahitian flows range from 857.4 ± 3.5 ka to 770.6 ± 5.9 ka (all uncertainties in this study are 2σ internal errors) and thus capture several geomagnetic phases prior to, during and after the reversal, as defined in astronomically dated sediment records. These include the stable-reversed Matayuma Chron, a “precursor” phase characterized by a paleointensity low ~15-20 ka prior to the reversal phase (Kent and Schneider, 1995), the main reversal phase at 773.1 ± 0.4 ka (Channell et al., 2010), and the stable-normal Brunhes Chron.

We also measured the paleomagnetic direction in 22 of the exposed basalt flows (Supplemental Materials). Our paleomagnetic data from the flows are in good agreement with a previous study (Mochizuki et al., 2011) from this location except for flow B1 (Figure 3.11), which was reported as recording a reversed geomagnetic orientation. Field measurements with our hand-held magnetometer indicated that this

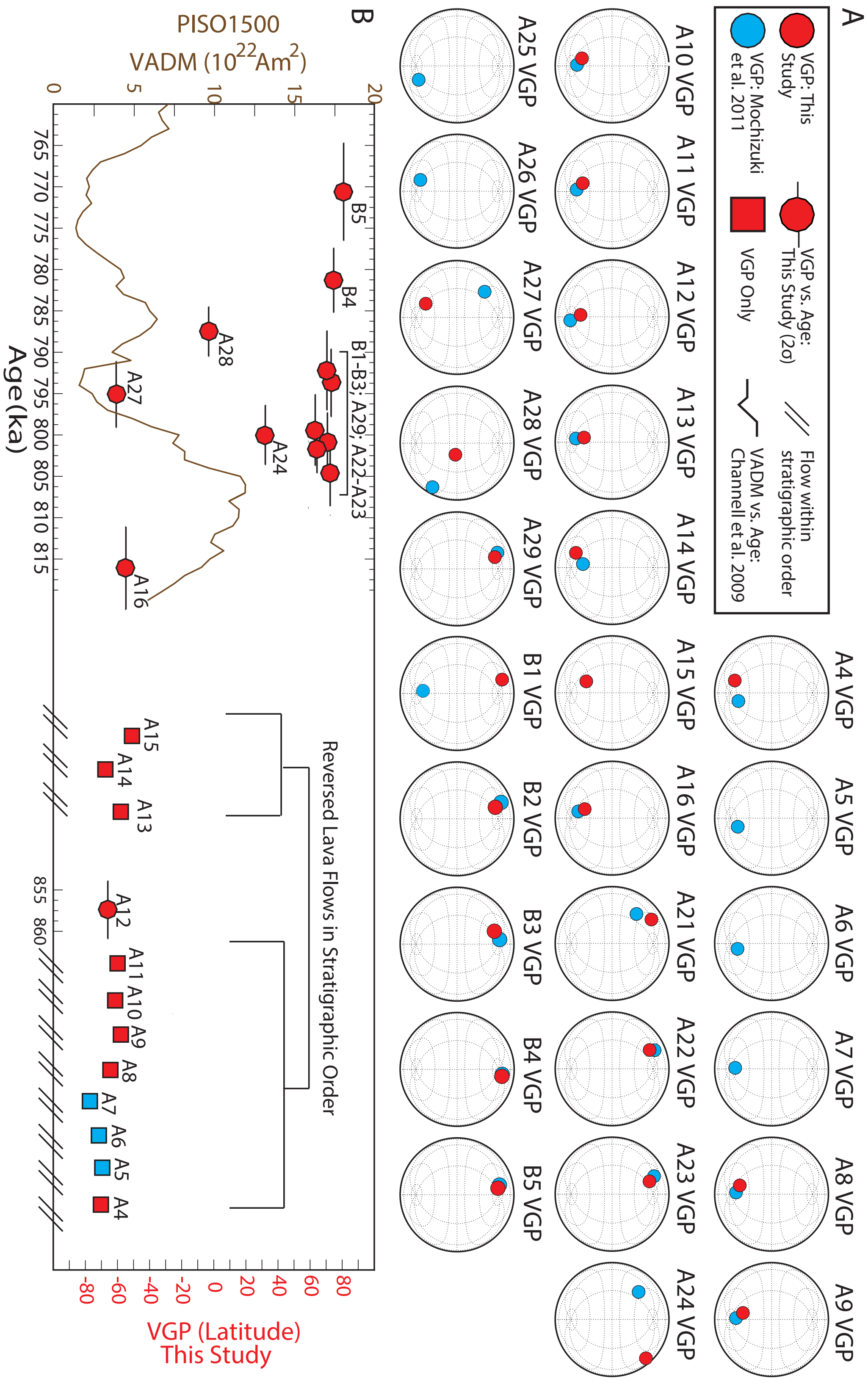
A
VGP: This Study
VGP: Mochizuki et al. 2011
VGP vs. Age: This Study (2σ)
VGP Only
Flow within stratigraphic order
VADM vs. Age: Channell et al. 2009
A4 VGP
A5 VGP
A6 VGP
A7 VGP
A8 VGP
A9 VGP
A10 VGP
A11 VGP
A12 VGP
A13 VGP
A14 VGP
A15 VGP
A16 VGP
A21 VGP
A22 VGP
A23 VGP
A24 VGP
A25 VGP
A26 VGP
A27 VGP
A28 VGP
A29 VGP
B1 VGP
B2 VGP
B3 VGP
B4 VGP
B5 VGP
B
PISO1500
VADM ($10^{22}Am^2$)
0
5
10
15
20
Age (ka)
765 770 775 780 785 790 795 800 805 810 815
855 860
B5
B4
A28
A27
B1–B3; A29; A22–A23
A24
A16
A12
Reversed Lava Flows in Stratigraphic Order
A15
A14
A13
A11
A10
A9
A8
A7
A6
A5
A4
VGP (Latitude)
This Study
-80
-60
-40
-20
0
20
40
60
80

Figure 3.1: Data from this study (Red) and Mochizuki et al., (2011) (Blue). (A) Mean VGP positions for all flows from this site. (B) Virtual axial dipole moment (VADM) PISO-1500 sediment stack (black line; Channell et al., 2009) plotted against Tahiti basalt VGP's. Squares represent samples without age determinations. Undated flow A21 is not shown.

flow records a normal magnetic field orientation, which is in agreement with our lab measurements. The 13 oldest flows have reversed polarity; we dated two of these flows at 857.4 ± 3.5 ka (A12) and 816.1 ± 5.0 ka (A16) (Figure 3.1). The next ten younger flows, which range in age from 801.7 ± 2.9 ka (B1) to 781.3 ± 3.9 ka (B4), have VGP latitudes that range consecutively from normal to transitional to normal to reversed to normal to transitional to normal (Figure 3.1). The youngest sample (B5) has a normal polarity, which, according to its 770.6 ± 5.9 ka age, may have formed after the main M-B reversal at 773 ka.

3.4 Discussion and Conclusion

Figure 3.2 compares our Tahitian constraints on magnetic field variability prior to the M-B reversal with similar evidence from other lava flow sequences dated by ^{40}Ar/^{39}Ar ages (Brown et al., 2004; Singer et al., 2002). We recalibrated all previously published ^{40}Ar/^{39}Ar ages to the same ^{40}K decay constants and the FCT standard age used for the Tahitian samples. Dated samples from the Maui site extend back to 785.1 ± 8.0 ka (Coe et al., 2004), while the La Palma and Chile samples largely occur between ~790 to 810 ka, coincident with the precursor phase (Singer et al., 2005) (Figure 3.2). VGP latitudes from these flows that are older than the M-B reversal range from reversed to normal, with a number of transitional directions clustered in the southern low latitudes. Here, we define field instability during the Matuyama Chron as any VGP between -45° and 90° latitude. Probability density functions (PDFs) of lava flows from Tahiti, Chile and La Palma that meet this

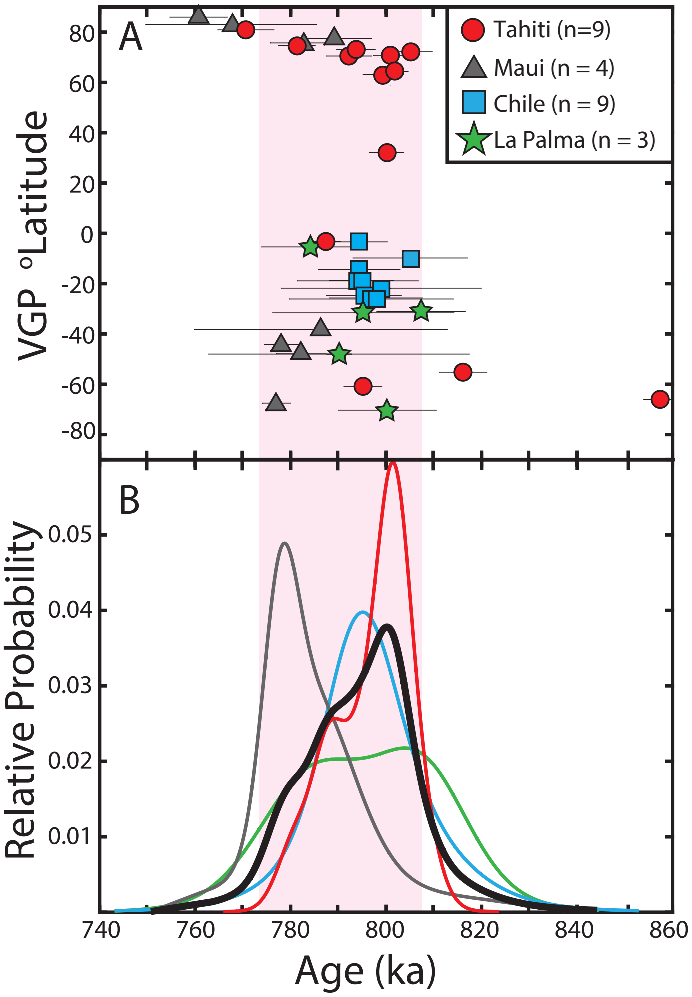

Figure 3.2: VGP latitudes through time from all field sites that record the M-B reversal (Coe et al., 2004; Singer et al., 2005) with corresponding probability density functions (PDF). The PDF curves incorporate only latitudinal VGPs between -45^o to 90^o interpreted as indicating instability during the Matuyama chron. The black PDF curve is a combination of all site data with VGP's between -45^o to 90^o. Pink bar represents 35 kyrs before the Brunhes Chron. All errors are 2σ uncertainty.

criterion, suggest that much of this instability occurred between ~795 ka and 805 ka; Maui is younger, being centered on ~779 ka.

Previous interpretations of this behavior from any given site suggested that the peak age of an instability PDF curve represented the M-B reversal, thus giving rise to disagreement about the age of the reversal (Channell et al., 2010). Because lava-flow records are discontinuous, however, we instead argue that the data from all four sites should be combined into a composite record that, while still discontinuous, provides a more complete record of field behavior. A PDF that includes all of the data suggests a prolonged period of instability that extends from the M-B reversal at ~773 ka to ~808 ka (Figure 3.2), nearly twice as long as previously considered (Singer et al., 2005). Additional ^{40}Ar/^{39}Ar dated records older than 808 ka are required to assess whether this unstable period might be longer. We also note that the frequency of the large polarity changes within this 35-kyr window suggests that geomagnetic changes were occurring on a millennial and perhaps centennial timescale. This is particularly well demonstrated by our high-resolution dating of Tahitian flows, which identifies two large excursions between ~800 ka and 787 ka; whereas the Maui data shows another large excursion between ~782 ka and the M-B reversal (Figure 3.2).

Well-dated, high-resolution sediment cores from a range of latitudes show that VGPs don’t maintain stable-reversed directions during the 35-kyr instability interval identified from volcanic records, although their expression suggests a lower frequency as well as lower amplitude (Figure 3.3). We use a simple illustrative model to show that rapid directional changes that take place on centennial-to-millennial timescales are smoothed in sediment records as a function of sampling method and

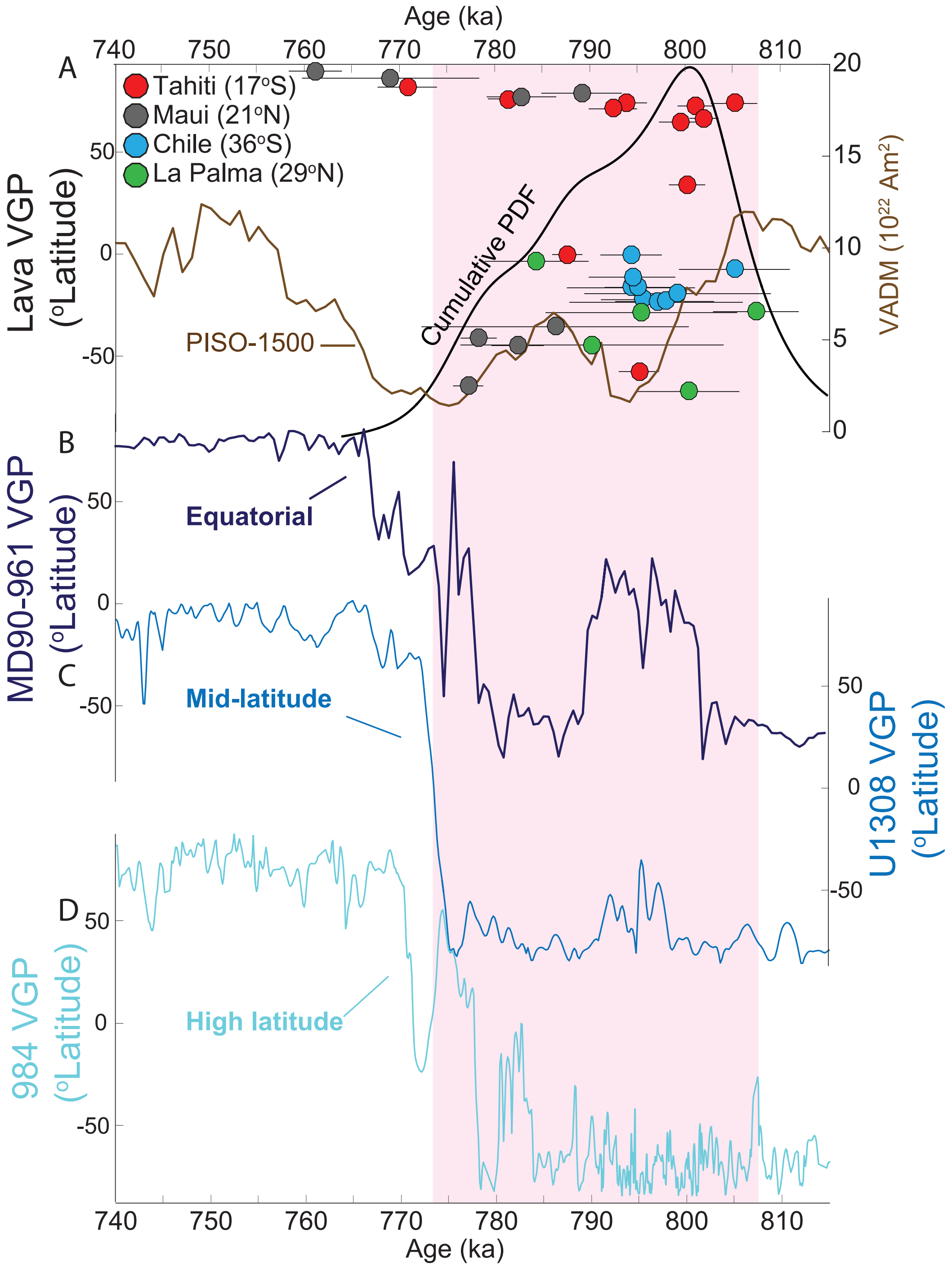

Age (ka)
740
750
760
770
780
790
800
810
A
Tahiti (17°S)
Maui (21°N)
Chile (36°S)
La Palma (29°N)
Lava VGP (°Latitude)
50
0
-50
20
15
10
5
0
VADM (10^{22} Am^2)
Cumulative PDF
PISO-1500
B
MD90-961 VGP (°Latitude)
Equatorial
C
Mid-latitude
U1308 VGP (°Latitude)
D
984 VGP (°Latitude)
High latitude

Figure 3.3: Latitudinal VGP variation of lava flow data compared against sediment core data from a range of latitudes. (Top) All lava flow records from this time interval (circles) compared against PISO-1500 stack (brown line). The black line represents the cumulative PDF curve for all lava flow data (Coe et al., 2004; Singer et al., 2005). Pink bar represents 35 kyrs before the Brunhes Chron. (Bottom) Astrochronologically tuned sediment cores ODP site 984 (average sedimentation rate is 11.5 cm kyr^{-1}; (Channell et al., 2002), IODP site U1308 (average sedimentation rate is 7.3 cm kyr^{-1}; (Channell et al., 2008), and MD90-961 (average sedimentation rate is 4.7 cm kyr^{-1} (Valet et al., 2014).

post-depositional processes, explaining the different expressions of VGP variability in sediment cores during this unstable period (Supplemental Materials).

Our results suggest that the sedimentary and volcanic records of field variability prior to and during the M-B reversal are contemporary and related, supporting good agreement between the astrochronological and $^{40}Ar/^{39}Ar$ dating methodologies during the last million years. The onset of the prolonged period of directional instability identified from these records is coincident with the start of the precursor phase signified by a field intensity reduction that is well expressed in the PISO-1500 stack (Figure 3.3). On top of that, the majority of the transitional volcanic VGP latitudes recorded in lava flows from Tahiti, Maui, Chile and La Palma are then coincident with a divergence from reversed field direction in some sediment records (Channell et al., 2008; Valet et al., 2014). This unstable field, coeval with the precursor phase of low-dipole intensity, suggests a period of heightened and extreme secular variation with large directional changes occurring on centennial to millennial timescales (Brown et al., 2007; Valet et al., 2012). There are fewer observations of field instabilities from volcanic records (e.g. Maui) during a second phase of low-dipole intensity, which may suggest either a sampling bias or relatively short-lived field instability immediately prior to the M-B reversal. The events described in this paper offer important new insights into the short precursor history of a reversing field and the rapid -- if not erratic -- changing field dynamics during periods of low-dipole intensity.

3.5 References:

Balbas, A., Koppers, A. A., Kent, D. V., Konrad, K., and Clark, P. U., 2016, Identification of the short-lived Santa Rosa geomagnetic excursion in lavas on Floreana Island (Galapagos) by 40Ar/39Ar geochronology: Geology, p. G37569. 37561.

Brown, L. L., Singer, B. S., Pickens, J. C., and Jicha, B. R., 2004, Paleomagnetic directions and 40Ar/39Ar ages from the Tatara-San Pedro volcanic complex, Chilean Andes: Lava record of a Matuyama-Brunhes precursor?: Journal of Geophysical Research: Solid Earth, v. 109, no. B12.

Brown, M. C., Holme, R., and Bargery, A., 2007, Exploring the influence of the non-dipole field on magnetic records for field reversals and excursions: Geophysical Journal International, v. 168, no. 2, p. 541-550.

Channell, J., Hodell, D., and Curtis, J., 2012, ODP Site 1063 (Bermuda Rise) revisited: oxygen isotopes, excursions and paleointensity in the Brunhes Chron: Geochemistry, Geophysics, Geosystems, v. 13, no. 2.

Channell, J., Hodell, D., Singer, B., and Xuan, C., 2010, Reconciling astrochronological and 40Ar/39Ar ages for the Matuyama-Brunhes boundary and late Matuyama Chron: Geochemistry, Geophysics, Geosystems, v. 11, no. 12.

Channell, J., Hodell, D., Xuan, C., Mazaud, A., and Stoner, J., 2008, Age calibrated relative paleointensity for the last 1.5 Myr at IODP Site U1308 (North Atlantic): Earth and Planetary Science Letters, v. 274, no. 1, p. 59-71.

Channell, J., Mazaud, A., Sullivan, P., Turner, S., and Raymo, M., 2002, Geomagnetic excursions and paleointensities in the Matuyama Chron at Ocean

Drilling Program sites 983 and 984 (Iceland Basin): Journal of Geophysical Research: Solid Earth (1978–2012), v. 107, no. B6, p. EPM 1-1-EPM 1-14.

Channell, J., Xuan, C., and Hodell, D., 2009, Stacking paleointensity and oxygen isotope data for the last 1.5 Myr (PISO-1500): Earth and Planetary Science Letters, v. 283, no. 1, p. 14-23.

Coe, R. S., Singer, B. S., Pringle, M. S., and Zhao, X., 2004, Matuyama–Brunhes reversal and Kamikatsura event on Maui: paleomagnetic directions, 40 Ar/39 Ar ages and implications: Earth and Planetary Science Letters, v. 222, no. 2, p. 667-684.

Hartl, P., and Tauxe, L., 1996, A precursor to the Matuyama/Brunhes transition-field instability as recorded in pelagic sediments: Earth and Planetary Science Letters, v. 138, no. 1, p. 121-135.

Kent, D. V., and Schneider, D. A., 1995, Correlation of paleointensity variation records in the Brunhes/Matuyama polarity transition interval: Earth and Planetary Science Letters, v. 129, no. 1, p. 135-144.

Kuiper, K., Deino, A., Hilgen, F., Krijgsman, W., Renne, P., and Wijbrans, J., 2008, Synchronizing rock clocks of Earth history: science, v. 320, no. 5875, p. 500-504.

Lascu, I., Feinberg, J. M., Dorale, J. A., Cheng, H., and Edwards, R. L., 2016, Age of the Laschamp excursion determined by U-Th dating of a speleothem geomagnetic record from North America: Geology, v. 44, no. 2, p. 139-142.

Min, K., Mundil, R., Renne, P. R., and Ludwig, K. R., 2000, A test for systematic errors in 40 Ar/39 Ar geochronology through comparison with U/Pb analysis of a 1.1-Ga rhyolite: Geochimica et Cosmochimica Acta, v. 64, no. 1, p. 73-98.

Mochizuki, N., Oda, H., Ishizuka, O., Yamazaki, T., and Tsunakawa, H., 2011, Paleointensity variation across the Matuyama-Brunhes polarity transition: Observations from lavas at Punaruu Valley, Tahiti: Journal of Geophysical Research: Solid Earth (1978–2012), v. 116, no. B6.

Raisbeck, G., Yiou, F., Cattani, O., and Jouzel, J., 2006, 10Be evidence for the Matuyama–Brunhes geomagnetic reversal in the EPICA Dome C ice core: Nature, v. 444, no. 7115, p. 82-84.

Roberts, A. P., and Winklhofer, M., 2004, Why are geomagnetic excursions not always recorded in sediments? Constraints from post-depositional remanent magnetization lock-in modelling: Earth and Planetary Science Letters, v. 227, no. 3, p. 345-359.

Singer, B., Relle, M., Hoffman, K., Battle, A., Laj, C., Guillou, H., and Carracedo, J., 2002, Ar/Ar ages from transitionally magnetized lavas on La Palma, Canary Islands, and the geomagnetic instability timescale: Journal of Geophysical Research: Solid Earth, v. 107, no. B11.

Singer, B. S., 2014, A Quaternary geomagnetic instability time scale: Quaternary Geochronology, v. 21, p. 29-52.

Singer, B. S., Hoffman, K. A., Coe, R. S., Brown, L. L., Jicha, B. R., Pringle, M. S., and Chauvin, A., 2005, Structural and temporal requirements for geomagnetic field reversal deduced from lava flows: Nature, v. 434, no. 7033, p. 633-636.

Valet, J.-P., Bassinot, F., Bouilloux, A., Bourlès, D., Nomade, S., Guillou, V., Lopes, F., Thouveny, N., and Dewilde, F., 2014, Geomagnetic, cosmogenic and climatic changes across the last geomagnetic reversal from Equatorial Indian Ocean sediments: Earth and Planetary Science Letters, v. 397, p. 67-79.

Valet, J.-P., Fournier, A., Courtillot, V., and Herrero-Bervera, E., 2012, Dynamical similarity of geomagnetic field reversals: Nature, v. 490, no. 7418, p. 89-93.

Valet, J. P., and Fournier, A., 2016, Deciphering Records of Geomagnetic Reversals: Reviews of Geophysics.

Chapter 4

^{10}Be dating constraints on the interplay between the late-Pleistocene Cordilleran Ice Sheet and Missoula Floods

Andrea Balbas[1], Aaron Barth[1], Peter U. Clark[1], Jorie Clark[1], Jim O'Connor[2], Victor R. Baker[3], Kevin Konrad[1], Marc Caffee[4]

[1]College of Earth, Ocean and Atmospheric Sciences, Oregon State University, Corvallis, OR 97331, USA

[2]U.S. Geological Survey, Geology, Minerals, Energy, and Geophysics Science Center, 2130 SW 5th Avenue, Portland, OR 97201, USA

[3]Department of Hydrology and Water Resources, University of Arizona, Tucson, AZ 85721, USA

[4]Department of Physics and Astronomy, Purdue University, West Lafayette, IN 47907, USA

To be submitted to Geology

4.1 Abstract

During the late Pleistocene, at least 89 catastrophic outburst floods triggered by the intermittent failure of an ice dam impounding Glacial Lake Missoula flowed across wide swaths of central Washington and down the Columbia River to the Pacific Ocean. The magnitudes, routings, and timing of many of these megafloods, however, remain largely unconstrained. Here we report cosmogenic ^{10}Be ages on flood boulders associated with several key flood landforms as well as on moraines formed by the Okanogan lobe of the Cordilleran Ice Sheet. Our ^{10}Be ages identify a large megaflood with a flux of 10-17 x 10^6 m^3s^{-1} (Benito and O'Connor, 2003) that occurred at 17.2 ± 0.8 ka, before blockage of the northern Columbia River by the advancing Okanogan lobe. ^{10}Be ages on moraines formed by the southernmost advance of the Okanogan lobe indicate that it began its retreat between 14.0 to 14.8 ka, likely in response to onset of the Bølling warm period. Floods that occurred after lobe retreat were not as large as those before blockage of the northern Columbia by this ice lobe. Several ^{10}Be ages indicate that megafloods continued after the initial retreat of the Purcell Trench Lobe (15.5 ± 0.8 ka) until as recently as 13.2 ± 1.0 ka. The age of the youngest flood indicates that this last megaflood may have been witnessed by early native people and may have influenced their oral traditions.

4.2 Introduction

The Missoula floods, which were caused by failure of an ice dam and rapid draining of Glacial Lake Missoula, are the largest floods known from Earth's geologic record (Baker, 1978; Benito and O'Connor, 2003; Bretz, 1923, 1928; O'Connor and Baker, 1992). The point of release was northeast of Spokane, Washington, and floodwaters traveled southwest across central Washington to the Columbia River and ultimately into the Pacific Ocean (Figure 4.1). The Channeled Scabland region in east-central Washington was shaped by these megafloods into a spectacular complex of anastomosing channels, coulees, cataracts, loess islands, rock basins, broad gravel deposits, and immense gravel bars. J Harlen Bretz first recognized this assemblage as the result of erosion and deposition by cataclysmic flooding (Bretz, 1923).

More recent work has not only confirmed that the Channeled Scabland was produced by megaflooding, but that it was also affected by multiple floods (Atwater, 1986; Baker and Bunker, 1985; Benito and O'Connor, 2003; Waitt, 1980, 1985), with the largest having peak discharges of at least 10^{-17} x 10^{6} $m^{3}s^{-1}$ (Benito and O'Connor, 2003; O'Connor and Baker, 1992). Evidence for multiple floods suggests that the evolution of the Scablands landscape has a much more complex history than would be inferred from its formation by only one flood. Nevertheless, several fundamental questions about the Missoula floods and the evolution of the Channeled Scabland landscape remain, including how the floods are related to the growth and decay of the Cordilleran Ice Sheet. In particular, while the rhythmically bedded slackwater deposits provide important constraints on the number and duration of flooding episodes (Atwater, 1986; Waitt, 1985), and the relative timing of changes in their routing across the landscape (Waitt et al., 2009), “dating of the last-glacial Missoula floods is sparse and remains a work in progress” (Waitt et al., 2009, p. 781),

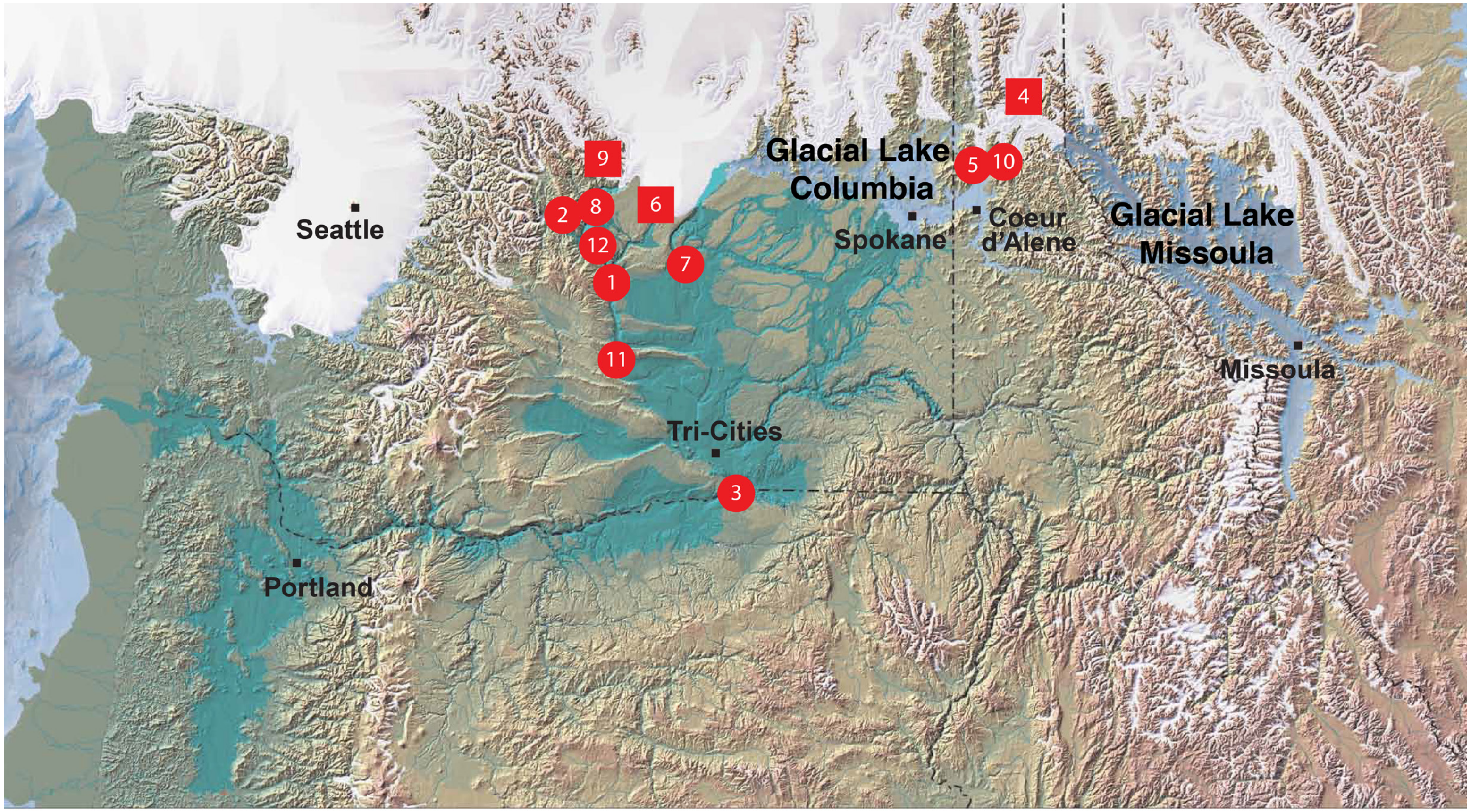

1 Babcock Ridge
2 Wenatchee Rafted
3 Wallula Gap
4 Purcell Trench
5 Spirit Lake Ripples
6 Withrow Moraine
7 Ephrata Fan
8 Wenatchee Bar
9 Chelan Moraine
10 S. Lake Pend Oreille
11 Matawa Fan
12 Pangborn Bar

Figure 4.1: A map of the Pacific Northwest landscape during the last glacial maximum with our field site markers superimposed. The base map is adapted with permission from the Ice Age Floods Institute. Circles represent flood deposited boulders and squares represent glacier deposited boulders. Individual site numbers are shown within each symbol and correlate to Figures 4.2 and 4.3.

particularly with regard to flood pathways. The age of the flood-landscape elements that comprise the Channeled Scabland and other parts of the flood path remain largely unknown because of the dearth of organic material for radiocarbon dating associated with these landscapes. Here we use ^{10}Be surface exposure dating of boulders associated with these events to unravel the timing and relationship of late Pleistocene megafloods and Cordilleran Ice Sheet growth and decay.

4.3 Methods

We collected samples from 26 boulders deposited on 11 features associated with megaflooding and the Cordilleran Ice Sheet (Figure 4.1). We preferentially sampled large (>1m) boulders, many with polished surfaces, positioned at least 0.5 meters above the ground surface thus limiting the chances of post-depositional movement and exhumation. Boulder surfaces were relatively smooth (relief < 1 cm) suggesting little to no post-depositional weathering or erosion of sampled surfaces. We did not account for erosion in our age determinations but sensitivity tests indicate that conservative erosion estimates (1 mm ka^{-1}) would increase our ages <2% (Ballantyne and Stone, 2012). Samples were collected from the upper 2 cm of each boulder's top surface and processed for ^{10}Be/^{9}Be measurements at Oregon State University Cosmogenic Isotope Laboratory following procedures of Licciardi (2000) and Marcott (2011). Accelerator Mass Spectrometry measurements were made at the Purdue Rare Isotope Measurement (PRIME) laboratory. All ^{10}Be ages were calculated using the CRONUS-Earth online calculator (v. 2.2) with the northeast North America (NENA) production rate (Balco et al., 2009) and the time-dependent scaling scheme of Lal (1991) and Stone (2000). The 07KNSTD standard was used for analyses. Blanks range from 8.3 ± 9.6 to 26.3 ± 9.3 x 10^3 ^{10}Be atoms (see supplement).

All errors are reported with 1 sigma uncertainty and include the production rate uncertainty of 4.8% (Balco et al., 2009). See appendix C for the methods for mean site age determinations. Shielding factors for applicable samples were calculated using the CRONUS-geometric shielding calculator. Ages are interpreted as the onset of deglaciation when associated with a moraine and the time of deposition by floods when associated with flood features.

4.4 Results

Ten of our site ages date the deposition of boulders on flood features. A single ^{10}Be age from a boulder from the top of Babcock Ridge (site 1) (395 m elevation) dates its deposition at 22.2 ± 1.3 ka (Figure 4.2). Ages for three boulders deposited closely together with elevations from 421 to 441 m in north Wenatchee (site 2) range from 17.4 to 17.0 ka with a mean age and uncertainty of 17.2 ± 0.8 ka. A similar ^{10}Be age of 17.2 ± 1.2 ka dates the deposition of a boulder at 341 m elevation near Wallula Gap (site 3). Three boulders deposited on the giant ripple marks close to Spirit Lake (site 5) have ages that range from 13.8 to 16.7 ka with a mean age of 15.2 ± 1.1 ka. Southeast of Moses Coulee, four boulders deposited on the Ephrata Fan (site 7) have ^{10}Be ages ranging from 14.1 to 15.2 ka and a mean age of 14.7 ± 0.8 ka. Two surface exposure ages from boulders on an armored bar along the Columbia River north of Wenatchee (site 8) have ^{10}Be ages of 14.4 and 14.6 ka and a mean age of 14.5 ± 0.7

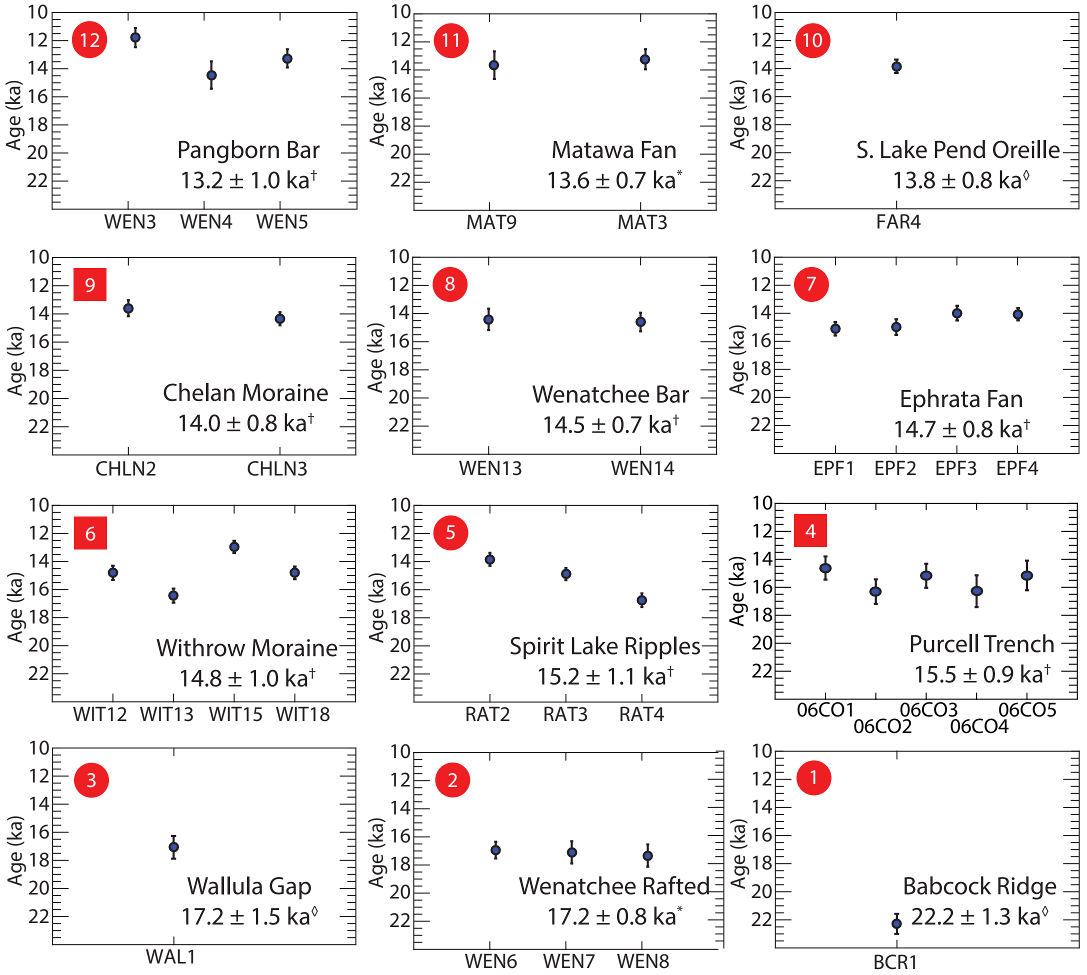

Figure 4.2: A summary of ^{10}Be surface exposure ages of boulders associated with late Pleistocene megafloods. Individual samples are defined in the x-axis with sample age in the y-axis. Site numbers appear in the upper left corner of each plot and correlate to the locations shown in Figure 4.1. Circles represent flood deposited boulders and squares represent glacier deposited boulders. Combined sample ages for single sites and uncertainty are in the right bottom corners. All errors are reported with 1σ confidence and include the uncertainty in the ^{10}Be production rate used (4.8%). The * represents an error weighted mean and uncertainty, † indicates a site mean and standard error and ◊ represents the analytical external error on the single sample. Purcell Trench data is from Breckenridge (2010) while all other data is from this study.

ka. One ^{10}Be age from a boulder west of southernmost Lake Pend Oreille, ID, (site 10) defines its time of deposition as 13.8 ± 0.8 ka. On the Mattawa Fan south of Sentinel Gap (site 11), two boulders have similar ^{10}Be ages of 13.5 and 13.9 ka with a mean age of 13.6 ± 0.7 ka. Our youngest site age is from Pangborn Bar in east Wenatchee (site 12), with three ^{10}Be ages ranging from 11.8 to 14.5 ka and a mean age of 13.2 ± 1.0 ka.

We also sampled boulders from moraines deposited by the Okanagon Lobe. Four boulders deposited on a well-preserved section of the terminal Withrow Moraine within Moses Coulee (site 6) have ^{10}Be ages that range from 13.0 to 16.4 ka and a mean age of 14.8 ± 1.0 ka. Two boulders on a moraine deposited by the Okanogan Lobe southeast of Chelan (site 9) have ^{10}Be ages of 13.6 and 14.3 and a mean age of 14.0 ± 0.8 ka, with the younger age than for the Withrow Moraine being consistent with the sites location farther to the north (Figure 4.1).

4.5 Discussion

Late Pleistocene megaflood dynamics are intimately coupled with the growth and decay of the Cordilleran Ice Sheet. Specifically, the Purcell Trench and Okanogan Lobes of the Cordilleran Ice Sheet played pivotal roles in flood magnitude and routing through time (Atwater, 1986; Baker and Bunker, 1985; Waitt, 1985; Weis et al., 1902). Waitt (1985) argued that the structural integrity and rate of regrowth of the Purcell Trench Lobe after each failure and release of Glacial Lake Missoula determined both the size and frequency of each subsequent flood. In contrast, the advance of the Okanogan Lobe blocked the northern Columbia River and impounded

Glacial Lake Columbia (Atwater, 1986), diverting floodwaters to more easterly routes.

Ages from our field sites help constrain the relationship between the Cordilleran Ice Sheet and the megafloods through time. The single boulder from the Babcock Ridge site is approximately 219 meters above the Columbia River and was likely deposited by an iceberg. The height of the sample indicates a large flood at ~22 ka that may have been routed through an open northern Columbia River or Moses Coulee. Dated boulders from north Wenatchee are approximately 225 to 245 meters above the Columbia River. They were also likely deposited by an iceberg entrained in a large flood that traveled down an open northern Columbia River passage ~17.2 ka. The Wallula Gap is a constriction of the Columbia River that was a significant obstacle to the flow of floodwaters to the Pacific Ocean, resulting in hydraulic damming and the formation of a large temporary lake north of the constriction (Bretz, 1925; Waitt, 1980). The Wallula Gap boulder (341 meters elevation) was also likely deposited by an iceberg stranded along the edge of the flow margin that, according to our dating, was the same large megaflood that deposited the boulders in north Wenatchee. Other ice rafted erratics associated with the boulder at Wallula Gap have been used to identify the largest late Pleistocene megaflood known with a maximum discharge of $10^{-17} \times 10^{6}\ m^{3}s^{-1}$ (Benito and O'Connor, 2003).

All younger flood features that we have dated suggest that the ~17.2 ka flood recorded at north Wenatchee and Wallua Gap was the last of the floods of this large size. This is supported by salinity records from the Pacific Ocean that indicate the most recent substantial increase in freshwater input was 17 to 19 cal ka B.P (Lopes and Mix, 2009). Evidence for an older interval of reduced salinity between 22 to 25 cal ka B.P. (Lopes and Mix, 2009) may correspond to the large flood we have dated at ~22 ka at Babcock Ridge (Figure 4.3).

Our evidence that floods traveled through the northern Columbia River at ~17.2 ka indicates that the Okanogan Lobe had not advanced across the river to its maximum extent ~70 km to the south at this time. This is in contrast to the timing of the advance of the Puget Lobe to its maximum extent, which occurred at ~16.95 ka (Porter and Swanson, 1998). We speculate that the large megafloods during the 17.2 to 22.2 ka time interval may have eroded the advancing margin of the Okanogan Lobe, causing the delay in reaching its maximum extent relative to the Puget Lobe to the west.

Our new ages demonstrate a more pronounced delay of ~2.4 kyr in the timing of retreat of the Puget Lobe (~16.9 ka) (Porter and Swanson, 1998) as compared to our new chronology for retreat of the Okanagon Lobe from the Withrow moraine (14.8±1.0 ka). We suggest that this difference in timing reflects two independent controls on lobe retreat. Records of ice-rafted debris from the NE Pacific identify a large increase in flux of ice from the marine-based Juan de Fuca Lobe of the Cordilleran Ice Sheet at ~17 ka, which may have been triggered by subsurface warming at the grounding line (Cosma et al., 2008; Hendy, 2009; Hendy et al., 2002; Taylor et al., 2014). Insofar as the Puget Lobe was immediately adjacent to the Juan de Fuca Lobe, the dynamically triggered drawdown of the Juan de Fuca Lobe likely

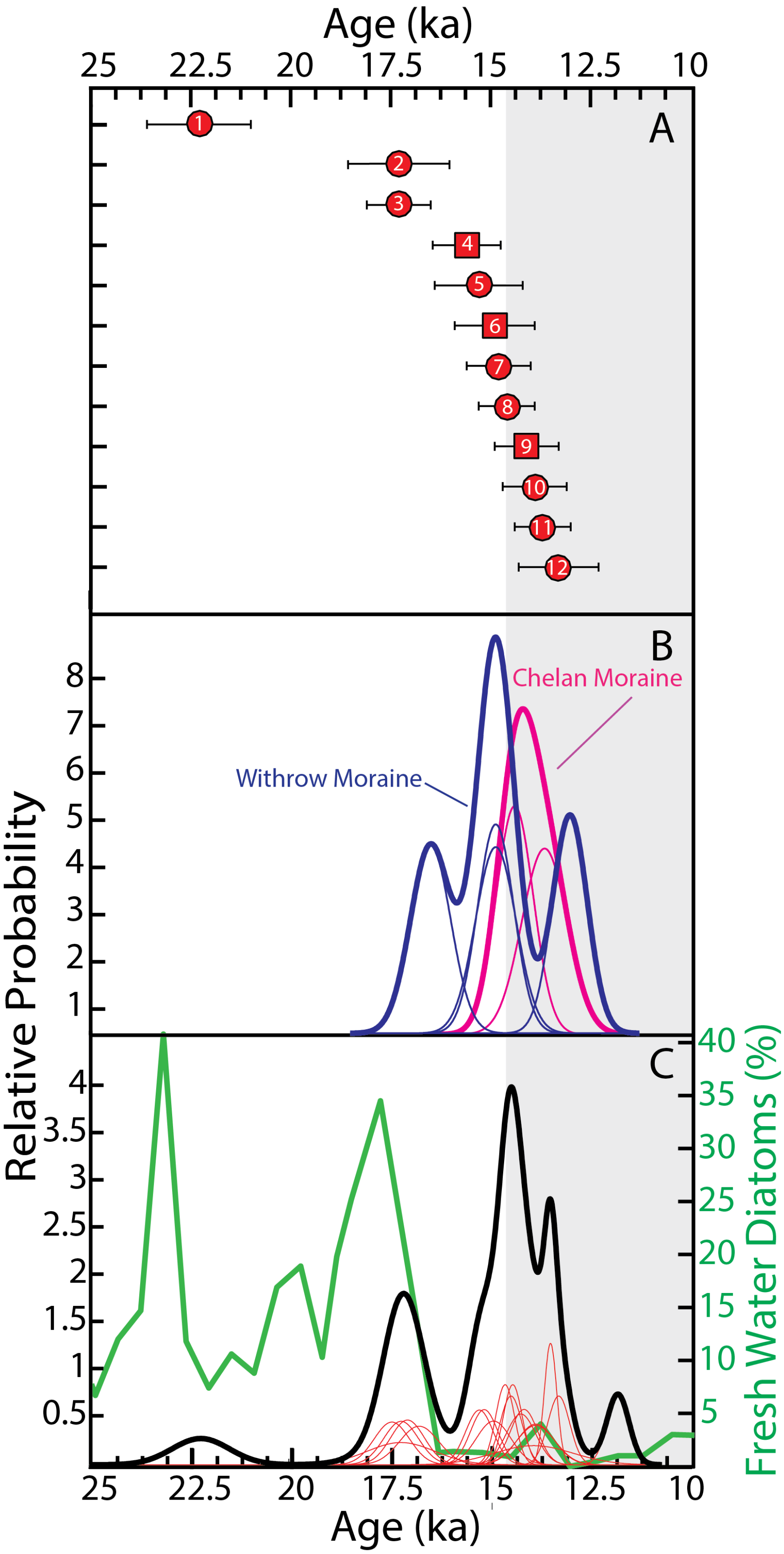
Age (ka)
25
22.5
20
17.5
15
12.5
10
A
1
2
3
4
5
6
7
8
9
10
11
12
B
Chelan Moraine
Withrow Moraine
8
7
6
5
4
3
2
1
Relative Probability
C
4
3.5
3
2.5
2
1.5
1
0.5
40
35
30
25
20
15
10
5
Fresh Water Diatoms (%)
25
22.5
20
17.5
15
12.5
10
Age (ka)

Figure 4.3: A comparison of surface exposure ages of Pleistocene deposits with records of fresh water diatom deposition in the Pacific and the presence of humans locally. The shaded grey region represent minimum timeframe of local human occupation based on the ^{14}C ages of human material found within Paisley Caves, Oregon (Gilbert et al., 2008) (A) The ages of depositional features as shown in Figure 4.2. (B) A probability density function (PDF) of the boulders from Chelan moraine (pink) and Withrow moraine (blue). (C) The PDF of all flood deposited boulders analyzed in this study (black) with individual samples shown as red lines. The green line represents the percent of fresh water diatoms recovered within Pacific sediment cores and indicate pulses of large flooding events (Lopes and Mix, 2009).

induced drawdown and thus retreat of the Puget Lobe. In contrast, our constraints for onset of retreat of the Okanagon Lobe at ~14.8 ka suggest a surface mass balance response to the abrupt onset of the Bølling warm period at ~14.7 ka, which is recorded in NE Pacific sea-surface temperature records (Hendy, 2009; Praetorius et al., 2015; Praetorius and Mix, 2014).

The Ephrata Fan represents a flood triggered by the failure of a debris dam at the southern edge of Grand Coulee (Bjornstad and Kiver, 2012; Bretz et al., 1956). Four surface exposure ages from boulders deposited on the fan indicate that the debris dam failed 14.7 ± 0.8 ka, which is a similar age as the armored bar along the Columbia upstream near Wenatchee (14.5 ± 0.7 ka). These features suggest megaflood events remained sourced from areas east of Grand Coulee and traveled through an open northern Columbia River route immediately after retreat of the Okanagon Lobe at 14.8 ± 1.0 ka.

Breckenridge, (2010) reported five ^{10}Be ages on boulders from a lateral moraine deposited by the Purcell Trench Lobe as it advanced into the Lake Pend Oreille basin (site 4) and dammed Glacial Lake Missoula. The ages range from 14.6 to 16.3 ka, with a mean age of 15.5 ± 0.9 ka (recalculated using the NENA production rate), suggesting a similar age as for the onset of retreat of the Okanogan Lobe from the Withrow moraine (14.8 ± 1.0 ka). Our one age (13.8 ± 0.8 ka) for a boulder immediately south of the outlet at Lake Pond Oreille (site 10) identifies the age of the last of the Missoula floods, and thus the last time that the Purcell Trench Lobe acted as an ice dam. Within our dating uncertainties, this flood is likely the same as is recorded by the Mattawa Fan (13.6 ± 0.7 ka) (site 11) and the Pangborn Bar (13.2 ± 1.0 ka) (site 12).

Radiocarbon ages from organic matter related to human inhabitants of the Paisley Caves in Oregon provide a minimum age for human occupation of the Pacific Northwest to 14.5 ± 0.4 ka (Gilbert et al., 2008). Our youngest site ages (13.2 ± 1.0 ka to 13.8 ± 0.8 ka) suggest that these early human populations may have witnessed these dramatic natural events and introduced them into their oral traditions.

4.6 Conclusions

New ^{10}Be ages from 11 key features associated with the late Pleistocene megafloods clarify the relationship between the Cordilleran Ice Sheet and megaflood dynamics. We show that a large megaflood occurred at ~17.2 ka and traveled through an open northern Columbia River throughway before the advance of the Okanogan Lobe and impoundment of Glacial Lake Columbia. ^{10}Be ages further indicate Okanogan Lobe retreat occurred between 14.0 to 14.8 ka and that floods that occurred after Okanogan retreat were not as large as those before blockage of the northern Columbia. The relatively late retreat of the Okanogan Lobe as compared to the Puget Lobe may reflect independent controls on ice-sheet behavior. Radiocarbon ages indicating the minimum age of human occupation of the Pacific Northwest of the United States in combination with our most recent site ages suggest humans may have witnessed some of the youngest megafloods, which dramatic character likely influenced their oral traditions.

4.7 References

Atwater, B. F., 1986, Pleistocene glacial-lake deposits of the Sanpoil River Valley, northeastern Washington: USGPO.

Baker, V. R., 1978, The Spokane Flood controversy and the Martian outflow channels: Science, v. 202, no. 4374, p. 1249-1256.

Baker, V. R., and Bunker, R. C., 1985, Cataclysmic late Pleistocene flooding from glacial Lake Missoula: A review: Quaternary Science Reviews, v. 4, no. 1, p. 1-41.

Balco, G., Briner, J., Finkel, R. C., Rayburn, J. A., Ridge, J. C., and Schaefer, J. M., 2009, Regional beryllium-10 production rate calibration for late-glacial northeastern North America: Quaternary Geochronology, v. 4, no. 2, p. 93-107.

Ballantyne, C. K., and Stone, J. O., 2012, Did large ice caps persist on low ground in north-west Scotland during the Lateglacial Interstade?: Journal of Quaternary Science, v. 27, no. 3, p. 297-306.

Benito, G., and O'Connor, J. E., 2003, Number and size of last-glacial Missoula floods in the Columbia River valley between the Pasco Basin, Washington, and Portland, Oregon: Geological Society of America Bulletin, v. 115, no. 5, p. 624-638.

Bjornstad, B. N., and Kiver, E. P., 2012, On the Trail of the Ice Age Floods: The Northern Reaches: A Geological Field Guide to Northern Idaho and the Channeled Scabland, Keokee Books.

Breckenridge, R. M., New Cosmogenic 10BE Surface Exposure Ages for the Purcell Trench Lobe of the Cordilleran Ice Sheet in Idaho, in Proceedings 2010 GSA Denver Annual Meeting2010.

Bretz, J. H., 1923, The channeled scablands of the Columbia Plateau: The Journal of Geology, v. 31, no. 8, p. 617-649.

Bretz, J. H., 1925, The Spokane flood beyond the channeled scablands: The Journal of Geology, p. 97-115.

Bretz, J.H., , 1928, The channeled scabland of eastern Washington: Geographical Review, v. 18, no. 3, p. 446-477.

Bretz, J. H., Smith, H. U., and Neff, G. E., 1956, Channeled Scabland of Washington: New data and interpretations: Geological Society of America Bulletin, v. 67, no. 8, p. 957-1049.

Cosma, T. N., Hendy, I. L., and Chang, A. S., 2008, Chronological constraints on Cordilleran Ice Sheet glaciomarine sedimentation from core MD02-2496 off Vancouver Island (western Canada): Quaternary Science Reviews, v. 27, no. 9, p. 941-955.

Gilbert, M. T. P., Jenkins, D. L., Götherstrom, A., Naveran, N., Sanchez, J. J., Hofreiter, M., Thomsen, P. F., Binladen, J., Higham, T. F., and Yohe, R. M., 2008, DNA from pre-Clovis human coprolites in Oregon, North America: Science, v. 320, no. 5877, p. 786-789.

Hendy, I., 2009, A fresh perspective on the Cordilleran Ice Sheet: Geology, v. 37, no. 1, p. 95-96.

Hendy, I. L., Kennett, J. P., Roark, E., and Ingram, B. L., 2002, Apparent synchroneity of submillennial scale climate events between Greenland and Santa Barbara Basin, California from 30–10ka: Quaternary Science Reviews, v. 21, no. 10, p. 1167-1184.

Lal, D., 1991, Cosmic ray labeling of erosion surfaces: in situ nuclide production rates and erosion models: Earth and Planetary Science Letters, v. 104, no. 2-4, p. 424-439.

Licciardi, J. M., 2000, Alpine glacier and pluvial lake records of late Pleistocene climate variability in the western United States.

Lopes, C., and Mix, A., 2009, Pleistocene megafloods in the northeast Pacific: Geology, v. 37, no. 1, p. 79-82.

O'Connor, J. E., and Baker, V. R., 1992, Magnitudes and implications of peak discharges from glacial Lake Missoula: Geological Society of America Bulletin, v. 104, no. 3, p. 267-279.

Porter, S. C., and Swanson, T. W., 1998, Radiocarbon age constraints on rates of advance and retreat of the Puget lobe of the Cordilleran ice sheet during the last glaciation: Quaternary Research, v. 50, no. 3, p. 205-213.

Praetorius, S., Mix, A., Walczak, M., Wolhowe, M., Addison, J., and Prahl, F., 2015, North Pacific deglacial hypoxic events linked to abrupt ocean warming: Nature, v. 527, no. 7578, p. 362-366.

Praetorius, S. K., and Mix, A. C., 2014, Synchronization of North Pacific and Greenland climates preceded abrupt deglacial warming: Science, v. 345, no. 6195, p. 444-448.

Stone, J. O., 2000, Air pressure and cosmogenic isotope production: Journal of Geophysical Research: Solid Earth, v. 105, no. B10, p. 23753-23759.

Taylor, M., Hendy, I., and Pak, D., 2014, Deglacial ocean warming and marine margin retreat of the Cordilleran Ice Sheet in the North Pacific Ocean: Earth and Planetary Science Letters, v. 403, p. 89-98.

Waitt, R. B., 1980, About forty last-glacial Lake Missoula jökulhlaups through southern Washington: The Journal of Geology, p. 653-679.

Waitt, R. B., 1985, Case for periodic, colossal jökulhlaups from Pleistocene glacial Lake Missoula: Geological Society of America Bulletin, v. 96, no. 10, p. 1271-1286.

Waitt, R. B., Denlinger, R. P., and O'Connor, J. E., 2009, Many monstrous Missoula floods down Channeled Scabland and Columbia valley: Field Guides, v. 15, p. 775-844.

Weis, P. L., Richmond, G. M., and Washinston, D., 1902, Geological Survey Research 1965: US Geological Survey Professional Paper, p. 128.

Chapter 5

Conclusions

This dissertation contains three geochronological studies about the timing of paleomagnetic change, Cordilleran Ice Sheet retreat and the late Pleistocene megaflood magnitude and routing through time. The results of which shed light on the processes associated with geomagnetic excursions, geomagnetic reversals, Cordilleran Ice Sheet retreat, and the dynamics of the largest freshwater floods in the geologic record.

5.1 Chapter Summaries

In Chapter 2, we revisited the basalt record of a paleomagnetic anomaly on the Island of Floreana in the Galapagos to better constrain the timing of this event. We define a new $^{40}Ar/^{39}Ar$ age of 925.7 ± 4.6 ka (2σ) for this geomagnetic anomaly, which indicates that it is associated with the Santa Rosa Excursion. A compilation of our data and previous work reveal a dramatic change in VGP and geomagnetic field strength during this time. Thus, we confirm the global extent of this excursion known to have resulted in an 86% reduction in absolute field intensity in the equatorial region (Wang and Kent, 2013). Together, the sedimentary records and igneous-rock data are convincing evidence of global field behavior that deviated markedly from an axial geocentric dipole. Our data suggest that the Santa Rosa Excursion was both a significant and short-lived geomagnetic anomaly, illustrating the potential for the geodynamo to dramatically alter the geomagnetic field in a few millennia. The global extent and short duration (sediment records) and the dramatic decrease in field intensity (igneous-rock data) of this excursion should thus place important constraints on models of the geodynamo.

In Chapter 3, we revisited the basalt record of the most recent paleomagnetic reversal on the island of Tahiti Nui in the Society Islands to better constrain the timing of this event. A compilation of our data and previous work suggests a prolonged period of instability that extends from the M-B reversal at ~773 ka to ~808 ka, nearly twice as long as previously considered. The frequency of the large polarity changes within this 35-kyr window suggests that geomagnetic changes were occurring on a millennial and perhaps centennial timescale. These records are coincident with the start of the precursor phase signified by a field intensity reduction that is well expressed in the PISO-1500 stack (Channell et al., 2009). Here we offer important new insights into the short precursor history of a reversing field and the rapid changing field dynamics during periods of low-dipole intensity.

In Chapter 4, we use ^{10}Be surface exposure dating to gain insight into the relationship between the growth and decay of the Cordilleran Ice Sheet and the magnitude and routing of the late Pleistocene megafloods. Surface exposure ages on several iceberg deposited boulders indicates a large megaflood occurred at ~17.2 ka and traveled through an open northern Columbia River throughway before the advance of the Okanogan Lobe and impoundment of Glacial Lake Columbia. Six surface exposure ages from two sites show that the Okanogan Lobe retreat occurred between 14.0 to 14.8 ka and that floods that occurred after Okanogan retreat were not as large as those before blockage of the northern Columbia. Later retreat of the Okanogan Lobe as compared to the Puget Lobe may reflect independent controls on ice-sheet behavior. Radiocarbon ages indicating the minimum age of human occupation of the Pacific Northwest of the United States in combination with our most recent site ages suggest humans may have witnessed some of the youngest megafloods; the dramatic character of these events may have influenced their oral traditions.

5.2 References:

Channell, J., Xuan, C., and Hodell, D., 2009, Stacking paleointensity and oxygen isotope data for the last 1.5 Myr (PISO-1500): Earth and Planetary Science Letters, v. 283, no. 1, p. 14-23.

Wang, H. P., and Kent, D. V., 2013, A paleointensity technique for multidomain igneous rocks: Geochemistry Geophysics Geosystems, v. 14, no. 10, p. 4195-4213.

APPENDICES

Appendix A - Identification of the short-lived Santa Rosa geomagnetic excursion in lavas on Floreana (Galapagos) by $^{40}Ar/^{39}Ar$ geochronology

A.1 Selected ages

The weighted plateau used in the reported age contains only data from ‘layer A’ samples (the bottom holocrystalline portion of the flow). These ages are highly reproducible, with all samples falling within one sigma confidence of each other. The layer 'A' samples include three different samples taken four meters apart and each were measured twice, one time using 15 mg and one time using 25 mg of highly purified and acid-cleaned groundmass separate (grain size 106-180 μm). The incremental heating patterns that are highly reproducible between analyses and that can be explained through simple low and high temperature recoil with minimal evidence of excess ^{40}Ar (e.g. Koppers et al., 2000). The $^{39}Ar(K)$ and $^{37}Ar(Ca)$ (K/Ca) curves for the different samples show a relatively flat plateau in the low and middle temperature increments, indicating that alteration and weathering have been effectively removed from the samples during sample preparation, acid leaching, hand picking and low temperature heating and that most of the age spectra reflects the outgassing of the high K magmatic phase present interstitially between the crystal network in the Floreana groundmasses (see panels A). The low temperature discordant incremental heating steps are likely reflecting the preferential degassing and recoil effects of fine-grained secondary (e.g. clay) phases that remain resident in the groundmass separates, even after the applied intense acid leaching protocol. Higher K/Ca ratios in combination with high Cl and higher atmospheric components (see orange lines in panels D) provide direct evidence for the outgassing of these alteration phases. The higher ages are explained by $^{39}Ar[K]$ recoil occurring during irradiation of these nominally very fine grained alteration phases, but this recoil effect resolves completely with the age plateaus, which are consistent within the 2σ confidence interval of the age plateaus. The high temperature discordant heating steps on the other hand are likely reflecting the preferential degassing of both plagioclase and clinopyroxene, which are abundant mineral phases in the dated groundmasses. This is evidenced by the lower K/Ca ratios approaching values below 0.05 in many cases whereby the outgassing of ^{37}Ar[Ca] is strongest (see purple lines in panels D) compared to the rather constant outgassing at low and intermediate temperatures. The lower ages are likely a combination of ^{39}Ar[K] and ^{37}Ar[Ca] recoil with the former being partitioned in the high temperature phases after removal from the secondary phases at low temperatures and the latter being lost from the high Ca phases such as plagioclase and clinopyroxene during irradiation, and which effect is strongest at high temperatures when the high-Ca phases are preferentially outgassing (e.g. Koppers et al., 2000, 2004). The incremental heating steps in the age plateaus, used to calculate the weighted mean ages for the groundmass, typically are characterized by the lowest atmospheric components, consistent outgassing of the radiogenic argon component (see green lines in panels D), and K/Ca ratios that are relatively high and consistent, indicating that a singular high K component is outgassing.

Furthermore, for layer ‘A’ samples the plateau and isochron ages are internally concordant and the ages between the different samples are highly reproducible. The only discordance is observed in the higher total fusion ages, which is readily explained by the low temperature ^{39}Ar[k] recoil loss typical for groundmass samples that have some fine-grained alteration phases remaining (Koppers et al., 2000). For the individual groundmass analyses, the MSWD's are low between 0.7 and 1.4 (n=5) and 2.4 (n=1) and spreading factors in the inverse isochrons range between 12.2% and 63%. The $^{40}Ar/^{36}Ar$ intercept values are typically within error with the 295.5 value of atmospheric argon or they are slightly subatmospheric, but there is no evidence for the presence of excess ^{40}Ar beyond the 2σ uncertainties given. For these reasons the the six plateau ages for the layer 'A' groundmass samples are deemed reliable and robustly reflect the eruption age of Floreana lava flow GA79.

Layer 'B' and 'C' samples from the top of lava flow GA79 were excluded from the population used to determine the age of this flow. The layer 'B' portion of the flow has a higher vesicularity and lower grain size than layer 'A'. Layer 'C' samples were from the frothy highly oxidized and glassy top portion of the flow. These samples display evidence for recoil in especially the low temperature sections of the age spectra, they have different and varying mean K/Ca values and these samples show increasingly erratic K/Ca curves. The weighted mean ages of the age plateaus of layers 'B' and 'C' show more scatter between 905 and 936 Ma and are thus less reproducible than layer 'A'. These samples also have different K/Ca spectra with either higher or lower mean K/Ca values, reflecting the fact that layers 'B' and 'C' have different phase modalities (i.e. more devitrified glass, lower crystallinity with lesser modal amounts of plagioclase and clinopyroxene, and stronger alteration throughout the groundmasses) than layer 'A' samples. Some minor excess ^{40}Ar is likely resident in the more abundant glass phase and therefore display higher apparent ages, although we don't observe any significant amount of excess ^{40}Ar present in the (sub)atmospheric $^{40}Ar/^{36}Ar$ intercept values from the inverse isochron analyses.

Table A.1: Floreana Age Data

				Age Spectrum							Total Fusion		Inverse Isochron Analyses			
Sample Number	Experiment Number	Sample Type	Weight (Mg)	Age ± 2σ (ka)	^{39}Ar (%)	K/Ca	MSWD	P (%)	n	N	Age ± 2σ (ka)	K/Ca	Age ± 2σ (ka)	^{40}Ar/ ^{36}Ar intercept	MSWD	P (%)
44A-Argon-2	13D07373	Groundmass	15	**927.9 ± 9.7**	71	0.03	0.83	68	20	34	1004.6 ± 12.5	0.120	926.3 ± 12.2	296.74 ± 5.20	0.86	63
44A-Argon-2	13D08071	Groundmass	25	**925.3 ± 7.9**	65	0.217	1.37	14	17	39	1047.7 ± 13.2	0.151	930.1 ± 16.0	290.32 ± 15.25	1.43	12
44A-Argon-3	13D08125	Groundmass	15	**924.2 ± 9.3**	65	0.157	1.32	16	19	39	975.1 ± 10.6	0.145	937.0 ± 11.7	285.34 ± 6.89	0.92	55
44A-Argon-3	13D07446	Groundmass	25	**922.0 ± 10.2**	67	0.235	0.99	46	14	34	941.9 ± 12.3	0.115	930.0 ± 19.0	288.09 ± 15.07	1.00	45
44A-Argon-5	13D07493	Groundmass	15	**929.0 ±11.8**	68	0.230	2.39	0	16	34	993.5 ± 10.4	0.137	951.9 ± 19.2	278.06 ± 12.78	1.73	4
44A-Argon-5	13D08189	Groundmass	25	**924.8 ± 8.7**	46	0.307	0.68	77	13	39	1083.9 ± 15.8	0.168	908.1 ± 52.1	308.88 ± 42.36	0.70	74
44A-Combined				**925.7 ± 4.6**	63	0.050	1.23	6	99	219	1013.8 ± 6.1	0.140	930.7 ± 6.4	291.25 ± 3.79	1.18	11
44B-Argon-1	13D07565	Groundmass	15	**904.8 ± 8.5**	79	0.306	1.06	39	17	34	906.6 ± 10.3	0.174	881.4 ± 21.2	312.60 ± 14.17	0.69	79
44B-Argon-5	13D07612	Groundmass	15	**936.2 ± 13.1**	77	0.096	0.58	93	21	34	1307.7 ± 40.9	0.088	936.7 ± 26.6	295.37 ± 10.50	0.62	90
44B-Combined				**913.2 ± 8.0**	78	0.117	1.26	14	38	68	1065.3 ± 17.5	0.125	893.4 ± 14.4	308.08 ± 7.78	0.99	48
44C-Argon-2	13D07659	Groundmass	15	**955.5 ± 17.8**	68	0.171	0.68	81	17	34	1071.9 ± 46.0	0.115	933.8 ± 55.7	298.80 ± 8.04	0.69	80
44C-Argon-2	13D08243	Groundmass	25	**959.2 ± 11.6**	61	0.168	0.87	62	20	39	1106.9 ± 33.8	0.146	957.2 ± 41.7	295.83 ± 6.7	0.92	55
44C-Combined				**958.1 ± 9.9**	64	0.169	0.77	84	37	73	1093.0 ± 27.5	0.132	949.5 ± 32.8	296.90 ± 5.1	0.78	82

P is the chi-squared probability

MSWD is the mean square of the weighted deviatants.

n is the number steps used in the age calculation

N is the total number of incremental heating steps

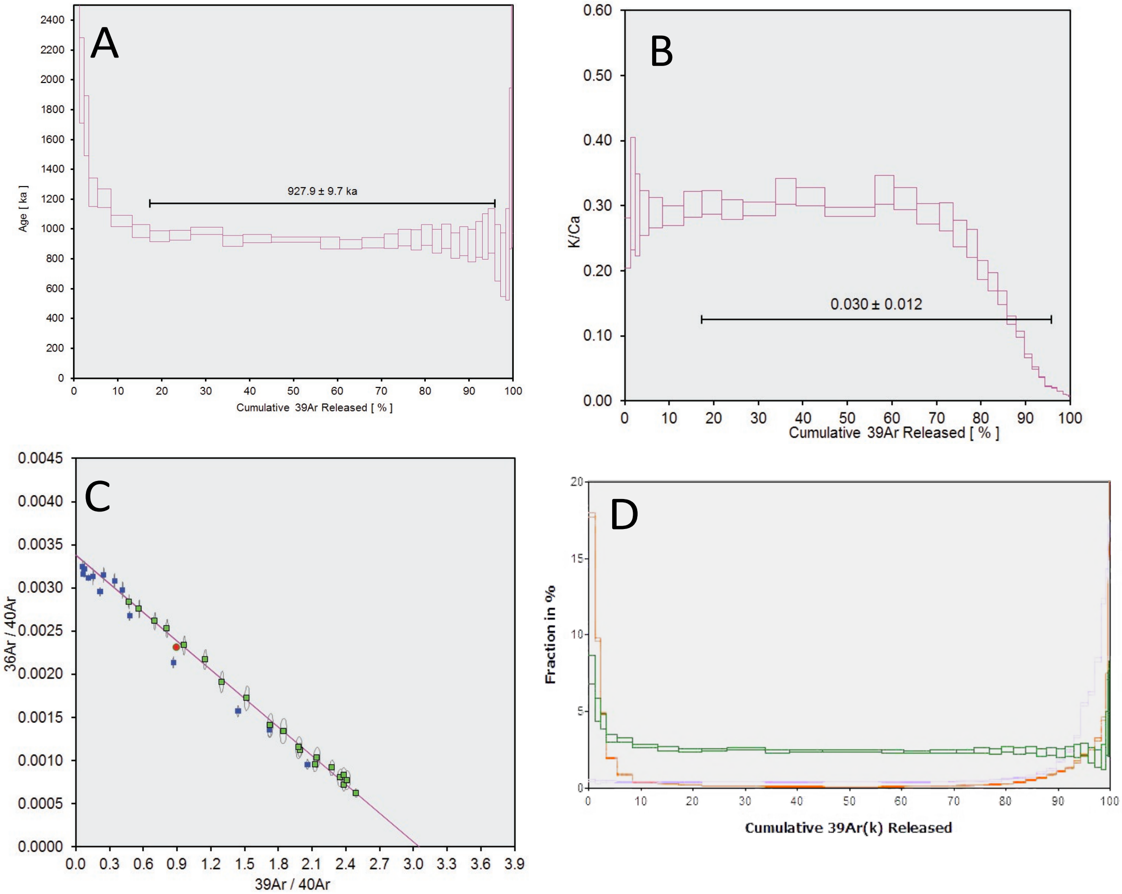

Figure A.1: Argon analysis of the 15mg split of sample 2 from ‘layer A’ (holocrystaline portion) of the flow. All steps included in the age plateau were used in the reported weighted mean age for this flow (see Figure 2.1 in main text). (**A**) The incremental heating plateau with age uncertainties reported at the 2σ confidence level. Early heating steps are excluded as they represent discordant incremental heating steps and are likely reflecting ^{39}Ar(K) recoil through the preferential degassing of fine-grained secondary (e.g. clay) phases that remain resident in the groundmass separates, even after the applied intense acid leaching protocol, but are resolved at higher temperatures and within the age plateau at the 2σ confidence interval. High temperature heating steps are also excluded due to high temperature ^{37}Ar(Ca) and ^{39}Ar(K) recoil. (**B**) The K/Ca curve for the incremental heating experiment. (**C**) The inverse isochron, whereby green squares represent points within the selected plateau and blue squares are excluded points from the heating plateau. The red circle represents the total fusion value. (**D**) Degassing patterns for the incremental heating experiment, normalized against the size of the gas released in each incremental heating step. The green boxes represent radiogenic ^{40}Ar*, the orange represent the atmospheric component (^{36}Ar) and purple is the Ca proxy (^{37}Ar). The concentration of Ca increases toward the higher temperatures by the preferential degassing of plagioclase and clinopyroxene micro-crystals in the groundmass (also reflected in the decreasing K/Ca ratio). The atmospheric signature shows high fraction percent during the low temperature heating steps, likely due to alteration. In the higher heating steps this atmospheric signature also increases, likely due to the presence of trapped atmospheric components during the formation of the lava flow.

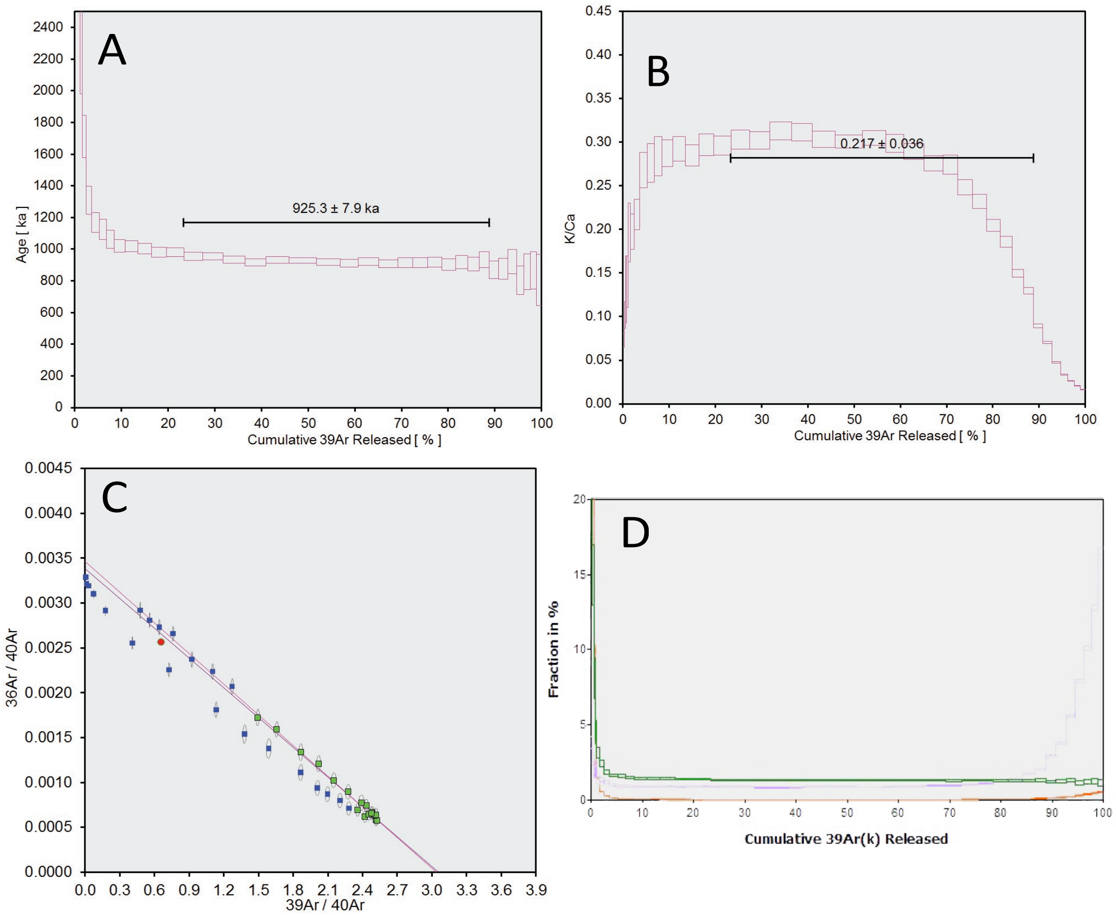

Figure A.2: Argon analysis of the 25mg split of sample 2 from ‘layer A’ (holocrystaline portion) of the flow. All steps included in the age plateau were used in the reported weighted mean age for this flow (see Figure 2.1 in main text). (**A**) The incremental heating plateau with age uncertainties reported at the 2σ confidence level. Early heating steps are excluded as they represent discordant incremental heating steps and are likely reflecting ^{39}Ar(K) recoil through the preferential degassing of fine-grained secondary (e.g. clay) phases that remain resident in the groundmass separates, even after the applied intense acid leaching protocol, but are resolved at higher temperatures and within the age plateau at the 2σ confidence interval. High temperature heating steps are also excluded due to high temperature ^{37}Ar(Ca) and ^{39}Ar(K) recoil. (**B**) The K/Ca curve for the incremental heating experiment. (**C**) The inverse isochron, whereby green squares represent points within the selected plateau and blue squares are excluded points from the heating plateau. The red circle represents the total fusion value. (**D**) Degassing patterns for the incremental heating experiment, normalized against the size of the gas released in each incremental heating step. The green boxes represent radiogenic ^{40}Ar*, the orange represent the atmospheric component (^{36}Ar) and purple is the Ca proxy (^{37}Ar). The concentration of Ca increases toward the higher temperatures by the preferential degassing of plagioclase and clinopyroxene micro-crystals in the groundmass (also reflected in the decreasing K/Ca ratio). The atmospheric signature shows high fraction percent during the low temperature heating steps, likely due to alteration. In the higher heating steps this atmospheric signature also increases, likely due to the presence of trapped atmospheric components during the formation of the lava flow.

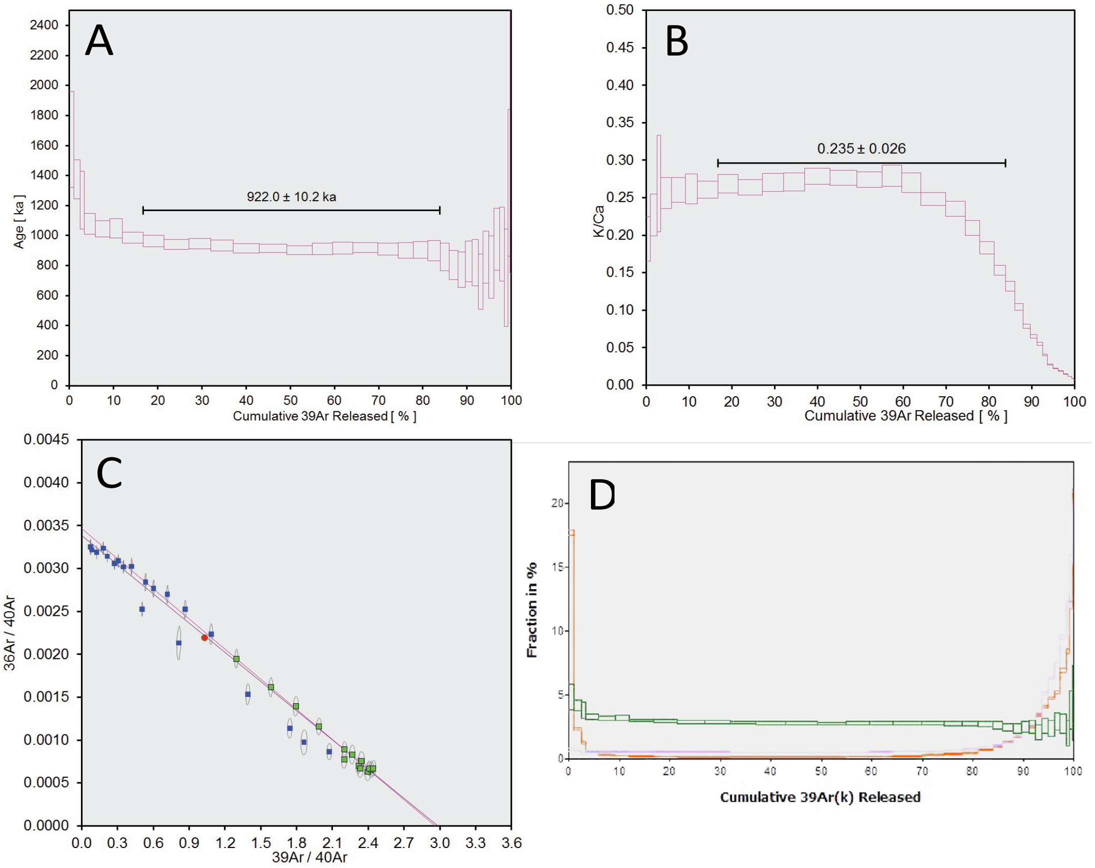

Figure A.3: Argon analysis of the 15mg split of sample 3 from ‘layer A’ (holocrystaline portion) of the flow. All steps included in the age plateau were used in the reported weighted mean age for this flow (see Figure 2.1 in main text). (**A**) The incremental heating plateau with age uncertainties reported at the 2σ confidence level. Early heating steps are excluded as they represent discordant incremental heating steps and are likely reflecting ^{39}Ar(K) recoil through the preferential degassing of fine-grained secondary (e.g. clay) phases that remain resident in the groundmass separates, even after the applied intense acid leaching protocol, but are resolved at higher temperatures and within the age plateau at the 2σ confidence interval. High temperature heating steps are also excluded due to high temperature ^{37}Ar(Ca) and ^{39}Ar(K) recoil. (**B**) The K/Ca curve for the incremental heating experiment. (**C**) The inverse isochron, whereby green squares represent points within the selected plateau and blue squares are excluded points from the heating plateau. The red circle represents the total fusion value. (**D**) Degassing patterns for the incremental heating experiment, normalized against the size of the gas released in each incremental heating step. The green boxes represent radiogenic ^{40}Ar*, the orange represent the atmospheric component (^{36}Ar) and purple is the Ca proxy (^{37}Ar). The concentration of Ca increases toward the higher temperatures by the preferential degassing of plagioclase and clinopyroxene micro-crystals in the groundmass (also reflected in the decreasing K/Ca ratio). The atmospheric signature shows high fraction percent during the low temperature heating steps, likely due to alteration. In the higher heating steps this atmospheric signature also increases, likely due to the presence of trapped atmospheric components during the formation of the lava flow.

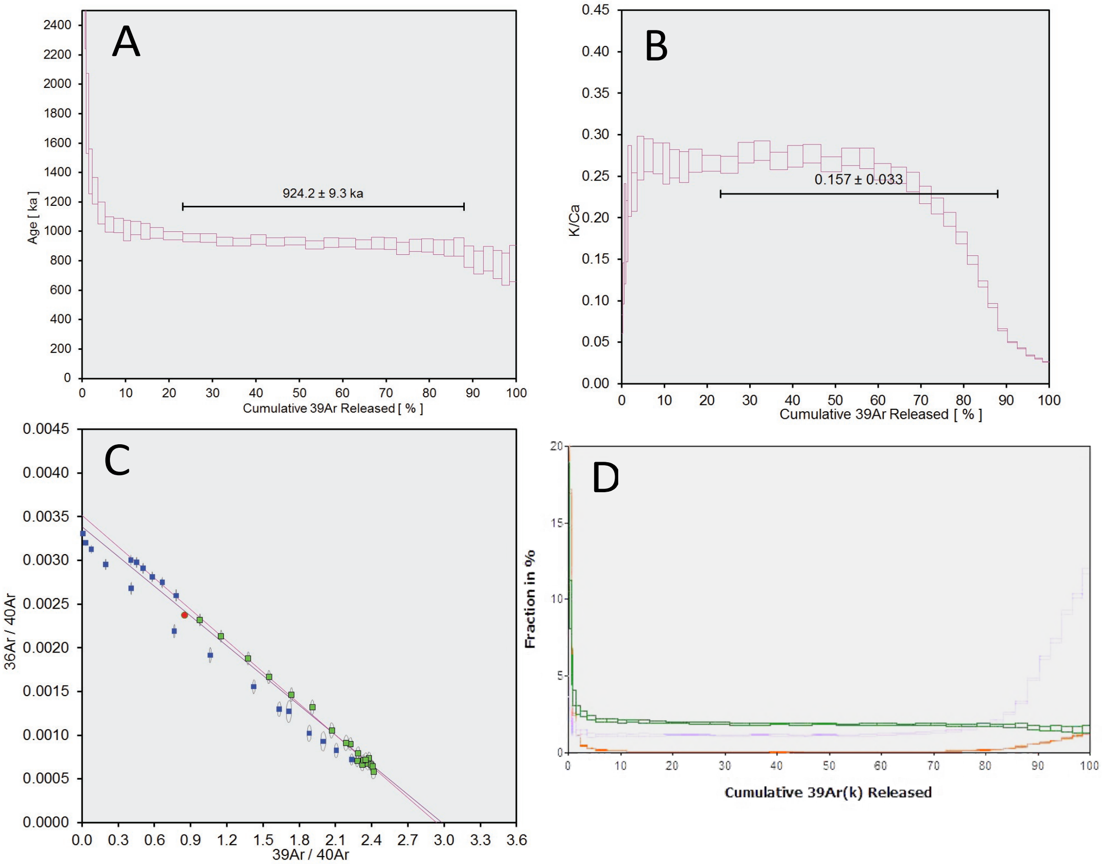

Figure A.4: Argon analysis of the 25mg split of sample 3 from 'layer A' (holocrystaline portion) of the flow. All steps included in the age plateau were used in the reported weighted mean age for this flow (see Figure 2.1 in main text). (**A**) The incremental heating plateau with age uncertainties reported at the 2σ confidence level. Early heating steps are excluded as they represent discordant incremental heating steps and are likely reflecting ^{39}Ar(K) recoil through the preferential degassing of fine-grained secondary (e.g. clay) phases that remain resident in the groundmass separates, even after the applied intense acid leaching protocol, but are resolved at higher temperatures and within the age plateau at the 2σ confidence interval. High temperature heating steps are also excluded due to high temperature ^{37}Ar(Ca) and ^{39}Ar(K) recoil. (**B**) The K/Ca curve for the incremental heating experiment. (**C**) The inverse isochron, whereby green squares represent points within the selected plateau and blue squares are excluded points from the heating plateau. The red circle represents the total fusion value. (**D**) Degassing patterns for the incremental heating experiment, normalized against the size of the gas released in each incremental heating step. The green boxes represent radiogenic ^{40}Ar*, the orange represent the atmospheric component (^{36}Ar) and purple is the Ca proxy (^{37}Ar). The concentration of Ca increases toward the higher temperatures by the preferential degassing of plagioclase and clinopyroxene micro-crystals in the groundmass (also reflected in the decreasing K/Ca ratio). The atmospheric signature shows high fraction percent during the low temperature heating steps, likely due to alteration. In the higher heating steps this atmospheric signature also increases, likely due to the presence of trapped atmospheric components during the formation of the lava flow.

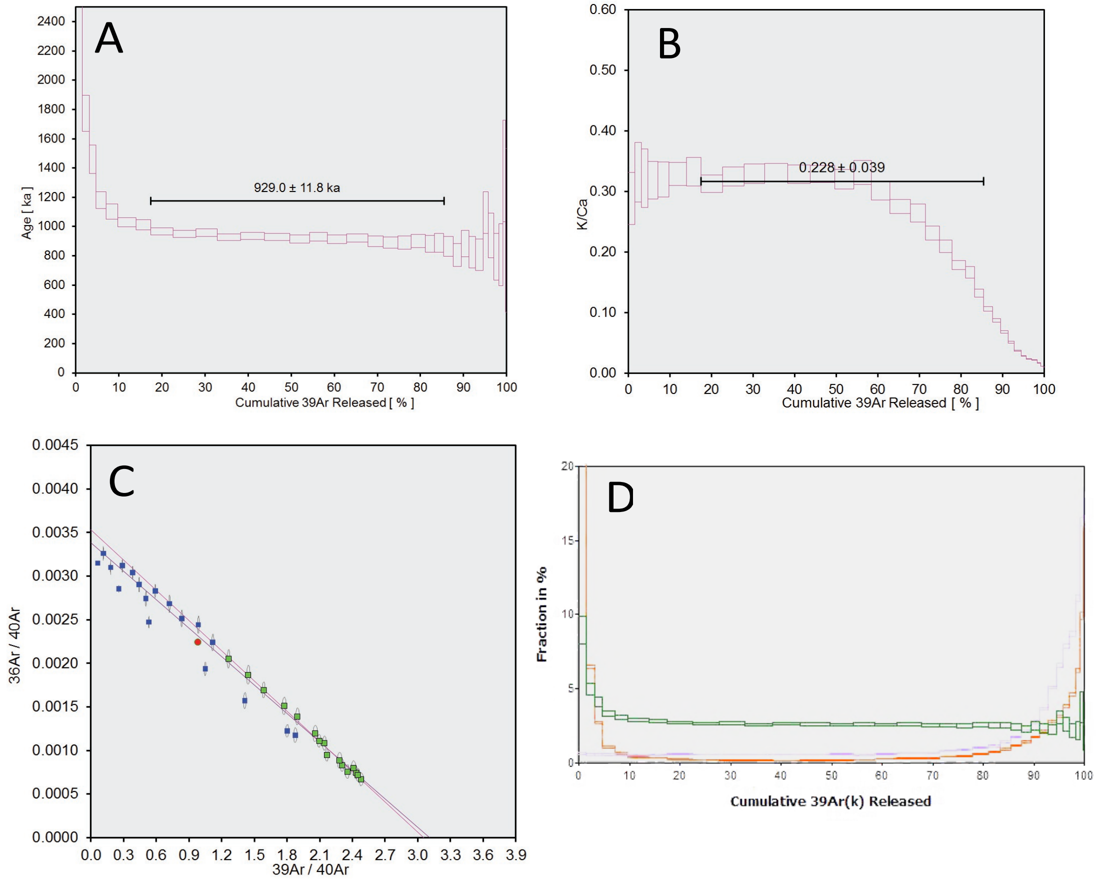

Figure A.5: Argon analysis of the 15mg split of sample 5 from 'layer A' (holocrystaline portion) of the flow. All steps included in the age plateau were used in the reported weighted mean age for this flow (see Figure 2.1 in main text). (**A**) The incremental heating plateau with age uncertainties reported at the 2σ confidence level. Early heating steps are excluded as they represent discordant incremental heating steps and are likely reflecting ^{39}Ar(K) recoil through the preferential degassing of fine-grained secondary (e.g. clay) phases that remain resident in the groundmass separates, even after the applied intense acid leaching protocol, but are resolved at higher temperatures and within the age plateau at the 2σ confidence interval. High temperature heating steps are also excluded due to high temperature ^{37}Ar(Ca) and ^{39}Ar(K) recoil. (**B**) The K/Ca curve for the incremental heating experiment. (**C**) The inverse isochron, whereby green squares represent points within the selected plateau and blue squares are excluded points from the heating plateau. The red circle represents the total fusion value. (**D**) Degassing patterns for the incremental heating experiment, normalized against the size of the gas released in each incremental heating step. The green boxes represent radiogenic ^{40}Ar*, the orange represent the atmospheric component (^{36}Ar) and purple is the Ca proxy (^{37}Ar). The concentration of Ca increases toward the higher temperatures by the preferential degassing of plagioclase and clinopyroxene micro-crystals in the groundmass (also reflected in the decreasing K/Ca ratio). The atmospheric signature shows high fraction percent during the low temperature heating steps, likely due to alteration. In the higher heating steps this atmospheric signature also increases, likely due to the presence of trapped atmospheric components during the formation of the lava flow.

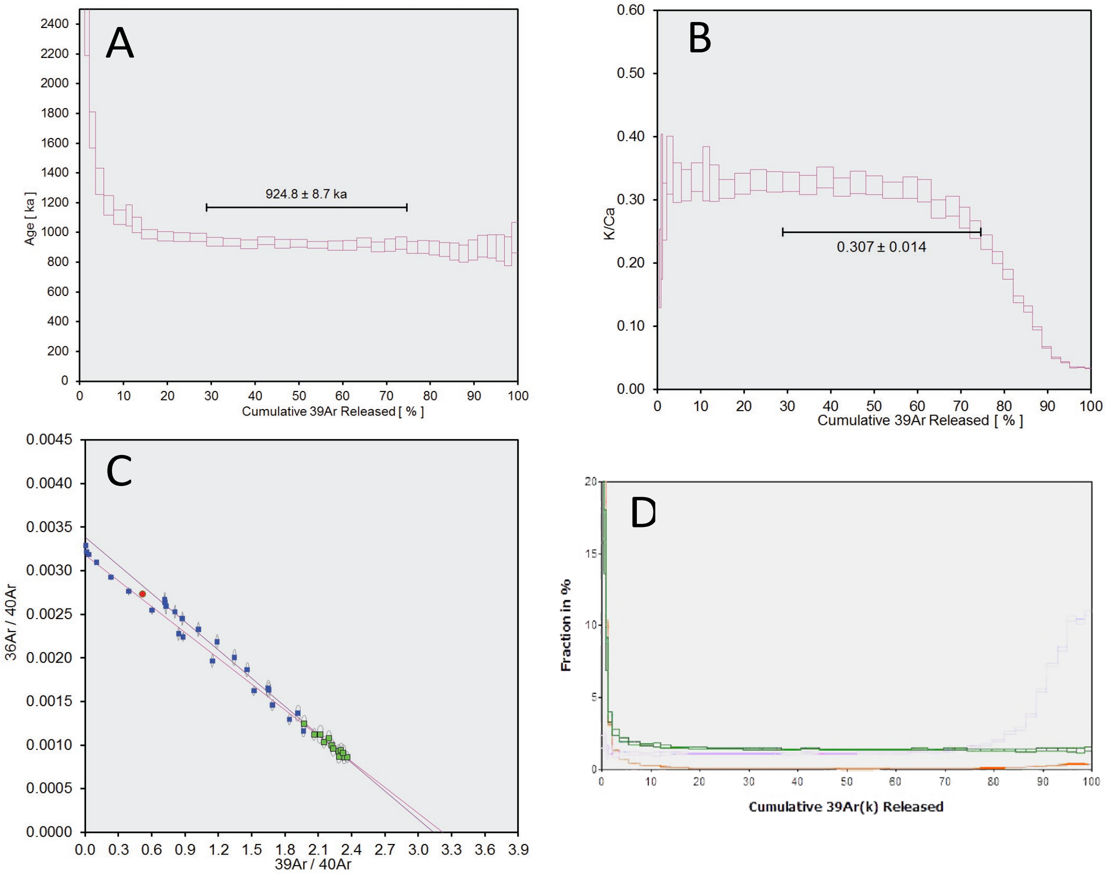

Figure A.6: Argon analysis of the 25mg split of sample 5 from 'layer A' (holocrystaline portion) of the flow. All steps included in the age plateau were used in the reported weighted mean age for this flow (see Figure 2.1 in main text). (**A**) The incremental heating plateau with age uncertainties reported at the 2σ confidence level. Early heating steps are excluded as they represent discordant incremental heating steps and are likely reflecting ^{39}Ar(K) recoil through the preferential degassing of fine-grained secondary (e.g. clay) phases that remain resident in the groundmass separates, even after the applied intense acid leaching protocol, but are resolved at higher temperatures and within the age plateau at the 2σ confidence interval. High temperature heating steps are also excluded due to high temperature ^{37}Ar(Ca) and ^{39}Ar(K) recoil. (**B**) The K/Ca curve for the incremental heating experiment. (**C**) The inverse isochron, whereby green squares represent points within the selected plateau and blue squares are excluded points from the heating plateau. The red circle represents the total fusion value. (**D**) Degassing patterns for the incremental heating experiment, normalized against the size of the gas released in each incremental heating step. The green boxes represent radiogenic ^{40}Ar*, the orange represent the atmospheric component (^{36}Ar) and purple is the Ca proxy (^{37}Ar). The concentration of Ca increases toward the higher temperatures by the preferential degassing of plagioclase and clinopyroxene micro-crystals in the groundmass (also reflected in the decreasing K/Ca ratio). The atmospheric signature shows high fraction percent during the low temperature heating steps, likely due to alteration. In the higher heating steps this atmospheric signature also increases, likely due to the presence of trapped atmospheric components during the formation of the lava flow.

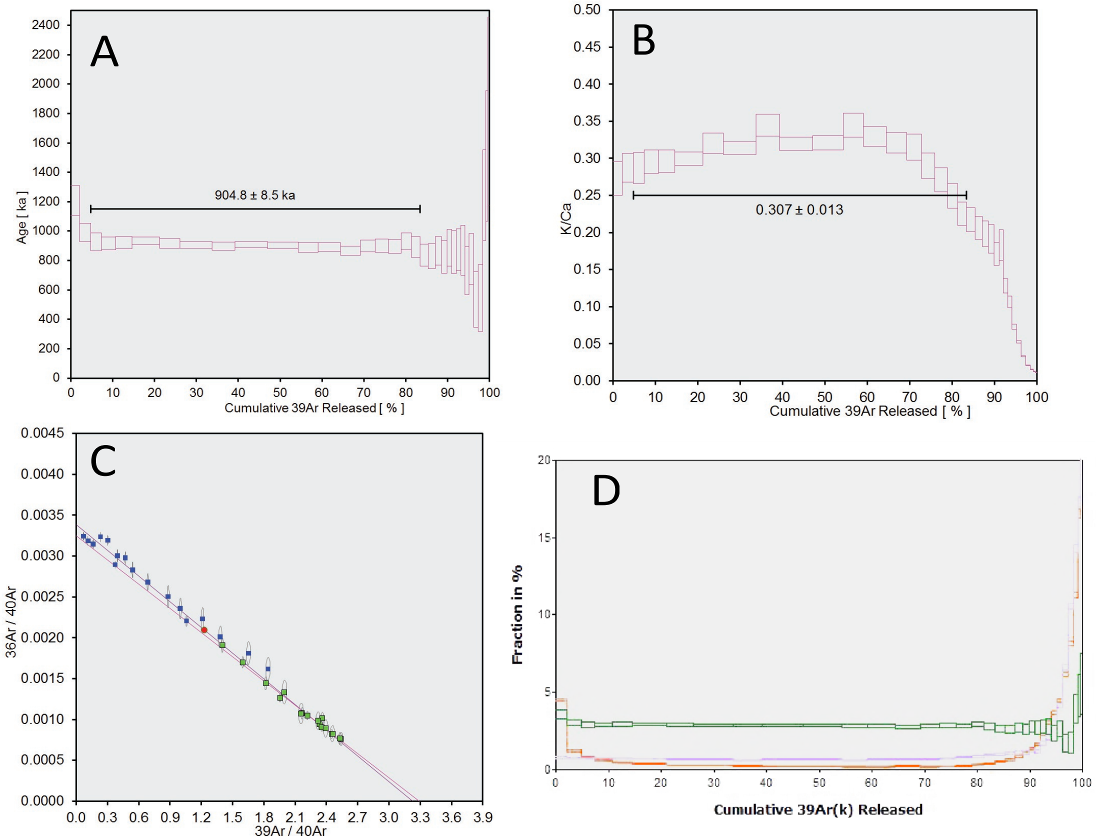

Figure A.7: Argon analysis of the 15mg split of sample 1 from 'layer B' (intermediate vesicular portion) of the flow. The weighted plateau age was not used in the reported weighted mean age for this flow. (**A**) The incremental heating plateau with age uncertainties reported at the 2σ confidence level. Early heating steps are excluded as they represent discordant incremental heating steps and are likely reflecting ^{39}Ar(K) recoil through the preferential degassing of fine-grained secondary (e.g. clay) phases that remain resident in the groundmass separates, even after the applied intense acid leaching protocol, but are resolved at higher temperatures and within the age plateau at the 2σ confidence interval. High temperature heating steps are also excluded due to high temperature ^{37}Ar(Ca) and ^{39}Ar(K) recoil. (**B**) The K/Ca curve for the incremental heating experiment. (**C**) The inverse isochron, whereby green squares represent points within the selected plateau and blue squares are excluded points from the heating plateau. The red circle represents the total fusion value. (**D**) Degassing patterns for the incremental heating experiment, normalized against the size of the gas released in each incremental heating step. The green boxes represent radiogenic ^{40}Ar*, the orange represent the atmospheric component (^{36}Ar) and purple is the Ca proxy (^{37}Ar). The concentration of Ca increases toward the higher temperatures by the preferential degassing of plagioclase and clinopyroxene micro-crystals in the groundmass (also reflected in the decreasing K/Ca ratio). The atmospheric signature shows high fraction percent during the low temperature heating steps, likely due to alteration. In the higher heating steps this atmospheric signature also increases, likely due to the presence of trapped atmospheric components during the formation of the lava flow. Layer 'B' samples have weighted plateau ages that are not reproducible at the 2σ uncertainty level and which have highly variable K/Ca signatures indicating heterogeneity within the upper part of the ~6m lava flow. The higher K/Ca samples gives a lower age than the Layer 'A' samples, whereas the lower K/Ca samples give higher age than expected. Therefore, these ages were removed from the reported age population (see text for further discussion).

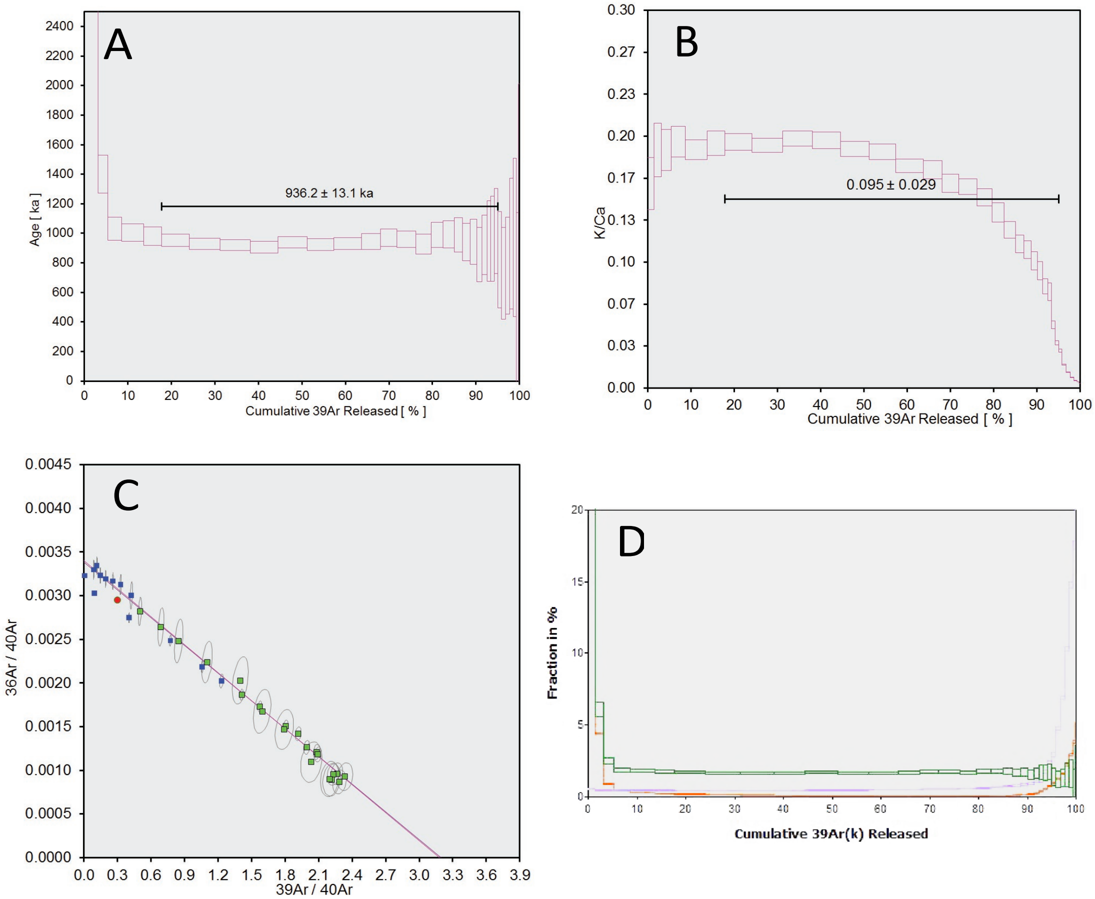

Figure A.8: Argon analysis of a 15mg split of sample 5 from 'layer B' (intermediate vesicular portion) of the flow. The weighted plateau age was not used in the reported weighted mean age for this flow. (**A**) The incremental heating plateau with age uncertainties reported at the 2σ confidence level. Early heating steps are excluded as they represent discordant incremental heating steps and are likely reflecting ^{39}Ar(K) recoil through the preferential degassing of fine-grained secondary (e.g. clay) phases that remain resident in the groundmass separates, even after the applied intense acid leaching protocol, but are resolved at higher temperatures and within the age plateau at the 2σ confidence interval. High temperature heating steps are also excluded due to high temperature ^{37}Ar(Ca) and ^{39}Ar(K) recoil. (**B**) The K/Ca curve for the incremental heating experiment. (**C**) The inverse isochron, whereby green squares represent points within the selected plateau and blue squares are excluded points from the heating plateau. The red circle represents the total fusion value. (**D**) Degassing patterns for the incremental heating experiment, normalized against the size of the gas released in each incremental heating step. The green boxes represent radiogenic ^{40}Ar*, the orange represent the atmospheric component (^{36}Ar) and purple is the Ca proxy (^{37}Ar). The concentration of Ca increases toward the higher temperatures by the preferential degassing of plagioclase and clinopyroxene micro-crystals in the groundmass (also reflected in the decreasing K/Ca ratio). The atmospheric signature shows high fraction percent during the low temperature heating steps, likely due to alteration. In the higher heating steps this atmospheric signature also increases, likely due to the presence of trapped atmospheric components during the formation of the lava flow. Layer 'B' samples have weighted plateau ages that are not reproducible at the 2σ uncertainty level and which have highly variable K/Ca signatures indicating heterogeneity within the upper part of the ~6m lava flow. The higher K/Ca samples gives a lower age than the Layer 'A' samples, whereas the lower K/Ca samples give higher age than expected. Therefore, these ages were removed from the reported age population (see text for further discussion).

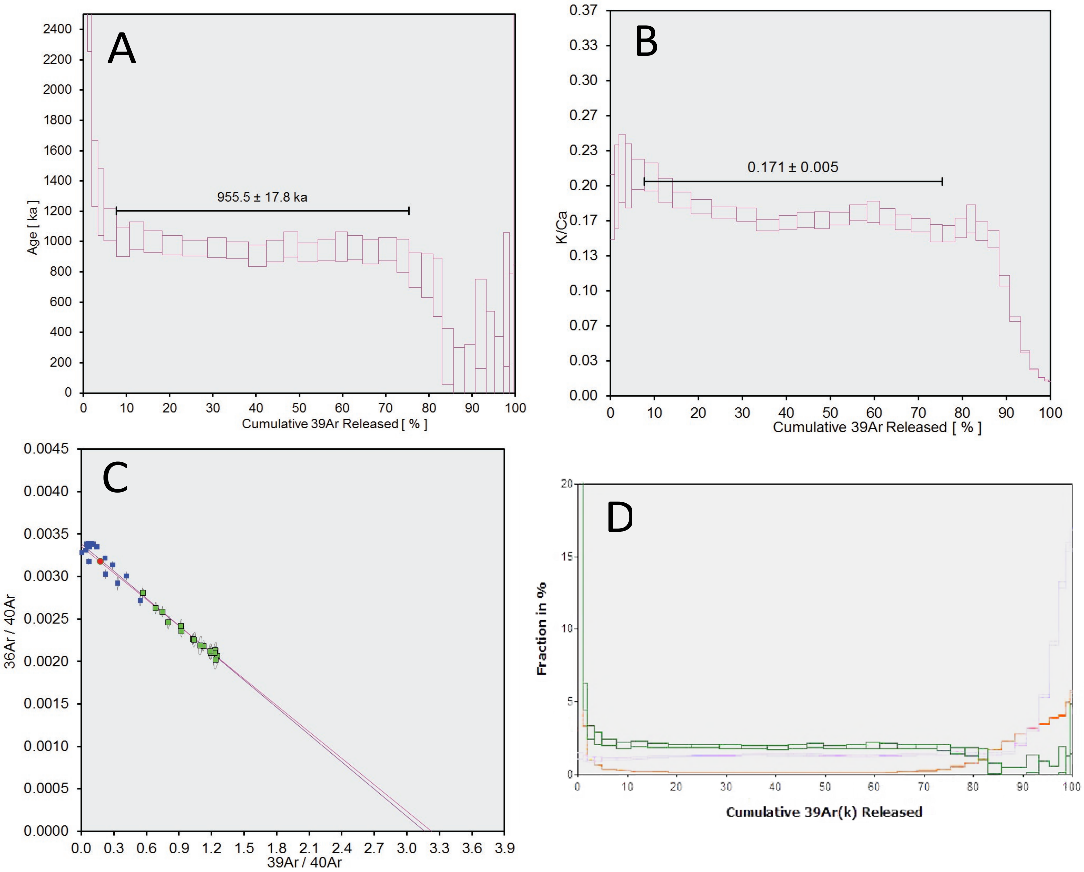

Figure A.9: Argon analysis of a 15mg split of sample 2 from 'layer C' (altered frothy topmost portion) of the flow. The weighted plateau age was not used in the reported weighted mean age for this flow. (**A**) The incremental heating plateau with age uncertainties reported at the 2σ confidence level. Early heating steps are excluded as they represent discordant incremental heating steps and are likely reflecting ^{39}Ar(K) recoil through the preferential degassing of fine-grained secondary (e.g. clay) phases that remain resident in the groundmass separates, even after the applied intense acid leaching protocol, but are resolved at higher temperatures and within the age plateau at the 2σ confidence interval. High temperature heating steps are also excluded due to high temperature ^{37}Ar(Ca) and ^{39}Ar(K) recoil. (**B**) The K/Ca curve for the incremental heating experiment. (**C**) The inverse isochron, whereby green squares represent points within the selected plateau and blue squares are excluded points from the heating plateau. The red circle represents the total fusion value. (**D**) Degassing patterns for the incremental heating experiment, normalized against the size of the gas released in each incremental heating step. The green boxes represent radiogenic ^{40}Ar*, the orange represent the atmospheric component (^{36}Ar) and purple is the Ca proxy (^{37}Ar). The concentration of Ca increases toward the higher temperatures by the preferential degassing of plagioclase and clinopyroxene micro-crystals in the groundmass (also reflected in the decreasing K/Ca ratio). The atmospheric signature shows high fraction percent during the low temperature heating steps, likely due to alteration. In the higher heating steps this atmospheric signature also increases, likely due to the presence of trapped atmospheric components during the formation of the lava flow. The two samples from Layer 'C' were not included in the reported age population for lava flow due to increased scatter in the K/Ca and an average K/Ca that is lower than Layer 'A' samples. The glassy nature of the Layer 'B' and 'C' samples may enhance the overall recoil and the presence of minor excess argon in these samples, resulting in older apparent ages.

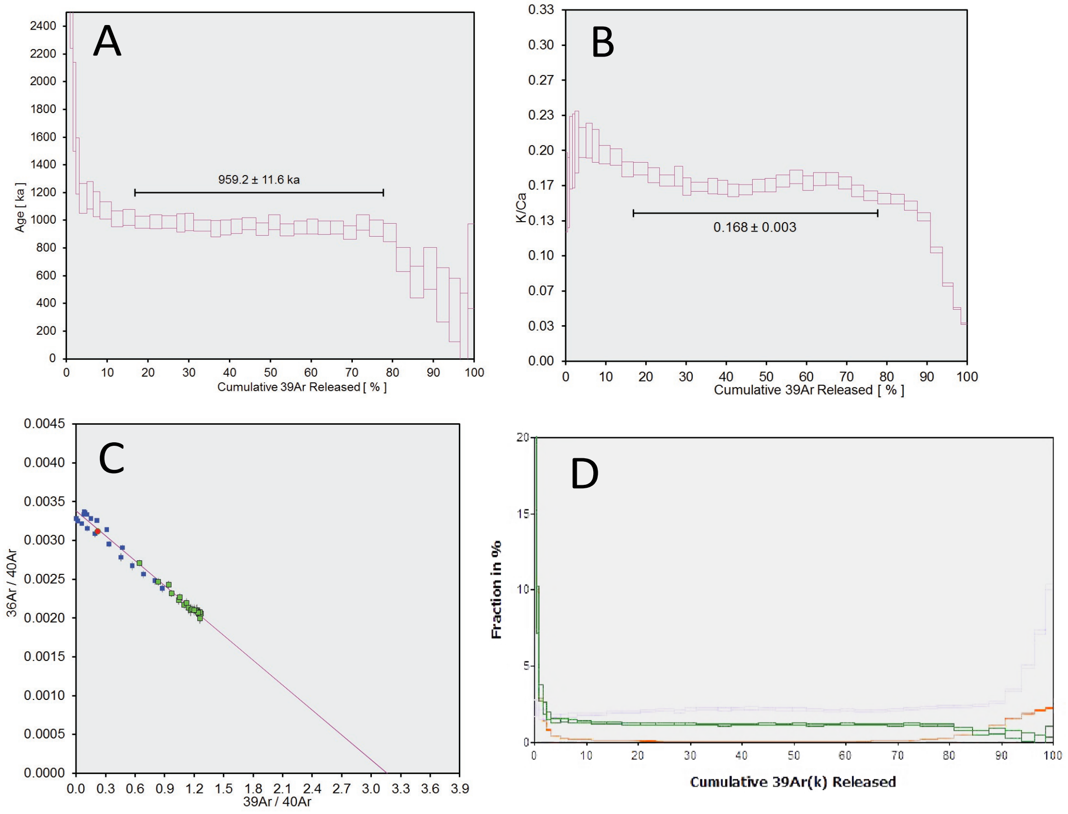

Figure A.10: Argon analysis of a 25mg split of sample 2 from ‘layer C’ (altered frothy topmost portion) of the flow. The weighted plateau age was not used in the reported weighted mean age for this flow. (**A**) The incremental heating plateau with age uncertainties reported at the 2σ confidence level. Early heating steps are excluded as they represent discordant incremental heating steps and are likely reflecting ^{39}Ar(K) recoil through the preferential degassing of fine-grained secondary (e.g. clay) phases that remain resident in the groundmass separates, even after the applied intense acid leaching protocol, but are resolved at higher temperatures and within the age plateau at the 2σ confidence interval. High temperature heating steps are also excluded due to high temperature ^{37}Ar(Ca) and ^{39}Ar(K) recoil. (**B**) The K/Ca curve for the incremental heating experiment. (**C**) The inverse isochron, whereby green squares represent points within the selected plateau and blue squares are excluded points from the heating plateau. The red circle represents the total fusion value. (**D**) Degassing patterns for the incremental heating experiment, normalized against the size of the gas released in each incremental heating step. The green boxes represent radiogenic ^{40}Ar*, the orange represent the atmospheric component (^{36}Ar) and purple is the Ca proxy (^{37}Ar). The concentration of Ca increases toward the higher temperatures by the preferential degassing of plagioclase and clinopyroxene micro-crystals in the groundmass (also reflected in the decreasing K/Ca ratio). The atmospheric signature shows high fraction percent during the low temperature heating steps, likely due to alteration. In the higher heating steps this atmospheric signature also increases, likely due to the presence of trapped atmospheric components during the formation of the lava flow. The two samples from Layer 'C' were not included in the reported age population for lava flow due to increased scatter in the K/Ca and an average K/Ca that is lower than Layer 'A' samples. The glassy nature of the Layer 'B' and 'C' samples may enhance the overall recoil and the presence of minor excess argon in these samples, resulting in older apparent ages.

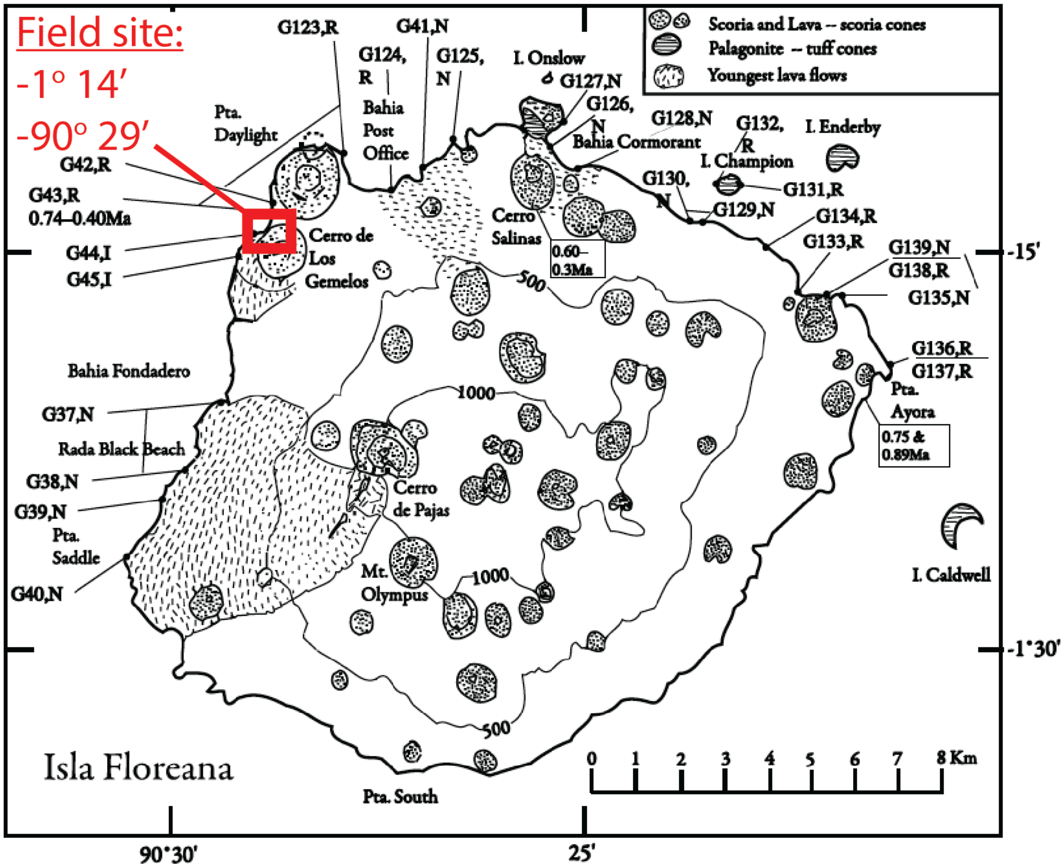

Figure A.11: A map of Floreana Island, Galapagos altered from Gromme et al., (2010). The sampled lava flow is outlined in red.

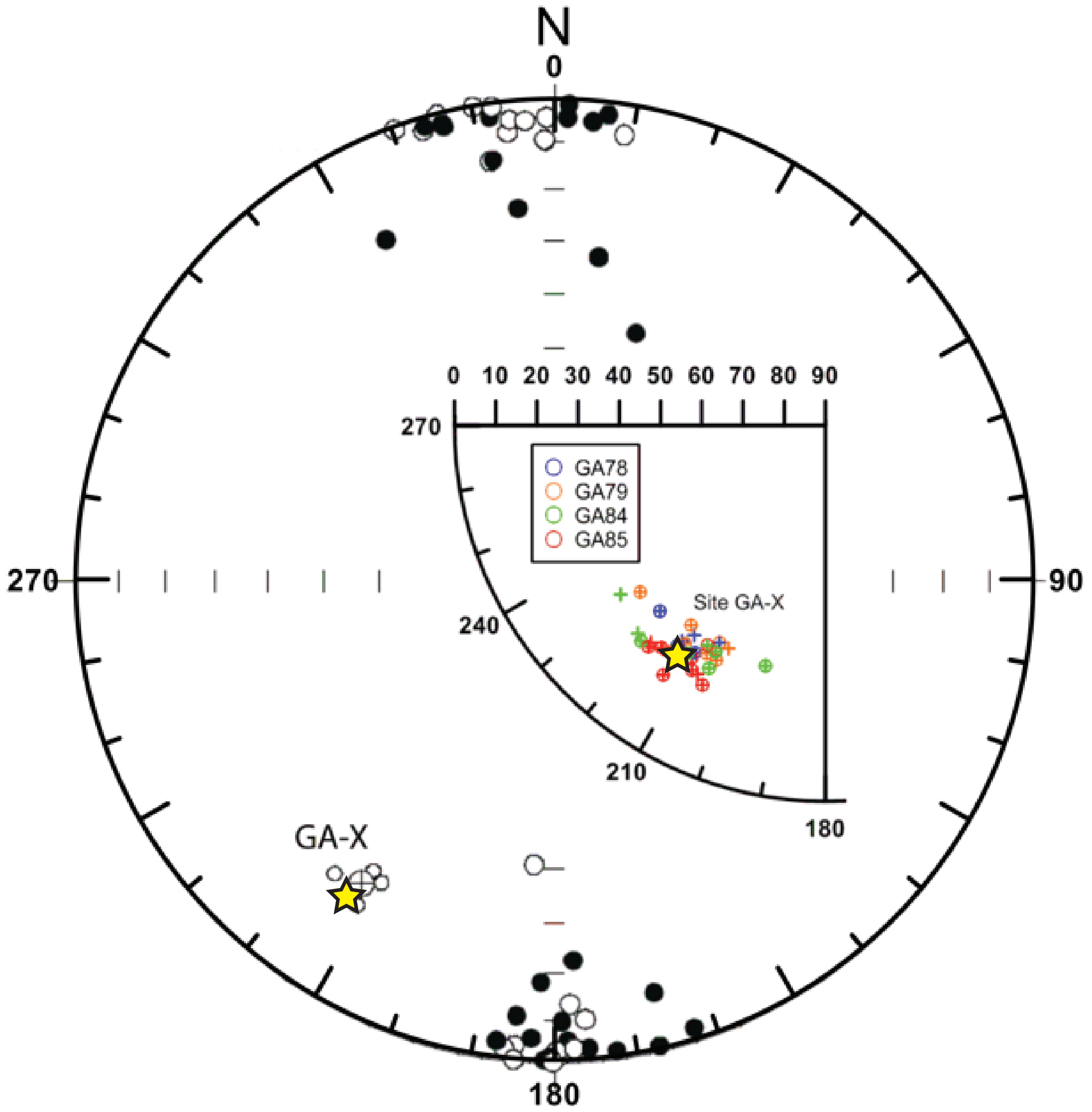

Figure A.12: The mean paleomagnetic direction for samples in this study shown by gold stars (Inc = -30.5°, Dec = 215.7°; n=42; A95=4.8°) superimposed on figure 2 from Wang and Kent (2013) in order to verify that we sampled the same flow for ^{40}Ar/^{39}Ar geochronological analyses. Filled and opened circles represent site-mean paleomagnetic directions for all Galapagos sample sites reported in Kent et al., (2010). The 180-270° quadrantal inset with colored symbols represent the individual measurements for the lava flows that make up the GA-X site.

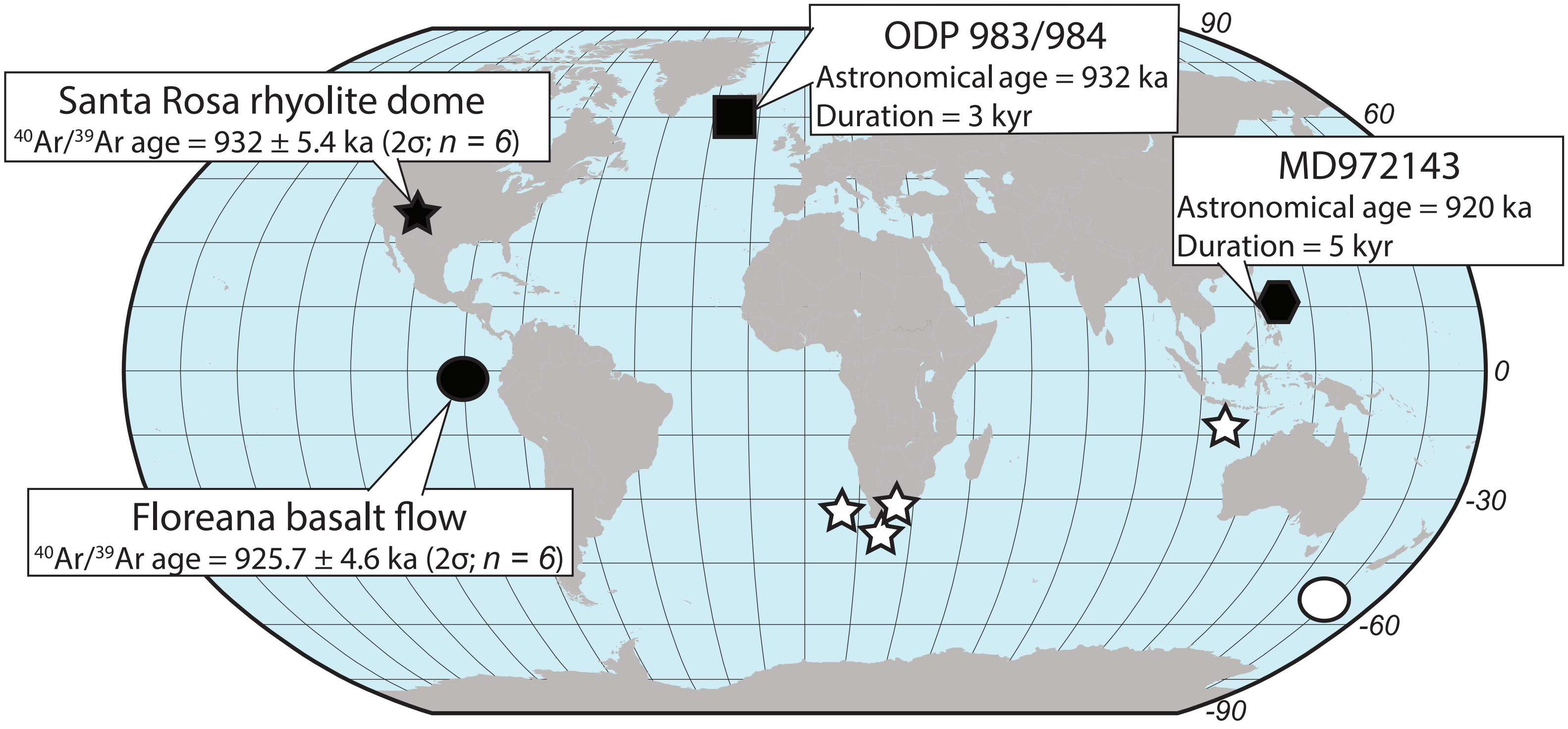
Santa Rosa rhyolite dome
^{40}Ar/^{39}Ar age = 932 ± 5.4 ka (2σ; n = 6)
ODP 983/984
Astronomical age = 932 ka
Duration = 3 kyr
MD972143
Astronomical age = 920 ka
Duration = 5 kyr
Floreana basalt flow
^{40}Ar/^{39}Ar age = 925.7 ± 4.6 ka (2σ; n = 6)
90
60
0
-30
-60
-90

Figure A.13: A Robinson projection of the globe with site locations recording the Santa Rosa Excursion (darker colors) and corresponding VGP for lava flows (lighter colors). Ages are reported in thousands of years before present and errors are reported as 2σ. Data from Floreana Island, Galapagos (circle) from Wang and Kent (2013) and this study. The Santa Rosa Dome, New Mexico, sanidine ages (star) from data in Doell et al. (1968), Singer and Brown (2002), and Singer (2014). ODP Sites 983 and 984 (rectangle) are reported in Channell et al. (2002). Sediment core MD972143 (polygon) data is from Horng et al. (2002).

A.2 References

Channell, J., Mazaud, A., Sullivan, P., Turner, S., and Raymo, M., 2002, Geomagnetic excursions and paleointensities in the Matuyama Chron at Ocean Drilling Program sites 983 and 984 (Iceland Basin): Journal of Geophysical Research: Solid Earth, v. 107, p. 1–14.

Doell, R.R., Dalrymple, G.B., Smith, R.L., and Bailey, R.A., 1968, Paleomagnetism, potassium-argon ages, and geology of rhyolites and associated rocks of the Valles caldera, New Mexico: Geological Society of America, v. 116, p. 211–248, doi:10.1130/MEM116-p211.

Horng, C.-S., Lee, M.-Y., Palike, H., Wei, K.-Y., Liang, W.-T., Iizuka, Y., and Torii, M., 2002, Astronomically calibrated ages for geomagnetic reversals within the Matuyama chron: Earth, Planets, and Space, v. 54, p. 679–690, doi:10.1186/BF03351719.

Koppers, A.A., 2002, ArArCALC—software for 40Ar/39Ar age calculations: Computers & Geosciences, v. 28, p. 605–619, doi:10.1016/S0098-3004(01)00095-4.

Koppers, A.A.P., Duncan, R.A., and Steinberger, B., 2004, Implications of a nonlinear 40Ar/39Ar age progression along the Louisville seamount trail for models of fixed and moving hot spots: Geochemistry Geophysics Geosystems, v. 5, Q06L02, doi:10.1029/2003GC000671.

Singer, B., and Brown, L.L., 2002, The Santa Rosa Event: 40Ar/39Ar and paleomagnetic results from the Valles rhyolite near Jaramillo Creek, Jemez

Mountains, New Mexico: Earth and Planetary Science Letters, v. 197, p. 51–64, doi:10.1016/S0012-821X(01)00598-2.

Singer, B.S., 2014, A Quaternary geomagnetic instability time scale: Quaternary Geochronology, v. 21, p. 29–52, doi:10.1016/j.quageo.2013.10.003.

Wang, H., and Kent, D.V., 2013, A paleointensity technique for multidomain igneous rocks: Geochemistry Geophysics Geosystems, v. 14, p. 4195–4213, doi:10.1002/ggge.20248.

Appendix B – Millennial-Scale Instability in the Earth's Magnetic Field Prior to the Matuyama-Brunhes Reversal

B.1 Materials and methods

B.1.1: Field site description and sample description

Basaltic lava flows from the island of Tahiti-Nui, Society Islands were sampled in order to capture the dynamics of the Matuyama-Bruhnes reversal. We reoccupied the site sampled by Mochizuki et al. (2011). More than twenty-nine lava flows were exposed by road cuts during the development of a housing project on the northern side of the Punaruu valley in the early 1990's. These lava flows can be related to the Chauvin et al. (1990) samples collected from the southern side of the valley. The lava flows consisted primarily of clinopyroxene and olivine phyric alkali basalts (including some ankaramites) that have erupted as typically massive flows ranging from 2 to 10 m in height. Distinct rubbly tops on each flow separate individual flows from each other.

At least six samples were selected for ^{40}Ar/^{39}Ar analyses from each lava flow. We preferentially sampled basalt with a holocrystalline groundmass character from the freshest sections of each flow. Every effort was made to increase the horizontal spacing between samples. The average horizontal distance between samples was ~3-4 meters. Oriented paleomagnetic cores were drilled for each lava flow to confirm sampling of the same lava flows detailed by Mochizuki et al. (2011) (see Figure 3.1).

B.1.2: Sample preparations and acid-leaching for ^{40}Ar/^{39}Ar geochronology

Between two and six incremental heating analyses per flow were undertaken using the ^{40}Ar/^{39}Ar age dating method. Samples were crushed and sieved to a grain size of 150-180 µm followed by removal of pyroxene and olivine by magnetic separation. Moderately magnetic groundmass separates were then acid leached following previously defined procedures (Koppers et al., 2011; Balbas et al., 2016). Samples were sonicated for four one-hour steps in 3N and 6N HCl and 1N and 3N HNO3 followed by a one-hour sonication in ultrapure H2O (Koppers et al., 2000; 2011). Samples were then oven dried overnight at 50^{o}C. All samples were handpicked under a binocular microscope to avoid any alteration and the presence of adhering phenocryst fragments. Samples were loaded into aluminum packets and irradiated in the Oregon State University (OSU) TRIGA reactor for six hours with Fish Canyon Tuff (FCT) sanidine flux monitors along with Alder Creek (AC-2) sanidine samples used as a secondary standard.

B.1.3: ^{40}Ar/^{39}Ar geochronology mass spectrometry and data reduction

Samples were analyzed using a Thermo Scientific ARGUS VI mass spectrometer in the OSU Argon Geochronology Laboratory (http://geochronology.coas.oregonstate.edu). Approximately 19 mg of groundmass sample was loaded into copper trays. Samples were incrementally heated using a CO_2 laser for 33 steps with blanks run before, after, and during the analyses (a total of 14 blanks). Released gas was exposed to and cleaned for 6 minutes using four getters kept at respectively 400°C (ST101), 200°C (ST172) and room temperate (ST172, AP10). Samples were inlet into the mass spectrometer with ^{40}Ar, ^{39}Ar, ^{38}Ar, and ^{37}Ar measured simultaneously on five 10^{12} Ω faraday cups while the ^{36}Ar was measured on an ion-counting CuBe electron multiplier.

All ages were processed using ArArCALC v.2.7.0 (Koppers, 2002) with a Fish Canyon Tuff (FCT) sanidine as a fluence monitor with as assigned age of 28.201 ± 0.046 Ma (2σ; Kuiper et al., 2008) and the decay constant and equations of Min et al. (2000). All errors include corrections for baselines, blanks, irradiation, production ratios, radioactive decay, mass fractionation, and the multiplier/Faraday collector calibration on mass 36. Reproducibility of the secondary AC-2 sanidine standard has been excellent providing an age of 1185.2 ± 3.8 ka; MSWD: 6.62; N = 257/275 using the FCT standard age of 28.201 Ma, within error with the AC-2 age of 1186.4 ± 3.0 ka from Jicha et al. (2016) measured on a Noblesse Nu-instruments multicollector mass spectrometer.

B.1.4 Sample Exclusions

Whenever possible we used the same sample identifications for flows as Mochizuki et al (2011). While in the field, we observed portions of flows or potential previously unreported new flows and/or contacts. The stratigraphic relationship and geologic context of these flows could not be resolved in the field due to obstruction by road cuts and general construction. Several homes cover the area and roads were constructed along the weaker, highly-altered and fractured sections of basalt. Consequently, some road cuts are covered in cement to prevent rock fall. Again, we note that these features were not sampled by Mochizuki et al (2011). However, we endeavored to collected samples of these features that were all highly weathered and altered in hopes of resolving their geologic significance with paleomagnetic and/or ^{40}Ar/^{39}Ar analyses. Unfortunately, the paleomagnetic measurements of these samples were not helpful for resolving their field relationships because too few samples were collected coupled with the fact that we had no previous data to compare against. The ^{40}Ar/^{39}Ar analyses could not help us resolve the geologic significance of these flows either due to the large scatter between ages on a single flow feature likely due to the extremely altered character of these samples. Thus, we must exclude the samples from flows B0, B0*, A28a, and A28a*. Please note that such sample names are not reported in Mochizuki et al (2011).

Sample B3-Ar-3 was excluded from the mean flow age calculation of B3 due to the presence of excess Ar evident in the heating spectrum and non-atmospheric isochron intercept. Accordingly, of the 57 incremental heating experiments conducted for this project, we report 46 with the only exclusions listed above.

B.2: Current precision and accuracy of ^{40}Ar/^{39}Ar geochronology

The accuracy and precision of the ^{40}Ar/^{39}Ar method are well documented by recent studies regarding the timing of the Laschamp and Santa Rosa excursions. North American speleothems were used to define the age of the Laschamp Excursion as 41.10 ± 0.35 ka using high precision ^{230}Th dating and layer counting (Lascu et al. 2016). The most recent age determinations for this excursion using ^{40}Ar/^{39}Ar geochronology are in good agreement at 41.30 ± 0.60 ka and 40.70 ± 0.95 ka (Laj et al. 2014; Singer et al. 2009). These ages are also in good agreement with sediment archives, for example the PISO1500 stack (Channel 2009) in which the paleointensity low associated with the Laschamp Excursion appears at ~40 ka. Recent ^{40}Ar/^{39}Ar age determinations for lavas from Floreana Island (Galapagos) similarly are in excellent agreement with astrochonologically-tuned sediment records. In Floreana the Santa Rosa excursion was ^{40}Ar/^{39}Ar dated at 925.7 ± 4.6 ka and shown to record an absolute paleointensity equaling no more than 14% of today's magnetic field strength (Wang and Kent, 2005; Balbas et al. 2016). This short-lived geomagnetic event is again in close agreement with the PISO1500 stack that provides an age of 926 ka for the same sharp field strength reduction (Balbas et al. 2016) by astrochronological tuning (Channel et al. 2002). The agreement between these two geochronological methodologies illustrates that both can provide precise and accurate timing estimates for the same, short-lived geomagnetic events. This implies that over the timescale of the last million years, assumptions in both methods seem to be reasonable and accurate. The FCT sanidine standard age of 28.201 ± 0.046 (2σ) Ma of Kuiper et al.

(2008) and the adjusted decay constants of Min et al. (2000) seem to provide the correct $^{40}Ar/^{39}Ar$ ages for lava flows (at least) younger than 1 Ma and relative to astrononologically-tuned marine sediments.

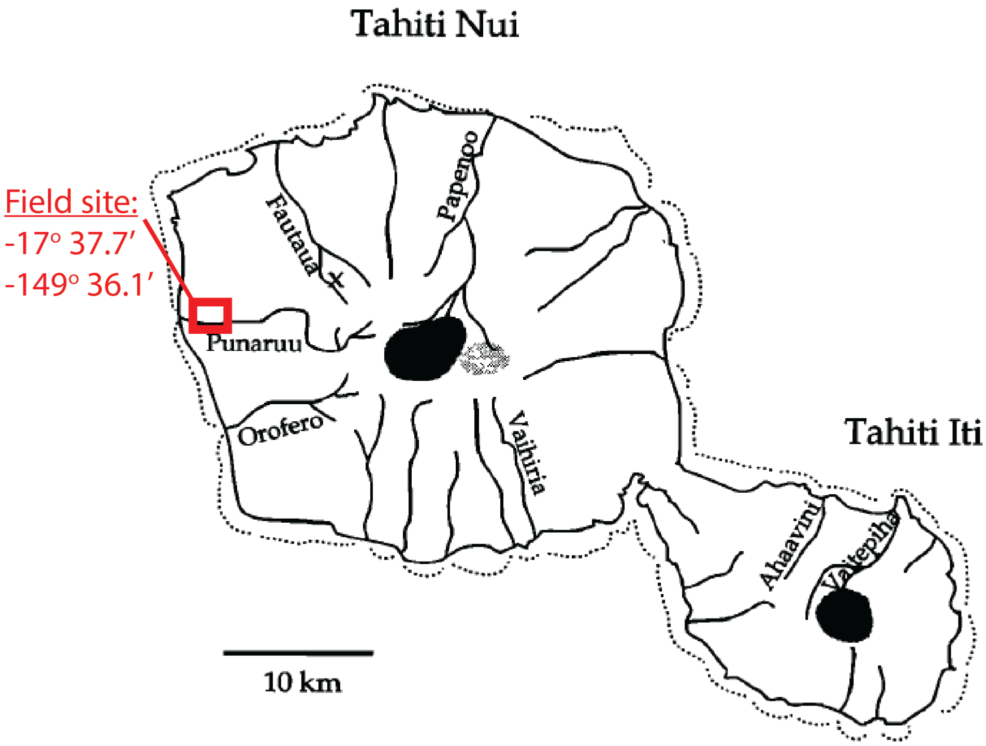

Figure B.1: A map of Tahiti, Society Islands altered from Duncan et al., (1994). The location of the sampled lava flows is outlined in red.

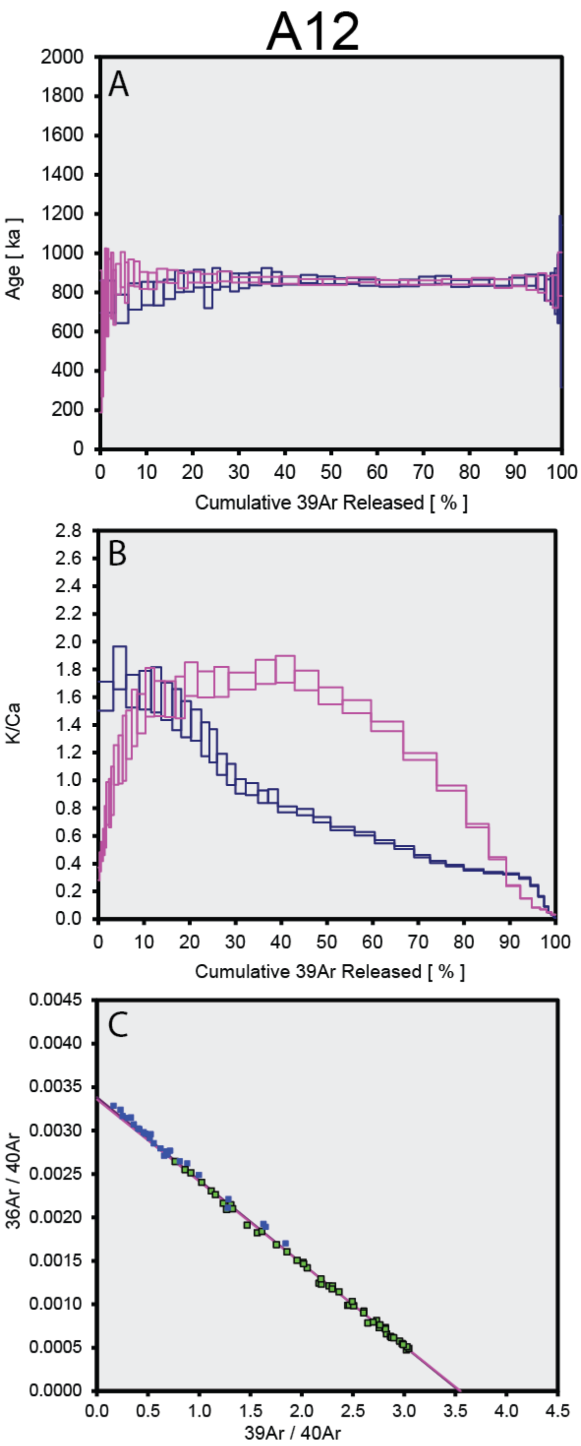

Figure B.2: The argon analysis of lava flow A12 (n=2). **(A)** The incremental heating plateau with age uncertainties reported at the 2σ confidence level. Early heating steps are excluded as they represent discordant incremental heating steps and are likely reflecting some partial loss of radiogenic ^{40}Ar through partial degassing. The spectrum becomes flat and concordant within the age plateau at the 2σ confidence interval. **(B)** The K/Ca curve for the incremental heating experiment, showing the petrologic and chemical K/Ca differences between these two samples from a single flow. The two samples show concordant ages with different K/Ca curves. Sample A12-Ar-4 (blue) K/Ca indicates an increased glassy component that degasses a ^{39}Ar(K) component at lower temperatures. **(C)** The inverse isochron, whereby green squares represent points within the selected plateau and blue squares are excluded points from the heating plateau.

Table B.1: (Below) Incremental heating plateau results for flow A12.

Sample	**Age (ka)**	**2σ**	**MSWD**	**40Ar/36Ar int**	**2σ**
A12-Ar-2	858.7	4.3	0.95	303.9	6.8
A12-Ar-4	855.7	4.9	0.65	298.2	2.5

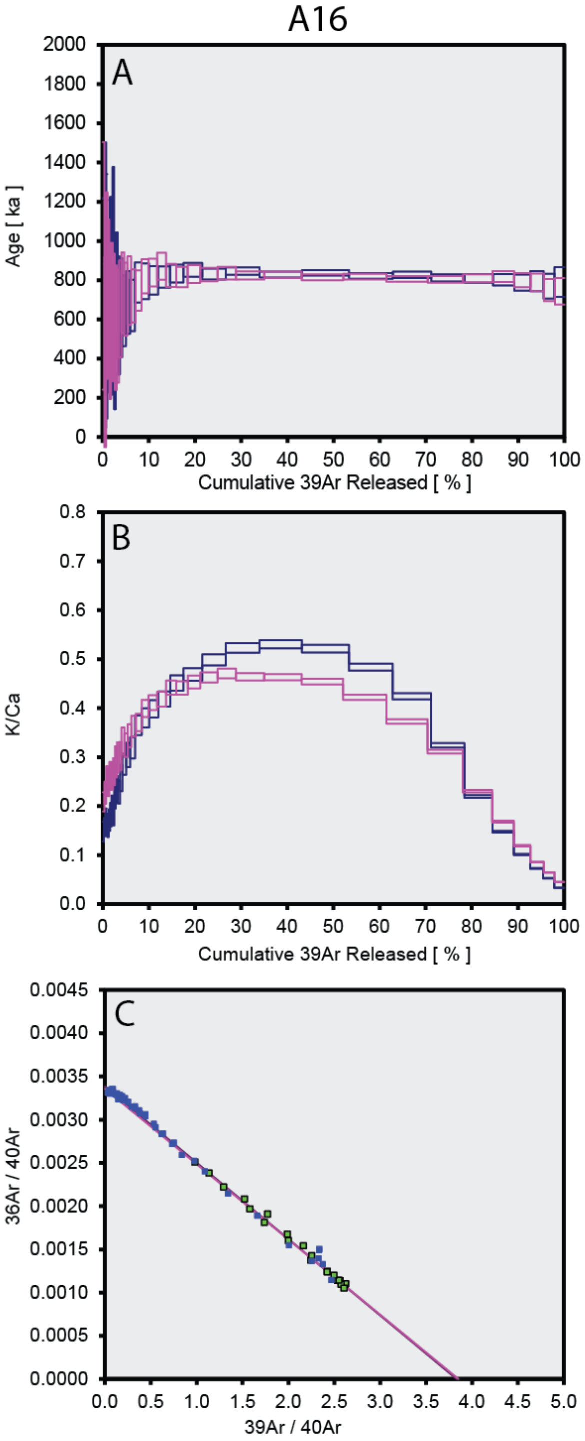

Figure B.3: The argon analysis of lava flow A16 (n=2). **(A)** The incremental heating plateau with age uncertainties reported at the 2σ confidence level. Early heating steps are excluded as they represent discordant incremental heating steps and are likely reflecting some partial loss of radiogenic ^{40}Ar through partial degassing. The spectrum becomes flat and concordant within the age plateau at the 2σ confidence interval. The highest temperature heating steps are excluded from the age calculation due to high temperature ^{37}Ar(Ca) and ^{39}Ar(K) recoil. **(B)** The K/Ca curve for the incremental heating experiment. Samples display a saddled pattern indicating early degassing of some alteration components the ^{39}Ar(K) increases as the interstitial mesostatsis degasses. The ^{37}Ar(Ca) component increase towards the higher temperature steps as plagioclase and clinopyroxene components begin degassing. **(C)** The inverse isochron, whereby green squares represent points within the selected plateau and blue squares are excluded points from the heating plateau.

Table B.2: (Below) Incremental heating plateau results for flow A16.

Sample	**Age (ka)**	**2σ**	**MSWD**	**40Ar/36Ar int**	**2σ**
A16-Ar-2	816.5	6	0.8	299.9	5.4
A16-Ar-4	815.4	8.6	1.14	275.3	16

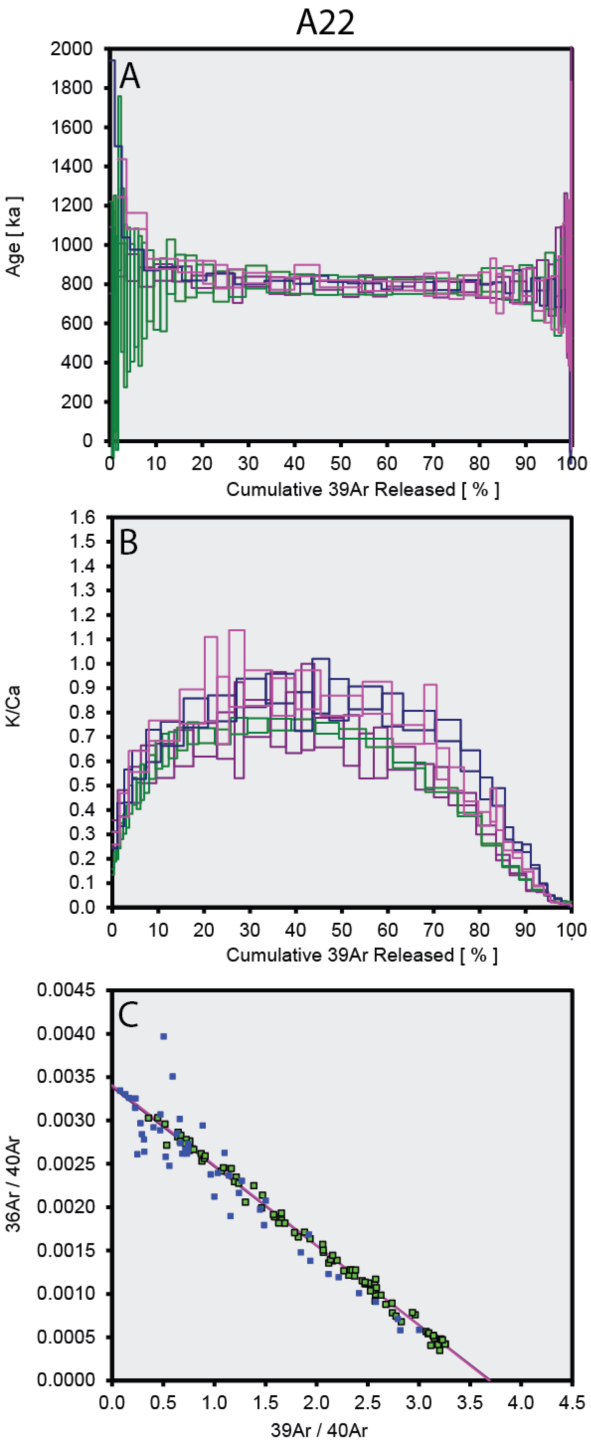

Figure B.4: The argon analysis of lava flow A22 (n=4). **(A)** The incremental heating plateau with age uncertainties reported at the 2σ confidence level. Early heating steps are excluded as they represent discordant incremental heating steps and are likely reflecting ^{39}Ar(K) recoil through the preferential degassing of fine-grained secondary (e.g. clay) phases that remain resident in the groundmass separates, even after the applied intense acid leaching protocol, but are resolved at higher temperatures and within the age plateau at the 2σ confidence interval. High temperature heating steps are also excluded due to high temperature ^{37}Ar(Ca) and ^{39}Ar(K) recoil. **(B)** The K/Ca curve for the incremental heating experiment. Samples display a saddled pattern indicating early degassing of some alteration components the ^{39}Ar(K) increases as the interstitial mesostatsis degasses. The ^{37}Ar(Ca) component increase towards the higher temperature steps as plagioclase and clinopyroxene components begin degassing. **(C)** The inverse isochron, whereby green squares represent points within the selected plateau and blue squares are excluded points from the heating plateau.

Table B.3: (Below) Incremental heating plateau results for flow A22.

Sample	Age (ka)	2σ	MSWD	40Ar/36Ar int	2σ
A22-Ar-2	800.7	9.1	0.85	290.3	9.3
A22-Ar-3	801	8.6	1.99	316.7	42.3
A22-Ar-4a	799	13.1	0.34	293.8	5.1
A22-Ar-4b	795.7	8.3	0.86	293.3	5.2

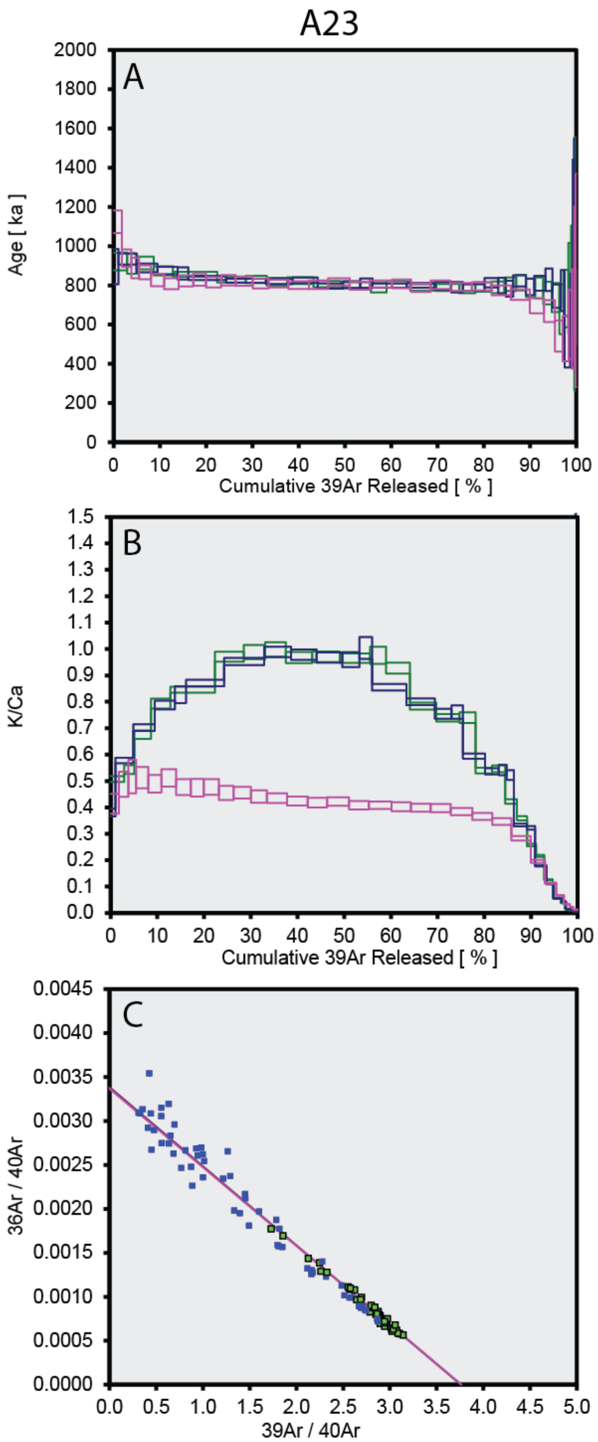

Figure B.5: The argon analysis of lava flow A23 (n=3). **(A)** The incremental heating plateau with age uncertainties reported at the 2σ confidence level. Early heating steps are excluded as they represent discordant incremental heating steps and are likely reflecting ^{39}Ar(K) recoil through the preferential degassing of fine-grained secondary (e.g. clay) phases that remain resident in the groundmass separates, even after the applied intense acid leaching protocol, but are resolved at higher temperatures and within the age plateau at the 2σ confidence interval. High temperature heating steps are also excluded due to high temperature ^{37}Ar(Ca) and ^{39}Ar(K) recoil. **(B)** The K/Ca curve for the incremental heating experiment, showing the petrologic and chemical K/Ca differences between these two samples from a single flow. The two samples show concordant ages with different K/Ca curves. Sample A23-Ar-1 (pink) K/Ca indicates an increased glassy component that degasses a ^{39}Ar(K) component at lower temperatures. Samples A23-Ar-3 and 4 display a saddled pattern indicating early degassing of some alteration components the ^{39}Ar(K) increases as the interstitial mesostatsis degasses. The ^{37}Ar(Ca) component increase towards the higher temperature steps as plagioclase and clinopyroxene components begin degassing. **(C)** The inverse isochron, whereby green squares represent points within the selected plateau and blue squares are excluded points from the heating plateau.

Table B.4: (Below) Incremental heating plateau results for flow A23.

Sample	Age (ka)	2σ	MSWD	40Ar/36Ar int	2σ
A23-Ar-1	805.4	5.7	0.97	287.3	29.3
A23-Ar-3	799.7	5.4	0.68	304.2	13.6
A23-Ar-4	797.1	6.3	0.77	299.5	23.8

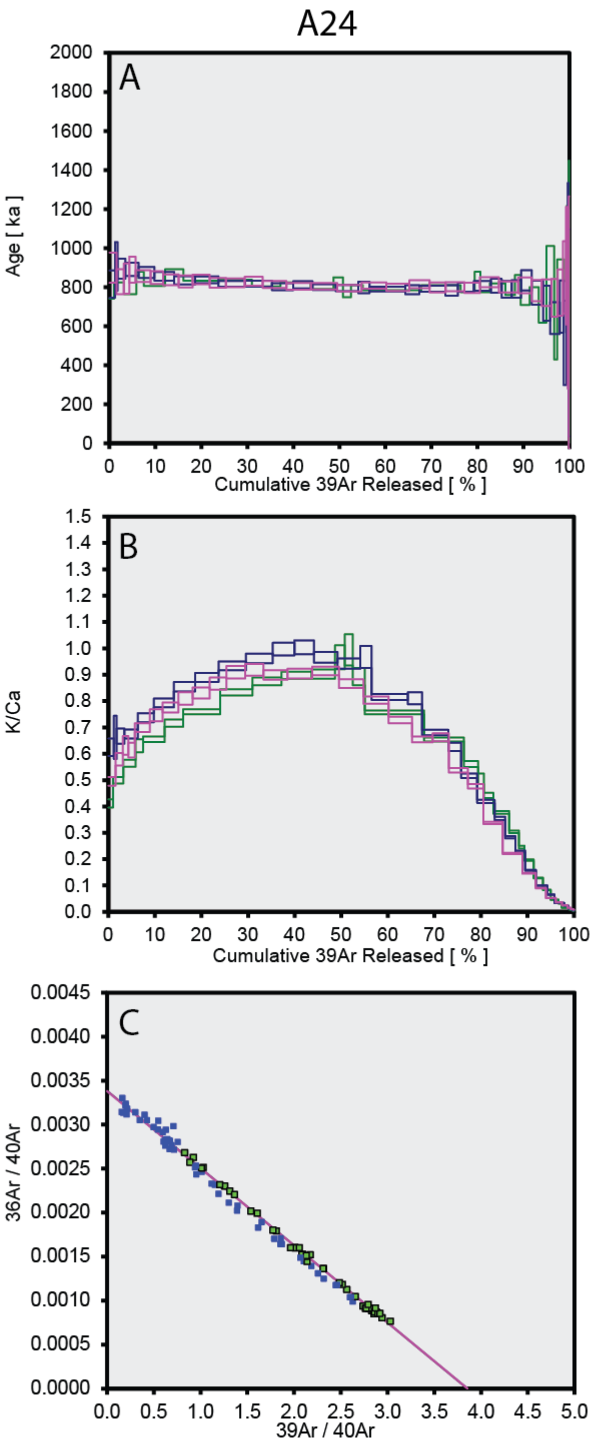

Figure B.6: The argon analysis of lava flow A24 (n=3). **(A)** The incremental heating plateau with age uncertainties reported at the 2σ confidence level. Early heating steps are excluded as they represent discordant incremental heating steps and are likely reflecting ^{39}Ar(K) recoil through the preferential degassing of fine-grained secondary (e.g. clay) phases that remain resident in the groundmass separates, even after the applied intense acid leaching protocol, but are resolved at higher temperatures and within the age plateau at the 2σ confidence interval. High temperature heating steps are also excluded due to high temperature ^{37}Ar(Ca) and ^{39}Ar(K) recoil. **(B)** The K/Ca curve for the incremental heating experiment. Samples display a saddled pattern indicating early degassing of some alteration components the ^{39}Ar(K) increases as the interstitial mesostatsis degasses. The ^{37}Ar(Ca) component increase towards the higher temperature steps as plagioclase and clinopyroxene components begin degassing. **(C)** The inverse isochron, whereby green squares represent points within the selected plateau and blue squares are excluded points from the heating plateau.

Table B.5: (Below) Incremental heating plateau results for flow A24.

Sample	Age (ka)	2σ	MSWD	40Ar/36Ar int	2σ
A24-Ar-1	804.6	5.9	0.68	292.5	5.1
A24-Ar-2	797	5.5	0.73	299	5.1
A24-Ar-3	798.8	6	0.66	296.6	6.6

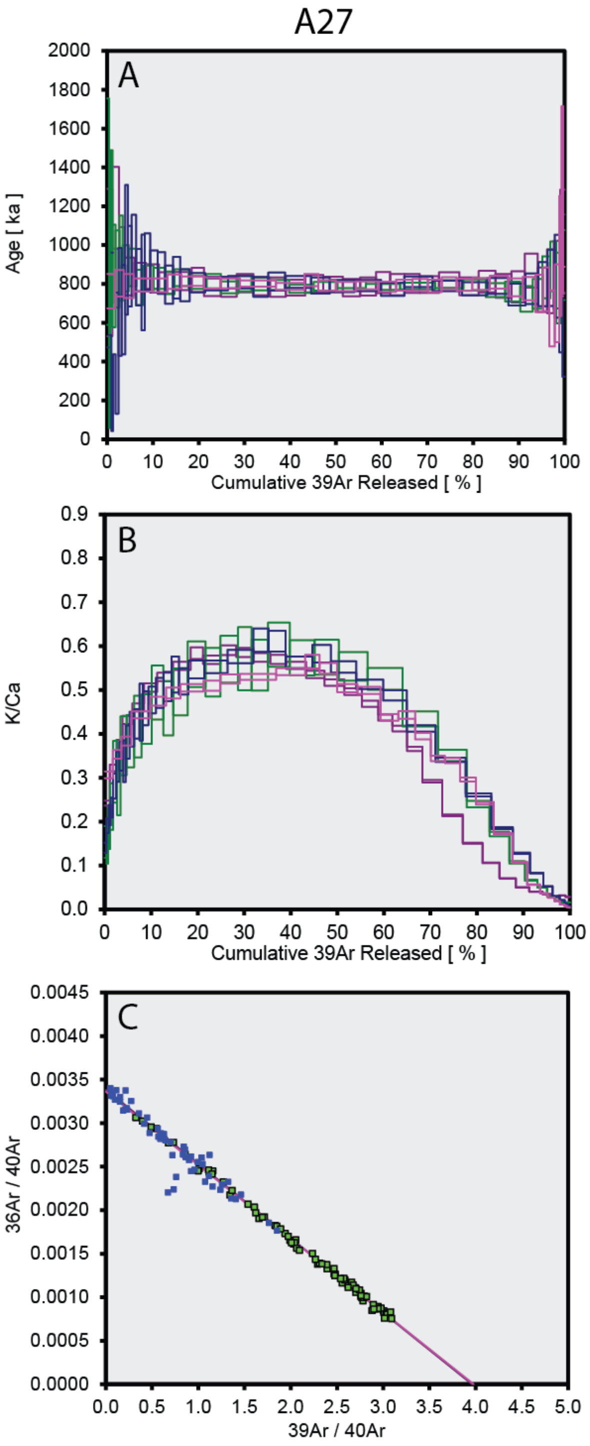

Figure B.7: The argon analysis of lava flow A27 (n=4). **(A)** The incremental heating plateau with age uncertainties reported at the 2σ confidence level. The plateau is flat for most analyses with some slight low temperature recoil effects seen within some spectrums. **(B)** The K/Ca curve for the incremental heating experiment. Samples display a saddled pattern indicating early degassing of some alteration components the ^{39}Ar(K) increases as the interstitial mesostatsis degasses. The ^{37}Ar(Ca) component increase towards the higher temperature steps as plagioclase and clinopyroxene components begin degassing. **(C)** The inverse isochron, whereby green squares represent points within the selected plateau and blue squares are excluded points from the heating plateau.

Table B.6: (Below) Incremental heating plateau results for flow A27.

Sample	Age (ka)	2σ	MSWD	40Ar/36Ar int	2σ
A27-Ar-1	796.9	6	0.48	294.6	3.6
A27-Ar-3a	795.8	9.2	0.52	297.2	12.9
A27-Ar-3b	790.1	6.9	0.49	300	14.2
A27-Ar-4	800	10	0.5	299	3.4

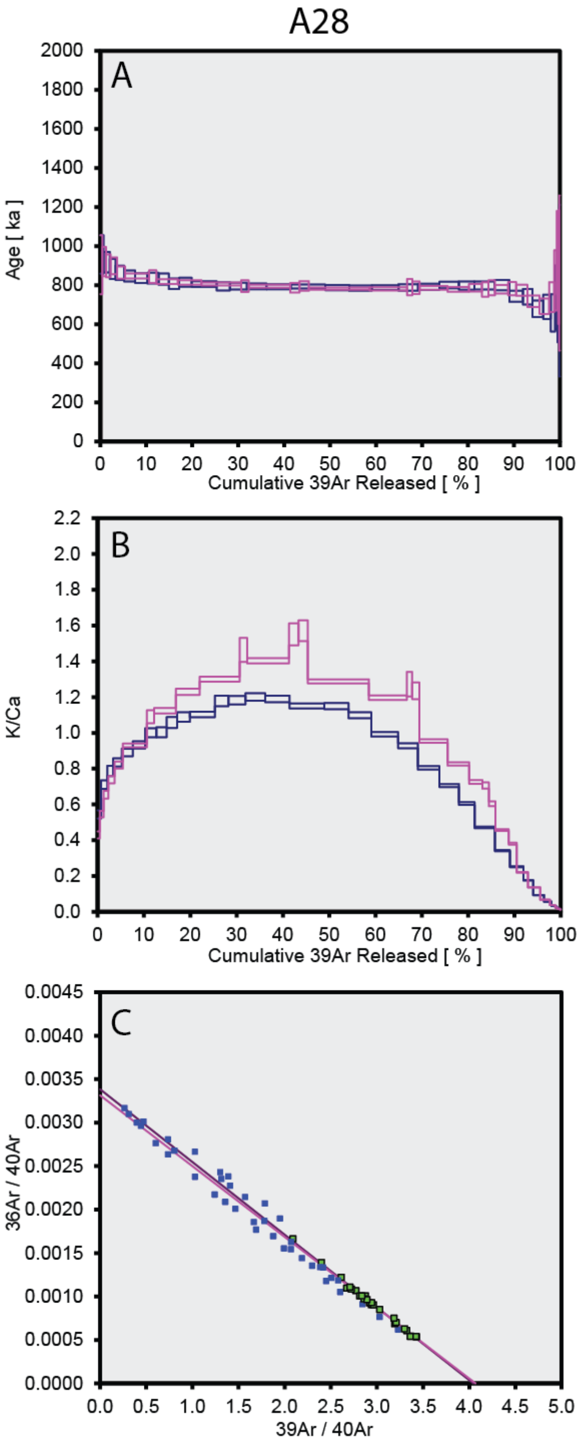

Figure B.8: The argon analysis of lava flow A28 (n=2). **(A)** The incremental heating plateau with age uncertainties reported at the 2σ confidence level. Early heating steps are excluded as they represent discordant incremental heating steps and are likely reflecting ^{39}Ar(K) recoil through the preferential degassing of fine-grained secondary (e.g. clay) phases that remain resident in the groundmass separates, even after the applied intense acid leaching protocol, but are resolved at higher temperatures and within the age plateau at the 2σ confidence interval. High temperature heating steps are also excluded due to high temperature ^{37}Ar(Ca) and ^{39}Ar(K) recoil. **(B)** The K/Ca curve for the incremental heating experiment. Samples display a saddled pattern indicating early degassing of some alteration components the ^{39}Ar(K) increases as the interstitial mesostatsis degasses. The ^{37}Ar(Ca) component increase towards the higher temperature steps as plagioclase and clinopyroxene components begin degassing. **(C)** The inverse isochron, whereby green squares represent points within the selected plateau and blue squares are excluded points from the heating plateau.

Table B.7: (Below) Incremental heating plateau results for flow A28.

Sample	Age (ka)	2σ	MSWD	40Ar/36Ar int	2σ
A28-Ar-1	785	3.5	0.81	292.4	10.3
A28-Ar-3	792	4.5	0.58	324.2	39.3

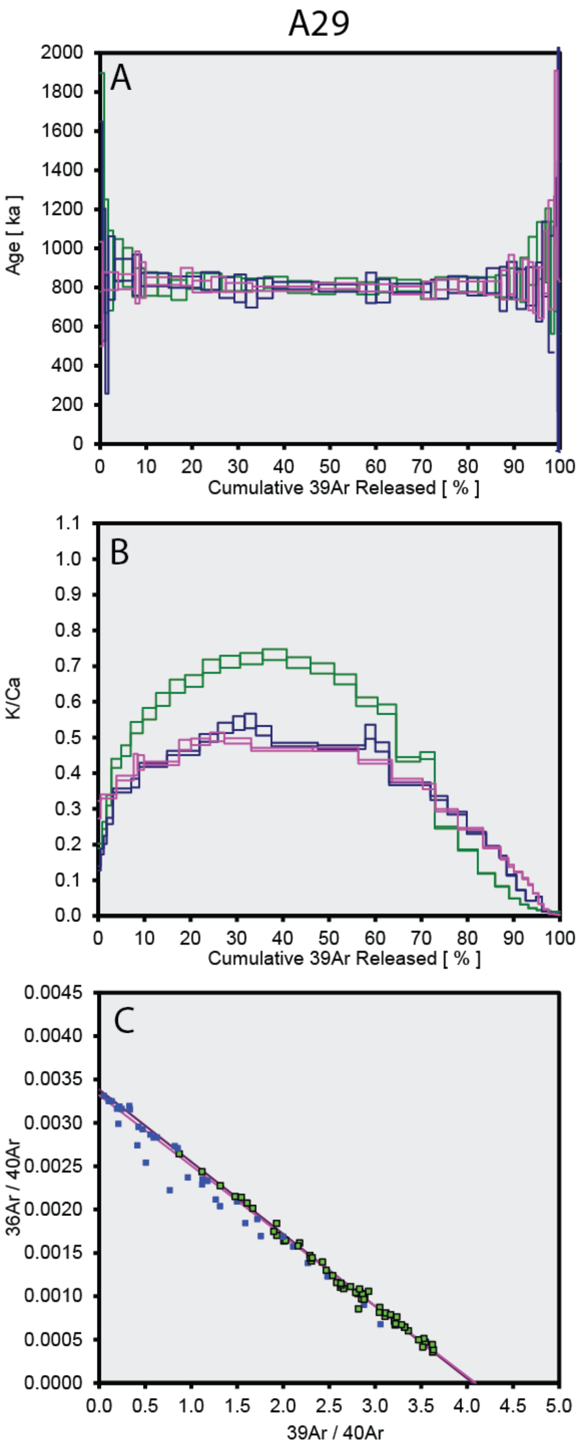

Figure B.9: The argon analysis of lava flow A29 (n=3). **(A)** The incremental heating plateau with age uncertainties reported at the 2σ confidence level. The plateau is flat for most analyses with some slight low temperature recoil effects seen within some spectrums. **(B)** The K/Ca curve for the incremental heating experiment. Samples display a saddled pattern indicating early degassing of some alteration components the ^{39}Ar(K) increases as the interstitial mesostatsis degasses. The ^{37}Ar(Ca) component increase towards the higher temperature steps as plagioclase and clinopyroxene components begin degassing. **(C)** The inverse isochron, whereby green squares represent points within the selected plateau and blue squares are excluded points from the heating plateau.

Table B.8: (Below) Incremental heating plateau results for flow A29.

Sample	Age (ka)	2σ	MSWD	40Ar/36Ar int	2σ
A29-Ar-1	799.7	6.5	0.56	304.2	28
A29-Ar-2	807.6	8.6	0.69	308	11
A29-Ar-3	812.2	8.5	0.47	297.4	5.7

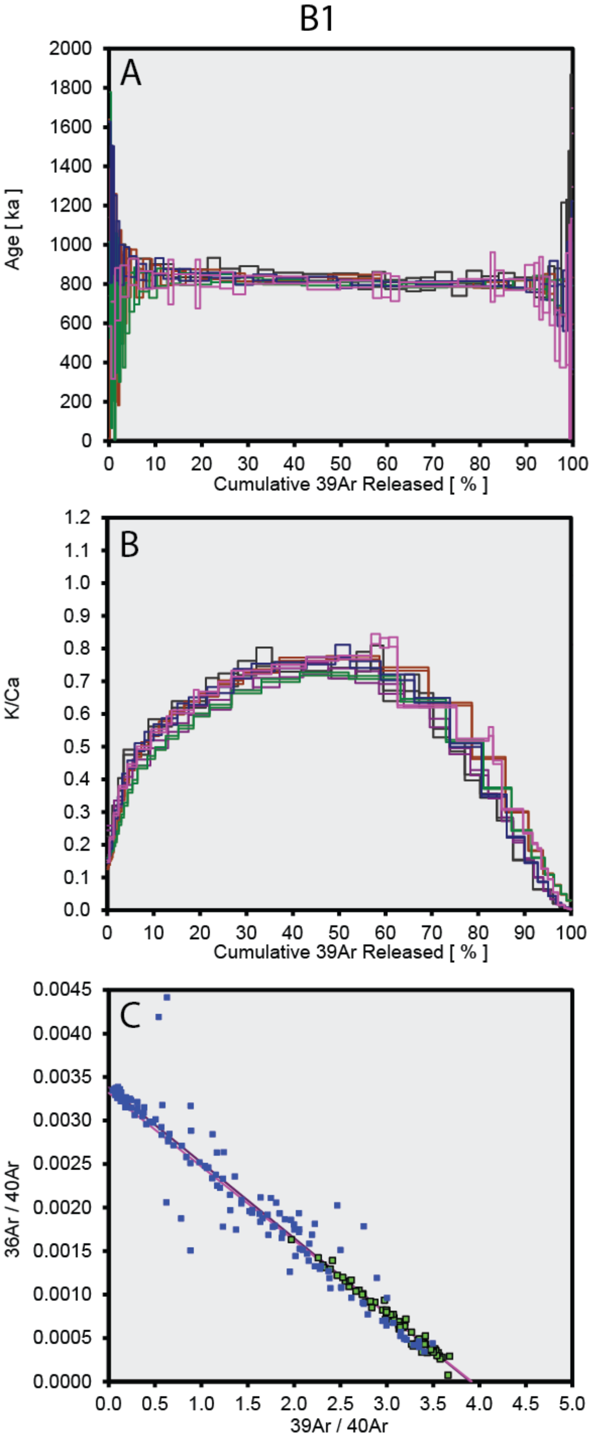

Figure B.10: The argon analysis of lava flow B1 (n=6). **(A)** The incremental heating plateau with age uncertainties reported at the 2σ confidence level. Some analyses had early heating steps that were excluded as they represent discordant incremental heating steps and are likely reflecting some partial loss of radiogenic ^{40}Ar through partial degassing. The spectrum becomes flat and concordant within the age plateau at the 2σ confidence interval. Some high temperature heating steps are also excluded due to high temperature ^{37}Ar(Ca) and ^{39}Ar(K) recoil. **(B)** The K/Ca curve for the incremental heating experiment. Samples display a saddled pattern indicating early degassing of some alteration components the ^{39}Ar(K) increases as the interstitial mesostatsis degasses. The ^{37}Ar(Ca) component increase towards the higher temperature steps as plagioclase and clinopyroxene components begin degassing. **(C)** The inverse isochron, whereby green squares represent points within the selected plateau and blue squares are excluded points from the heating plateau.

Table B.9: (Below) Incremental heating plateau results for flow B1.

Sample	Age (ka)	2σ	MSWD	40Ar/36Ar int	2σ
B1-Ar-1a	805.8	6	0.84	309.6	15
B1-Ar-1b	802.4	5.2	0.77	269.2	35
B1-Ar-2a	802.7	5	1.16	316.7	20
B1-Ar-2b	794.5	7.4	1.27	329.7	27
B1-Ar-4a	798.5	6.5	0.07	292.3	23
B1-Ar-4b	806.8	11.4	1.32	289.4	38

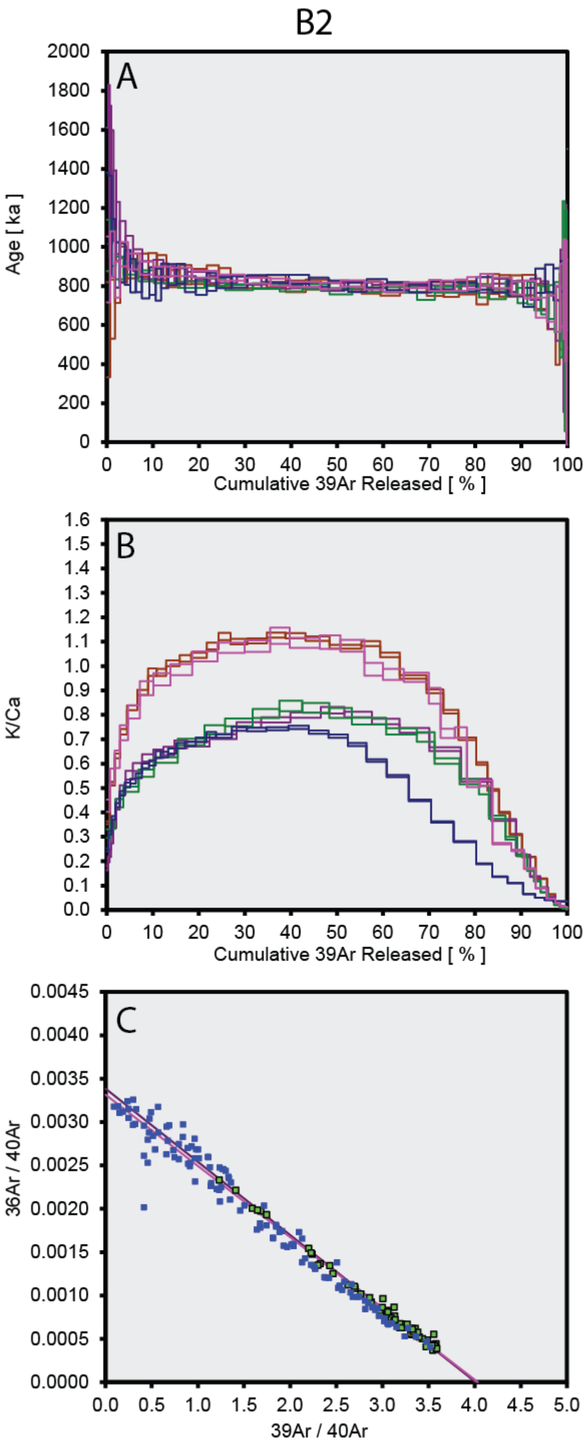

Figure B.11: The argon analysis of lava flow B2 (n=5). **(A)** The incremental heating plateau with age uncertainties reported at the 2σ confidence level. Early heating steps are excluded as they represent discordant incremental heating steps and are likely reflecting ^{39}Ar(K) recoil through the preferential degassing of fine-grained secondary (e.g. clay) phases that remain resident in the groundmass separates, even after the applied intense acid leaching protocol, but are resolved at higher temperatures and within the age plateau at the 2σ confidence interval. High temperature heating steps are also excluded due to high temperature ^{37}Ar(Ca) and ^{39}Ar(K) recoil. **(B)** The K/Ca curve for the incremental heating experiment. Samples display a saddled pattern indicating early degassing of some alteration components the ^{39}Ar(K) increases as the interstitial mesostatsis degasses. The ^{37}Ar(Ca) component increase towards the higher temperature steps as plagioclase and clinopyroxene components begin degassing. **(C)** The inverse isochron, whereby green squares represent points within the selected plateau and blue squares are excluded points from the heating plateau.

Table B.10: (Below) Incremental heating plateau results for flow B2.

Sample	Age (ka)	2σ	MSWD	40Ar/36Ar int	2σ
B2-Ar-2a	795	8.7	0.51	297.6	8.5
B2-Ar-2b	804.9	5.7	0.98	296	6.1
B2-Ar-3a	800.3	7.8	0.52	293.7	16.8
B2-Ar-3b	777	7.8	1.72	296.4	53
B2-Ar-4	793	6	0.82	292.9	14

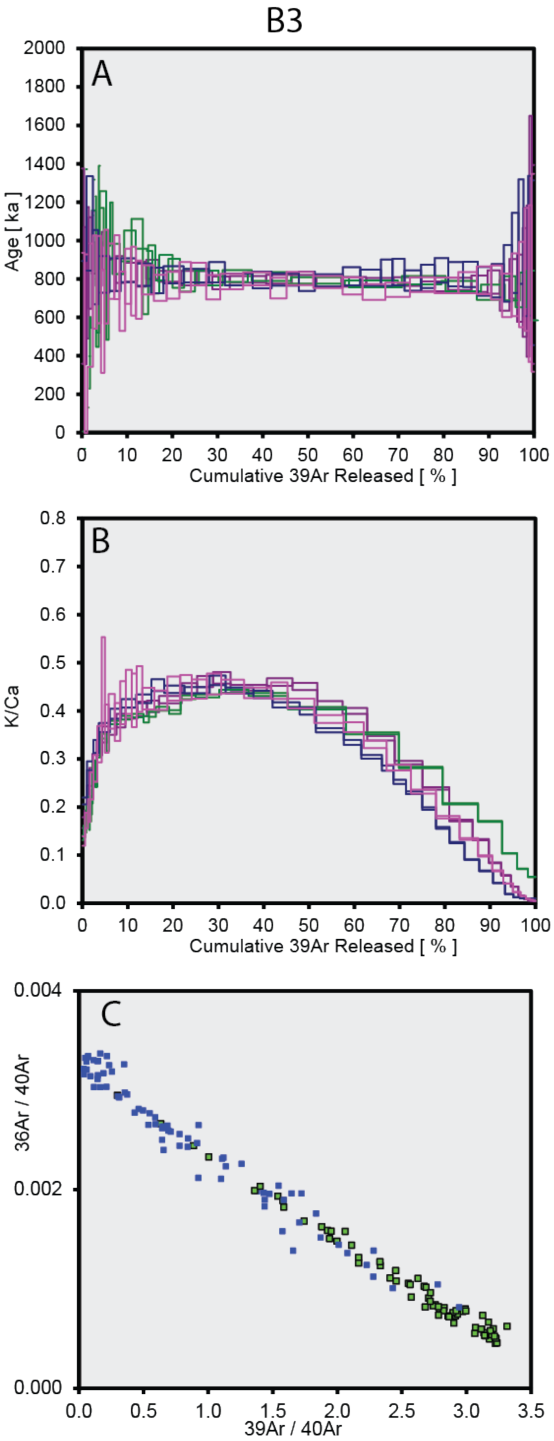

Figure B.12: The argon analysis of lava flow B3 (n=4). **(A)** The incremental heating plateau with age uncertainties reported at the 2σ confidence level. Early heating steps are excluded as they represent discordant incremental heating steps and are likely reflecting ^{39}Ar(K) recoil through the preferential degassing of fine-grained secondary (e.g. clay) phases that remain resident in the groundmass separates, even after the applied intense acid leaching protocol, but are resolved at higher temperatures and within the age plateau at the 2σ confidence interval. High temperature heating steps are also excluded due to high temperature ^{37}Ar(Ca) and ^{39}Ar(K) recoil. **(B)** The K/Ca curve for the incremental heating experiment. Samples display a saddled pattern indicating early degassing of some alteration components the ^{39}Ar(K) increases as the interstitial mesostatsis degasses. The ^{37}Ar(Ca) component increase towards the higher temperature steps as plagioclase and clinopyroxene components begin degassing. **(C)** The inverse isochron, whereby green squares represent points within the selected plateau and blue squares are excluded points from the heating plateau.

Table B.11: (Below) Incremental heating plateau results for flow B3. Sample B3-Ar-2 was excluded from the mean due to excess ^{40}Ar.

Sample	Age (ka)	2σ	MSWD	40Ar/36Ar int	2σ
B3-Ar-2	901.5	22.2	2.68	328.3	12
B3-Ar-3a	776.6	10.7	0.93	298.5	18
B3-Ar-3b	809	10.2	0.45	298.1	4.3
B3-Ar-4a	793.9	11.3	1.59	340.33	83
B3-Ar-4b	789.8	7.1	0.97	294.2	22

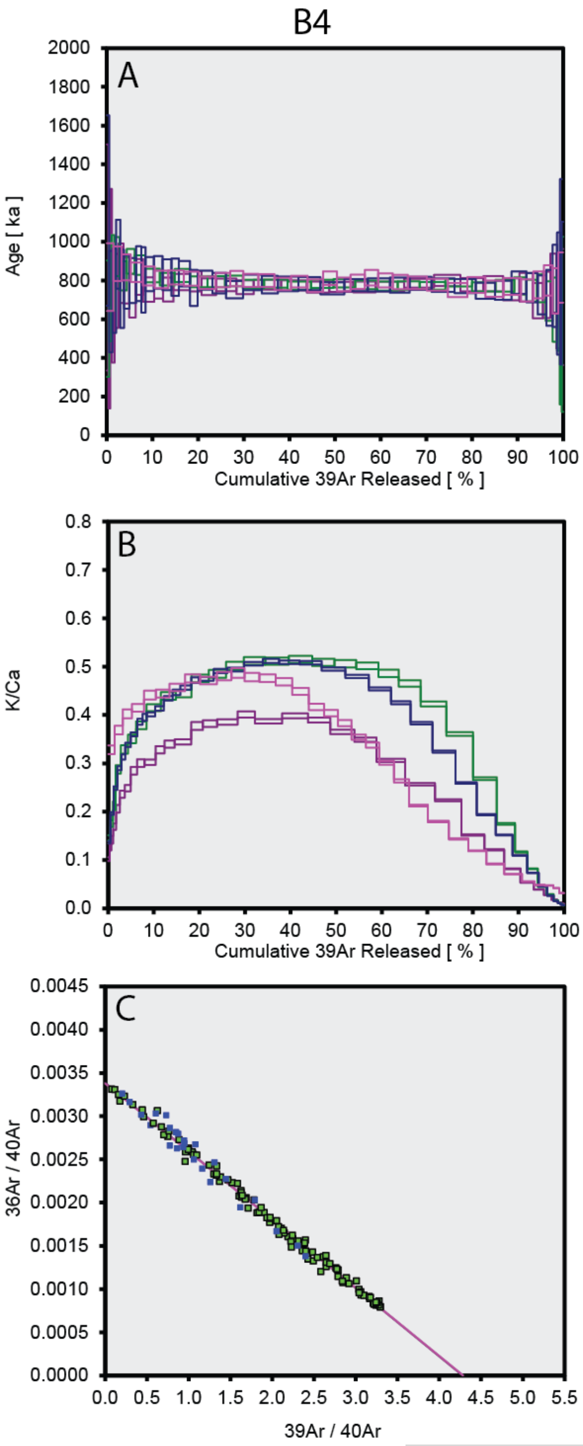

Figure B.13: The argon analysis of lava flow B4 (n=4). **(A)** The incremental heating plateau with age uncertainties reported at the 2σ confidence level. **(B)** The K/Ca curve for the incremental heating experiment. Samples display a saddled pattern indicating early degassing of some alteration components the ^{39}Ar(K) increases as the interstitial mesostatsis degasses. The ^{37}Ar(Ca) component increase towards the higher temperature steps as plagioclase and clinopyroxene components begin degassing. **(C)** The inverse isochron, whereby green squares represent points within the selected plateau and blue squares are excluded points from the heating plateau.

Table B.12: (Below) Incremental heating plateau results for flow B4.

Sample	Age (ka)	2σ	MSWD	40Ar/36Ar int	2σ
B4-Ar-2	790.7	7.4	0.88	292.5	6.4
B4-Ar-4a	778.4	9	0.73	297.8	5.1
B4-Ar-4b	779.9	6.1	0.55	297.2	16
B4-Ar-5	775.7	7.7	0.46	295.4	2.1

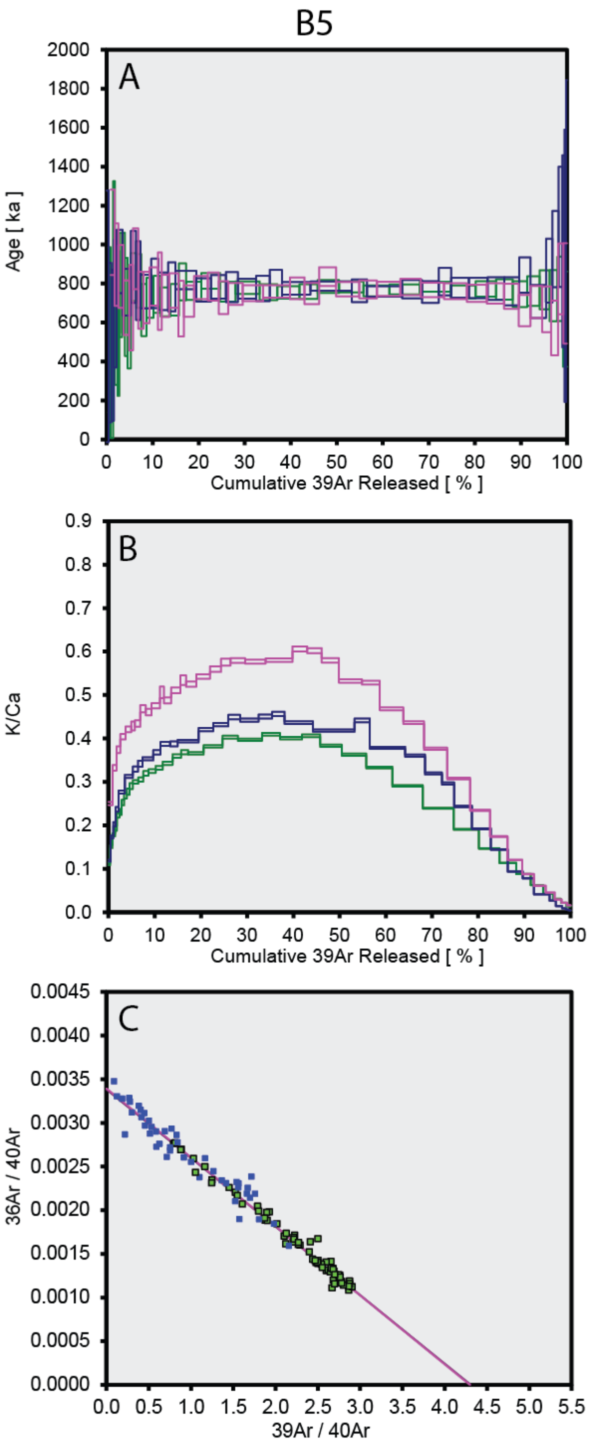

Figure B.14: The argon analysis of lava flow B5 (n=3). **(A)** The incremental heating plateau with age uncertainties reported at the 2σ confidence level. Early heating steps are excluded as they represent discordant incremental heating steps and are likely reflecting ^{39}Ar(K) recoil through the preferential degassing of fine-grained secondary (e.g. clay) phases that remain resident in the groundmass separates, even after the applied intense acid leaching protocol, but are resolved at higher temperatures and within the age plateau at the 2σ confidence interval.
High temperature heating steps are also excluded due to high temperature ^{37}Ar(Ca) and ^{39}Ar(K) recoil. **(B)** The K/Ca curve for the incremental heating experiment. Samples display a saddled pattern indicating early degassing of some alteration components the ^{39}Ar(K) increases as the interstitial mesostatsis degasses. The ^{37}Ar(Ca) component increase towards the higher temperature steps as plagioclase and clinopyroxene components begin degassing. **(C)** The inverse isochron, whereby green squares represent points within the selected plateau and blue squares are excluded points from the heating plateau.

Table B.13: (Below) Incremental heating plateau results for flow B5.

Sample	Age (ka)	2σ	MSWD	40Ar/36Ar int	2σ
B5-Ar-3a	764.3	10.5	0.77	279.06	19
B5-Ar-3b	778.3	10.5	0.48	299.4	8.8
B5-Ar-4	769.4	9.1	0.39	293.9	5

Table B.14: Summary of age determinations for each flow

		Age Spectrum								Total Fusion		Inverse Isochron Analyses			
Lava Flow	Sample Type	**Age ± 2σ (ka)**	^{39}Ar (%)	K/Ca	MSWD	P (%)	n steps	N al ste	N samples	**Age ± 2σ (ka)**	K/Ca	Age ± 2σ (ka)	^{40}Ar/ ^{36}Ar intercept	MSWD	P (%)
A12	Groundmass	**857.4 ± 3.5**	83	0.161	0.82	81	49	76	2	**849.3 ± 4.4**	0.462	854.4 ± 4.4	297.9 ± 2.14	0.73	92
A16	Groundmass	**816.1 ± 5.0**	62	0.062	0.89	60	22	70	2	**809.4 ± 6.2**	0.243	812.1 ± 10.1	297.8 ± 4.99	0.89	60
A22	Groundmass	**799.4 ± 4.3**	76	0.023	0.82	89	91	138	4	**802.2 ± 5.4**	0.204	802.2 ± 5.4	293.54 ± 2.76	0.81	91
A23	Groundmass	**800.9 ± 3.6**	53	0.206	0.88	68	41	98	3	**811.1 ± 3.6**	0.208	799.7 ± 9.3	296.95 ± 10	0.90	65
A24	Groundmass	**800.0 ± 3.6**	58	0.045	0.75	89	45	99	3	**810.4 ± 4.1**	0.222	799.6 ± 5.9	295.81 ± 2.91	0.77	87
A27	Groundmass	**795.1 ± 4.0**	80	0.044	0.52	100	85	139	4	**798.9 ± 5.4**	0.166	792.1 ± 5.6	297.34 ± 2.29	0.50	100
A28	Groundmass	**787.5 ± 3.0**	58	0.437	0.96	52	27	66	2	**796.2 ± 3.2**	0.386	782.7 ± 6.6	301.68 ± 7.57	0.90	61
A29	Groundmass	**805.1 ± 4.6**	82	0.075	0.66	98	59	96	3	**825.3± 6.6**	0.112	799.2 ± 6.3	301.34 ± 4.15	0.53	100
B1	Groundmass	**801.7 ± 2.9**	56	0.072	1.05	37	73	209	6	**808.7 ± 3.4**	0.216	798.4 ± 5.2	301.24 ± 7.05	1.02	43
B2	Groundmass	**793.7 ± 4.1**	51	0.218	1.74	0	58	177	5	**816.2 ± 3.6**	0.233	789 ± 5.7	301.66 ± 5.13	1.59	0
B3	Groundmass	**792.2 ± 4.8**	74	0.048	1.08	31	70	144	4	**791.4 ± 6.7**	0.138	788.9 ± 5.9	300.23 ± 3.82	1.01	31
B4	Groundmass	**781.3 ± 3.9**	90	0.071	0.96	98	113	139	4	**782.7 ± 4.7**	0.160	780.2 ± 5.1	296.02 ± 1.67	0.75	98
B5	Groundmass	**770.6 ± 5.9**	82	0.065	0.61	100	70	116	3	**769.0 ± 7.2**	0.155	772.5 ± 10.4	294.61 ± 4.22	0.61	100

‘Samp.’ stands for the total amount of samples analyzed.

MSWD is the mean-square of the weighted deviants.

P is the chi2 probability.

n steps’ represents the incremental heating steps used in the age calculation while ‘N total steps’ represents the total amount of steps analyzed.

‘Int’ is an abbreviation for intercept.

B.3: Supplementary information on paleomagnetic measurements and models

Table B.15: Paleomagnetic results for the Tahitian lava flows.

Lava	**Site**		**n**	**N**	**Directions**				**VGP**	
	Latitude	**Longitude**			**Dec**	**Inc**	**a95**	**ƙ**	**Lat**	**Long**
A4	-17.62818	-149.60110	3	3	187.4	-11.7	7.2	296.4	-70.6	287.3
A8	-17.6289	-149.60082	1	1	177.9	7.3	0.3	12037	-64.6	324.6
A9	-17.62908	-149.60112	3	3	170.3	11.9	6.5	364.8	-58.6	337.9
A10	-17.62905	-149.60107	4	4	173.8	10.1	9.2	100.3	-61.5	332.6
A11	-17.62918	-149.60115	3	3	171.6	6.5	5.1	576.3	-59.7	331.3
A12	-17.62927	-149.60128	3	3	179.8	37.5	4.5	741.3	-66	351.9
A13	-17.62935	-149.60138	3	3	169.3	18	17.9	48.7	-57.8	344.9
A14	-17.62950	-149.60148	3	3	181.9	-27.6	32.4	15.5	-67.4	283.2
A15	-17.62985	-149.60158	3	3	161.6	-5.9	22.9	30.1	-51.2	326.5
A16	-17.62997	-149.60160	3	2	166.2	2.1	42.4	36.8	-55.2	331.5
A21	-17.62977	-149.60100	2	2	47.9	31	37.4	46.8	55.3	241.7
A22	-17.62968	-149.60078	4	4	38.2	42.6	7.2	163.9	63.2	262.8
A23	-17.62968	-149.60078	2	2	7.9	-16.1	14.4	303.2	70.8	281.7
A24	-17.62958	-149.59982	4	4	73.4	-66.1	8.2	126.7	32.1	134
A27	-17.62930	-149.59883	4	4	172.9	-15.2	22.7	17.4	-60.8	308.3
A28	-17.62917	-149.59922	3	3	283.8	40.1	23.6	28.3	-3.2	23.2
A29	-17.62902	-149.59913	4	4	12.2	-3.8	5.3	305.9	72.4	281.9
B1	-17.62902	-149.59953	4	4	36.8	-2.1	35.6	7.6	64.3	219.9
B2	-17.62900	-149.59953	3	3	18.3	12.7	12.4	100	73.1	278.8
B3	-17.62897	-149.59958	3	3	7.3	-17.7	5.1	585.5	70.5	281.6
B4	-17.62897	-149.59858	2	1	346.1	-20	0.8	0	74.7	147
B5	-17.62897	-149.59858	2	2	7	-22.2	6.6	1429	80.9	259.4

'n' indicates the amount of samples that were collected and measured while 'N' represents the amount of samples used in measuring the site directions. The sampled lava flows are the same flows analyzed in Mochizuki et al., (2011).

B.3.1 Sediment smoothing model

We use a simple model to illustrate that rapid geomagnetic directional changes that take place on centennial-to-millennial timescales, as demonstrated by the Tahiti, Chile, La Palma, and Maui volcanic records, would appear smoothed in sedimentary records as a result of sampling method and post-depositional processes. The model uses the PDFs of observed ages of reversed (-90 to -45), transitional (-45 to 45) and normal (45 to 90) VGP latitudes from the four volcanic datasets (Figure 3.2) to create 1,000 possible volcanic records, uniformly sampled through time. These hypothetical volcanic records are then converted to hypothetical sedimentary records by applying a 5,000 year (6 sigma width) Gaussian filter (Figure B15).

Each iteration of the model uses a square wave of reversed VGP latitudes (-90° to -70°) and normal VGP latitudes (70° to 90°) randomly sampled from uniform distributions and run from 830 to 750 ka at time steps of 500 yrs. The switch from reversed to normal is randomly determined from a normal distribution of ages, as determined from sedimentary archives (773 ± 5 ka; Channell et al., 2010).

The decision to perturb the square wave at each time step is based on the sum PDF of all observations, normalized by the maximum probability. If the square wave is perturbed at that time step, a randomly sampled reverse (-90 to -70), transitional (-45 to 45), or normal (70 to 90) direction from a uniform distribution is assigned based on the relative probability of each respective PDF.

The 95% confidence interval for VGP latitude at each time step is calculated from the 1,000 iterations of hypothetical sedimentary (smoothed) records. We find that the general structure, timing, and uncertainty of the hypothetical sedimentary

VGP latitudes to be consistent with high-quality sedimentary records, especially given the ~5 kyr uncertainty in their astrochronologically tuned age models. This simple model, although not physically meaningful, demonstrates that given uncertainties related to chronologic, spatial/temporal coverage, and magnetic acquisition processes, volcanic and sedimentary archives are not in disagreement (Figure B16).

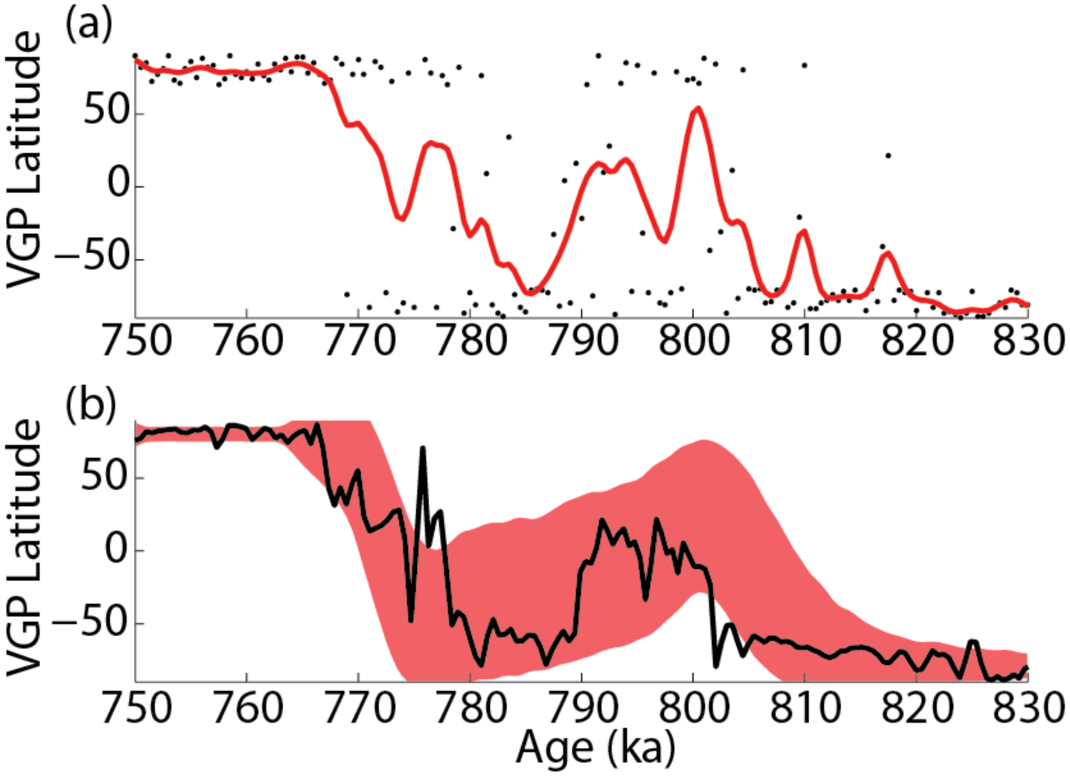

Figure B15: A simple model illustrates how volcanic and sedimentary records might record centennial to millennial scale variations of the geomagnetic field quite differently, in this example compared to the sedimentary VGP latitude reconstruction from the Indian Ocean (Figure 3.3; Valet et al, 2014) and its 95% confidence interval (black line with gray outline). A vertical red line at 773 ka is used to denote the age of the M-B reversal, as defined by astronomically tuned sedimentary records (Channell et al., 2010) **(a)** A single model run with a hypothetical volcanic record (black dots) of an instable field lasting 30 kyr (based on data from Figure 3.2 between 773 and 80 ka) while it transitions from fully reversed to fully normal. The modeled sedimentary record with an average sedimentation rate of 4.7 cm/year for latitude of 5.04° is shown in the smoothed red line. There is a good agreement between the model and the Indian Ocean sediment record, especially considering the 5 kyr uncertainty (Valet et al., 2014) in the observation's astrochronologic age model. **(b)** The 95% confidence interval of modeled sedimentary VGP latitudes from 1,000 model iterations (red shading) suggests that there is little disagreement in high-quality sedimentary and volcanic archives given uncertainties related to chronologic, spatial/temporal coverage, and magnetic acquisition processes that are largely dependent on sedimentation rates.

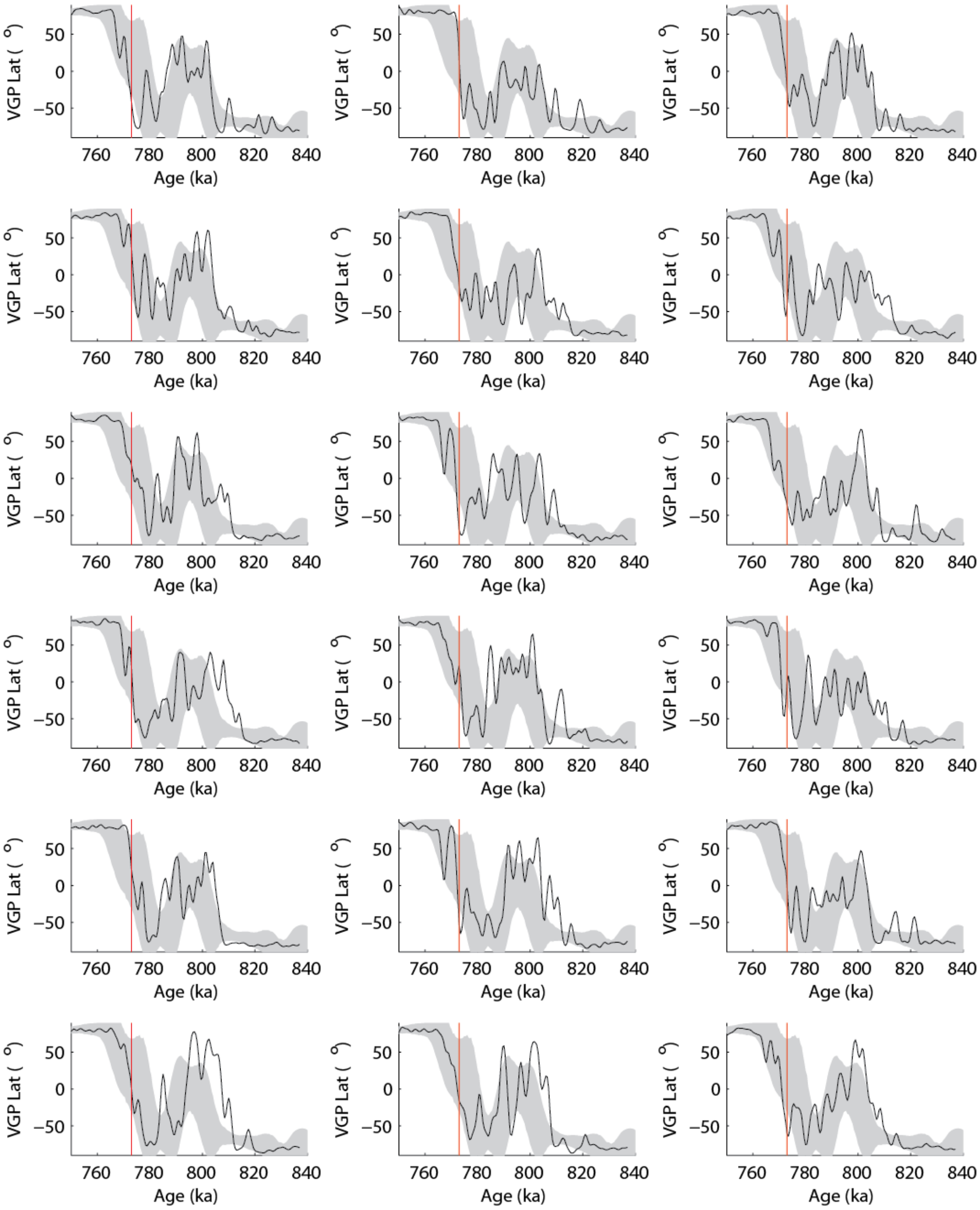

Figure B16: Eighteen random iterations from monte carlo runs selected model runs of hypothetical sedimentary records (black line; see supplementary text for discussion). A vertical red line at 773 ka is used to denote the age of the M-B reversal, as defined by astronomically tuned sedimentary records (Channell et al., 2010). For comparison, the 95% confidence interval (gray outline) of an Indian Ocean sedimentary record of the M-B reversal (Valet et al., 2014) is created by perturbing its age model by the 5 kyr uncertainty in its astrochronologic age model. Although no model matches the observation perfectly, we find many similarities that suggest volcanic and sedimentary records show centennial to millennial scale variations of the geomagnetic field quite differently, with lava flows recording discrete maximum directional states of temporary excursions and reversals in the field while sediments are recording a smoothed and muted signal of the same events that is inversely dependent on sedimentation rates.

B.4. References

Balbas, A., Koppers, A. A., Kent, D. V., Konrad, K., and Clark, P. U., 2016, Identification of the short-lived Santa Rosa geomagnetic excursion in lavas on Floreana Island (Galapagos) by 40Ar/39Ar geochronology: Geology, p. G37569. 37561.

Chauvin, A., Roperch, P., & Duncan, R. A. (1990). Records of geomagnetic reversals from volcanic islands of French Polynesia: 2. Paleomagnetic study of a flow sequence (1.2–0.6 Ma) from the island of Tahiti and discussion of reversal models. Journal of Geophysical Research: Solid Earth, 95(B3), 2727-2752.

Channell, J., Xuan, C., and Hodell, D., 2009, Stacking paleointensity and oxygen isotope data for the last 1.5 Myr (PISO-1500): Earth and Planetary Science Letters, v. 283, no. 1, p. 14-23.

Channell, J., Mazaud, A., Sullivan, P., Turner, S., and Raymo, M., 2002, Geomagnetic excursions and paleointensities in the Matuyama Chron at Ocean Drilling Program sites 983 and 984 (Iceland Basin): Journal of Geophysical Research: Solid Earth (1978–2012), v. 107, no. B6, p. EPM 1-1-EPM 1-14.

Koppers, A.A., 2002, ArArCALC—software for 40Ar/39Ar age calculations: Computers & Geosciences, v. 28, p. 605–619, doi:10.1016/S0098-3004(01)00095-4.

Koppers, A.A.P., Duncan, R.A., and Steinberger, B., 2004, Implications of a nonlinear 40Ar/39Ar age progression along the Louisville seamount trail for models of fixed and moving hot spots: Geochemistry Geophysics Geosystems, v. 5, Q06L02, doi:10.1029/2003GC000671.

Kuiper, K., Deino, A., Hilgen, F., Krijgsman, W., Renne, P., and Wijbrans, J., 2008, Synchronizing rock clocks of Earth history: science, v. 320, no. 5875, p. 500-504.

Laj, C., Guillou, H., & Kissel, C. 2014. Dynamics of the earth magnetic field in the 10–75 kyr period comprising the Laschamp and Mono Lake excursions: New results from the French Chaîne des Puys in a global perspective. Earth and Planetary Science Letters, 387, 184-197.

Lascu, I., Feinberg, J. M., Dorale, J. A., Cheng, H., and Edwards, R. L., 2016, Age of the Laschamp excursion determined by U-Th dating of a speleothem geomagnetic record from North America: Geology, v. 44, no. 2, p. 139-142.

Min, K., Mundil, R., Renne, P. R., and Ludwig, K. R., 2000, A test for systematic errors in 40 Ar/39 Ar geochronology through comparison with U/Pb analysis of a 1.1-Ga rhyolite: Geochimica et Cosmochimica Acta, v. 64, no. 1, p. 73-98.

Mochizuki, N., Oda, H., Ishizuka, O., Yamazaki, T., and Tsunakawa, H., 2011, Paleointensity variation across the Matuyama-Brunhes polarity transition: Observations from lavas at Punaruu Valley, Tahiti: Journal of Geophysical Research: Solid Earth (1978–2012), v. 116, no. B6.

Singer, B. S., Guillou, H., Jicha, B. R., Laj, C., Kissel, C., Beard, B. L., & Johnson, C. M. 2009. 40Ar/39Ar, K–Ar and 230 Th–238 U dating of the Laschamp excursion: A radioisotopic tie-point for ice core and climate chronologies. Earth and Planetary Science Letters, 286(1), 80-88.

Valet, J.-P., Bassinot, F., Bouilloux, A., Bourlès, D., Nomade, S., Guillou, V., Lopes, F., Thouveny, N., and Dewilde, F., 2014, Geomagnetic, cosmogenic and climatic changes across the last geomagnetic reversal from Equatorial Indian Ocean sediments: Earth and Planetary Science Letters, v. 397, p. 67-79.

Wang, H., and Kent, D.V., 2013, A paleointensity technique for multidomain igneous rocks: Geochemistry Geophysics Geosystems, v. 14, p. 4195–4213, doi:10.1002/ggge.20248.

Appendix C - ^{10}Be dating constraints on the interplay between the late-Pleistocene Cordilleran Ice Sheet and Missoula Floods

C.1 Site mean age determinations

When determining the age of each feature, three different methods of calculating the mean age and uncertainty were used depending on the number of samples per site, standard deviation of the boulder ages per site, and analytical uncertainties per boulder age. For sites restricted to a single age, the boulder age and external uncertainty (Lal and Stone time-dependent scaling scheme) are reported. In scenarios where the standard deviation of the distribution of ages at a single site is greater than the mean analytical uncertainty, an arithmetic mean was used for the age. Equation 1 shows how the uncertainty with the arithmetic mean was calculated:

Equation 1

$$\sigma = \sqrt{\left(\frac{Standard\ deviation}{\sqrt{n}}\right)^2 + \ (Production\ rate\ uncertainty)^2}$$

For samples where the standard deviation of the distribution of ages was less than the mean analytical uncertainty of the ages, an error weighted mean was calculated using the equation 2:

Equation 2

$$\mu = \frac{\Sigma \frac{x_i}{\sigma_i^2}}{\Sigma \frac{1}{\sigma_i^2}}$$

Where x_i represents the age of an individual boulder and σ_i represents the analytical uncertainty. The error-weighted uncertainty was calculated using the following equation:

Equation 3

$$\sigma = \sqrt{\left(\frac{1}{\sqrt{\Sigma \frac{1}{\sigma_i^2}}}\right)^2 + (\,production\ rate\ uncertainty)^2}$$

Table C1: Summary of sampled boulders

Sample ID	Latitude	Longitude	Elevation (m)	Sample Thickness (cm)	Shielding	10Be/9Be	[^{10}Be] atoms g^{-1}	AMS standard	10Be age (a)	Internal uncertainty (1s)	External uncertainty (1s)
WIT-12	47.66025	-119.61309	636	2	1	2.02938E-13	103087.194	07KNSTD	14809	506	881
WIT-13	47.64924	-119.65714	655	2	1	2.30559E-13	116409.873	07KNSTD	16434	501	943
WIT-15	47.64990	-119.65025	615	2	0.999	1.67637E-13	88408.6485	07KNSTD	12958	432	765
WIT-18	47.66525	-119.63387	635	2	0.999	2.03896E-13	102906.309	07KNSTD	14810	451	850
WIT-19	*47.66531*	*-119.63384*	*633*	*2*	*0.999*	*3.93539E-13*	*192681.286*	*07KNSTD*	*27580*	*583*	*1464*
CHLN-1	*47.85958*	*-120.02036*	*630*	*2*	*1*	*1.2027E-13*	*62725.3227*	*07KNSTD*	*9075*	*474*	*650*
CHLN-2	47.85951	-120.02119	629	2	1	1.96184E-13	94162.7666	07KNSTD	13595	570	875
CHLN-3	47.85949	-120.02130	633	2	1	1.92451E-13	99541.0121	07KNSTD	14341	464	838
BCR-01	47.16920	-119.97806	395	2	0.997	1.45846E-13	124724.711	07KNSTD	22195	717	1295
FAR-04	47.97075	-116.59628	162	2	1	1.98563E-13	104936.06	07KNSTD	13839	478	826
RAT-02	47.93709	-116.83388	796	2	0.999	2.09105E-13	110428.724	07KNSTD	13840	463	817
RAT-03	47.97075	-116.59628	791	2	0.999	2.34592E-13	118436.913	07KNSTD	14891	431	843
RAT-04	47.95984	-116.81949	790	2	1	2.61861E-13	133390.799	07KNSTD	16748	488	950
UWB-2	*47.20572*	*120.01204*	*190*	*2*	*1*	*1.47782E-13*	*105525.154*	*07KNSTD*	*22300*	*747*	*1317*
EPF-1	47.26265	-119.46025	344	2	1	1.93717E-13	82826.4278	07KNSTD	15245	485	887
EPF-2	47.26245	-119.46028	341	2	0.9928	1.3107E-13	81379.7786	07KNSTD	15126	561	927
EPF-3	47.26180	-119.45975	340	2	1	1.8226E-13	76428.7565	07KNSTD	14132	524	866
EPF-4	47.32695	-119.46948	371	2	1	2.36434E-13	79119.8247	07KNSTD	14210	440	820
MAT-9	46.71987	119.94468	162	2	0.999	8.48127E-14	62564.4086	07KNSTD	13894	983	1198
MAT-3	46.71450	-119.94356	155	2	1	7.60907E-14	1309494.8	07KNSTD	13472	717	975
WEN-3	47.39828	-120.27150	274	2	1	9.04434E-14	1575142.36	07KNSTD	11787	684	897
WEN-4	47.39861	-120.27170	274	2	0.9972	8.57476E-14	1494295.92	07KNSTD	14457	975	1208
WEN-5	47.39820	-120.27180	274	2	0.9997	1.11547E-13	1961731.32	07KNSTD	13267	649	918
WEN-6	47.49510	-120.34406	421	2	0.99961	1.97891E-13	3470846.8	07KNSTD	17039	595	1021
WEN-7	47.49600	-120.34360	433	2	0.9997	1.14031E-13	2009298.28	07KNSTD	17198	792	1154
WEN-8	47.49640	-120.34315	441	2	0.9995	1.34694E-13	2373550	07KNSTD	17429	794	1163
WEN-13	47.56591	-120.26270	235	2	0.99419	9.68374E-14	1691064.63	07KNSTD	14413	761	1039
WEN-14	47.56591	-120.26270	235	2	0.99419	1.37815E-13	2438904.24	07KNSTD	14604	662	973
WAL-1	46.04585	-118.9619	341	2	1			07KNSTD	17206	846	1189

Italic values represent data not used in site age determinations due to inheritance or boulder post-depostional movement

Table C.2: Site mean ages

Site	Site Age	Site Age Uncertainty
	ka	ka (1σ)
Withrow Moraine+	14.8	1.0
Chelan Moraine+	14.0	0.8
Babcock Ridge◊	22.2	1.3
S. Lake Pend Oreille◊	13.8	0.8
Spirit Lake Ripples+	15.2	1.1
Ephrata Fan+	14.7	0.8
Mattawa Fan*	13.6	0.7
Pangborn Bar+	13.2	1.0
Wenatchee Rafted*	17.2	0.8
Wenatchee Bar*	14.5	0.7
Wallula Gap◊	17.2	1.2

+Indicate arithmetic mean and error (Equation 1, section C.1)

◊Indicate single sample value.

*Indicate error weighted mean and uncertainty (Equations 2 and 3, section C.1)

Table C.3: Procedural blank ^{10}Be data.

Blank No.	Sample ID	Carrier Added (g)[a]	^{10}Be/^{9}Be ± 1σ (10^{-15})	[^{10}Be] ± 1σ (10^{3} atoms)[b]	AMS Std[c]
7	201501608	0.8615	0.79 ± 0.32	16.3 ± 6.7	07KNSTD
8	201501943	0.8753	0.77 ± 0.26	16.1 ± 5.4	07KNSTD
9	201501944	0.8752	0.76 ± 0.26	15.8 ± 5.4	07KNSTD
10	201503085	0.8748	0.40 ± 0.46	8.3 ± 9.6	07KNSTD
11	201503095	0.8775	0.74 ± 0.40	15.6 ± 8.3	07KNSTD
12	201600931	0.8710	1.26 ± 0.45	26.3 ± 9.3	07KNSTD
13	201600938	0.8814	0.80 ± 0.30	16.9 ± 6.4	07KNSTD

[a] Carrier ^{9}Be concentration is 358 ppm.

[b] Total ^{10}Be (in atoms) in each procedural blank.

[c] AMS standard which ratios and concentrations are measured. ^{10}Be/^{9}Be ratio is 2.85×10^{-12}.

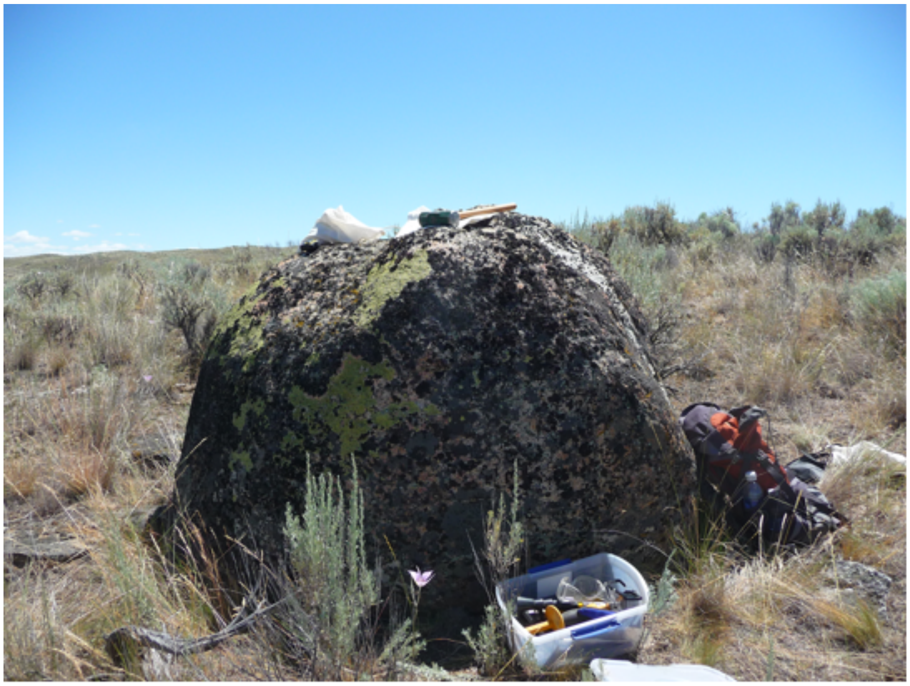

Figure C1: Withrow Moraine Sample: WIT-12
^{10}Be age: 14809 ± 506 (years; internal error; 2σ)
Location: Moses Coulee
Latitude: 47.66025
Longitude: -119.61309
Elevation: 636 m
Boulder Height: 1.4 m
Lithology: Granite
Shielding: none

Figure C.2: Withrow Moraine Sample: WIT-13
^{10}Be age: 16434 ± 501 (years; internal error; 2σ)
Location: Moses Coulee
Latitude: 47.64924
Longitude: -119.65714
Elevation: 655 m
Boulder Height: 1.05 m
Lithology: Granite
Shielding: none

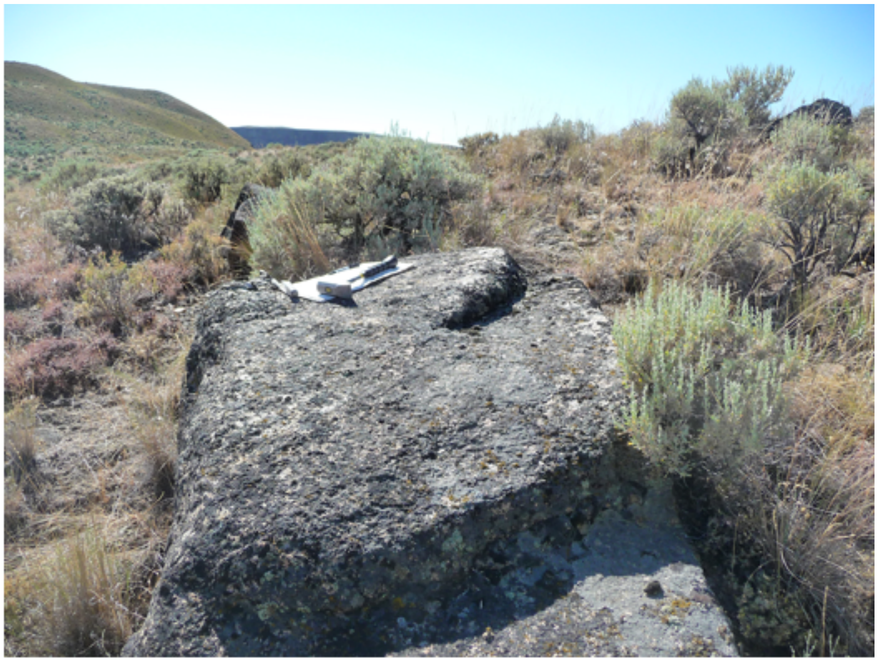

Figure C.3: Withrow Moraine Sample: WIT-15
^{10}Be age: 12958 ± 432 (years; internal error; 2σ)
Location: Moses Coulee
Latitude: 47.6499
Longitude: -119.65025
Elevation: 615 m
Boulder Height: 0.6 m
Lithology: Granite
Shielding: none

Figure C.4: Withrow Moraine Sample: WIT-18
^{10}Be age: 14810 ± 451 (years; internal error; 2σ)
Location: Moses Coulee
Latitude: 47.66525
Longitude: -119.63387
Elevation: 635 m
Boulder Height: 0.6 m
Lithology: Granite
Shielding: none

Figure C.5: Chelan Moraine Sample: CHLN-2
^{10}Be age: 13595 ± 570 (years; internal error; 2σ)
Location: Chelan Moraine
Latitude: 47.85951
Longitude: -120.02119
Elevation: 629 m
Boulder Height: 0.6 m
Lithology: Pegmatitic Granite
Shielding: none

Figure C.6: Chelan Moraine Sample: CHLN-3
^{10}Be age: 14341 ± 464 (years; internal error; 2σ)
Location: Chelan Moraine
Latitude: 47.85949
Longitude: -120.0213
Elevation: 633 m
Boulder Height: 1.0 m
Lithology: Granodiorite
Shielding: none

Figure C.7: Babcock Ridge Sample: BCR-1
^{10}Be age: 14341 ± 464 (years; internal error; 2σ)
Location: Babcock Ridge
Latitude: 47.169201
Longitude: -119.97806
Elevation: 395 m
Boulder Height: 1.0 m
Lithology: Granite
Shielding: none

Figure C.8: S. Lake Pend Oreille Moraine Sample: FAR-4
^{10}Be age: 13839 ± 478 (years; internal error; 2σ)
Location: S. Lake Pend Oreille
Latitude: 47.97075
Longitude: -116.59628
Elevation: 734 m
Boulder Height: 0.9 m
Lithology: Granite
Shielding: none

Figure C.9: Spirit Lake Ripples Sample: RAT-2
^{10}Be age: 13840 ± 463 (years; internal error; 2σ)
Location: Spirit Lake Ripples
Latitude: 47.93709
Longitude: -116.83388
Elevation: 796 m
Boulder Height: 1.5 m
Lithology: Granite
Shielding: none

Figure C.10: Spirit Lake Ripples Sample: RAT-3
^{10}Be age: 14891 ± 431 (years; internal error; 2σ)
Location: Spirit Lake Ripples
Latitude: 47.97075
Longitude: -116.59628
Elevation: 791 m
Boulder Height: 1.3 m
Lithology: Granite
Shielding: none

Figure C.11: Spirit Lake Ripples Sample: RAT-4
^{10}Be age: 16748 ± 488 (years; internal error; 2σ)
Location: Spirit Lake Ripples
Latitude: 47.95984
Longitude: -116.81949
Elevation: 790 m
Boulder Height: 1.4 m
Lithology: Granite
Shielding: none

Figure C.12: Ephrata Fan Sample: EPF-1
^{10}Be age: 15245 ± 485 (years; internal error; 2σ)
Location: Ephrata Fan
Latitude: 47.26265
Longitude: -119.46025
Elevation: 344 m
Boulder Height: 1.6 m
Lithology: Granite
Shielding: none

Figure C.13: Ephrata Fan Sample: EPF-2
^{10}Be age: 15126 ± 561 (years; internal error; 2σ)
Location: Ephrata Fan
Latitude: 47.26245
Longitude: -119.46028
Elevation: 341 m
Boulder Height: 1.4 m
Lithology: Granite
Shielding: none

Figure C.14: Ephrata Fan Sample: EPF-3
^{10}Be age: 14132 ± 524 (years; internal error; 2σ)
Location: Ephrata Fan
Latitude: 47.2618
Longitude: -119.45975
Elevation: 340 m
Boulder Height: 1.2 m
Lithology: Granite
Shielding: none

Figure C.15: Ephrata Fan Sample: EPF-4
^{10}Be age: 14210 ± 440 (years; internal error; 2σ)
Location: Ephrata Fan
Latitude: 47.32695
Longitude: -119.46948
Elevation: 371 m
Boulder Height: 1.2 m
Lithology: Granite
Shielding: none

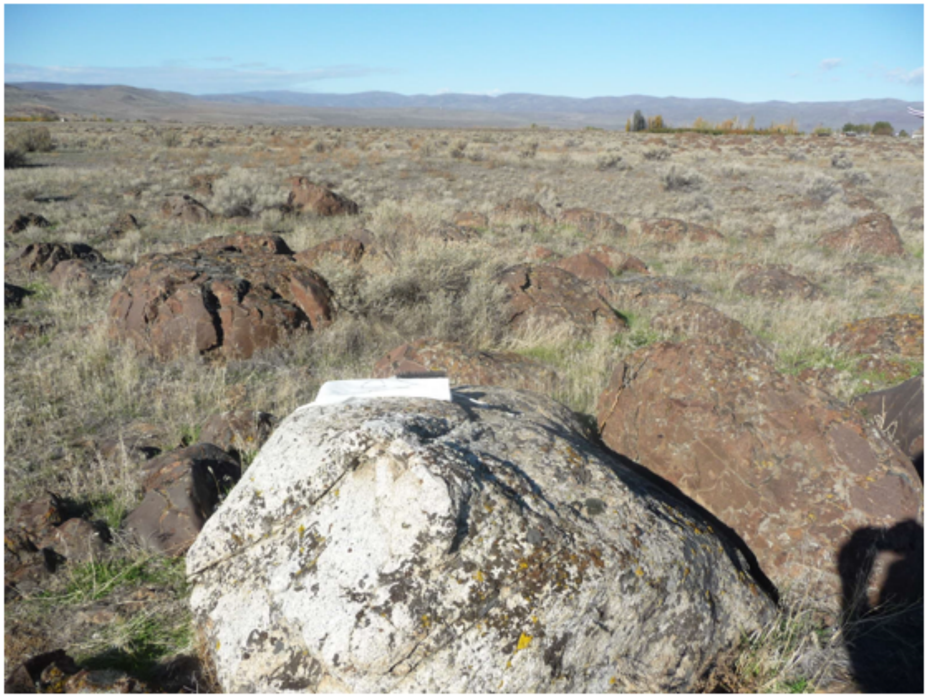

Figure C.16: Mattawa Fan Sample: MAT-9
^{10}Be age: 13894 ± 983 (years; internal error; 2σ)
Location: Mattawa Fan
Latitude: 46.71987
Longitude -119.94468
Elevation: 162 m
Boulder Height: 0.8 m
Lithology: Granite
Shielding: none

Figure C.17: Mattawa Fan Sample: MAT-3
^{10}Be age: 13894 ± 983 (years; internal error; 2σ)
Location: Mattawa Fan
Latitude: 46.7145
Longitude -119.94356
Elevation: 155 m
Boulder Height: 1.1 m
Lithology: Gneiss
Shielding: none

Figure C.18: East Wenatchee Sample: WEN-3
^{10}Be age: 11787 ± 684 (years; internal error; 2σ)
Location: East Wenatchee
Latitude: 47.39828
Longitude -120.2715
Elevation: 274 m
Boulder Height: 0.7 m
Lithology: Granite
Shielding: none

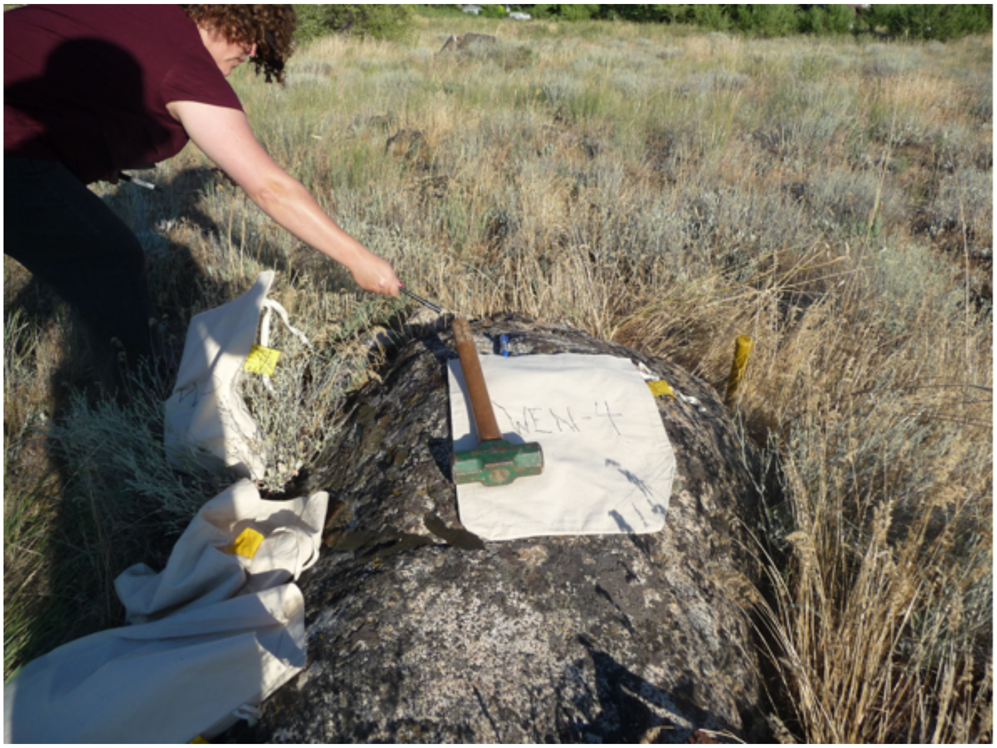

Figure C.19: East Wenatchee Sample: WEN-4
^{10}Be age: 14457 ± 975 (years; internal error; 2σ)
Location: East Wenatchee
Latitude: 47.39861
Longitude -120.2717
Elevation: 274 m
Boulder Height: 0.4 m
Lithology: Granite
Shielding: none

Figure C.20: East Wenatchee Sample: WEN-5
^{10}Be age: 13267 ± 649 (years; internal error; 2σ)
Location: East Wenatchee
Latitude: 47.3982
Longitude -120.2718
Elevation: 274 m
Boulder Height: 0.3 m
Lithology: Granite
Shielding: none

Figure C.21: Wenatchee Rafted Sample: WEN-6
^{10}Be age: 17039 ± 595 (years; internal error; 2σ)
Location: Northwest Wenatchee
Latitude: 47.49510
Longitude -120.34406
Elevation: 421 m
Boulder Height: 1.2 m
Lithology: Granodiorite
Shielding: none

Figure C.22: Wenatchee Rafted Sample: WEN-7
^{10}Be age: 17198 ± 792 (years; internal error; 2σ)
Location: Northwest Wenatchee
Latitude: 47.49600
Longitude -120.34360
Elevation: 433 m
Boulder Height: 0.4 m
Lithology: Granodiorite
Shielding: none

Figure C.23: Wenatchee Rafted Sample: WEN-8
^{10}Be age: 17429 ± 794 (years; internal error; 2σ)
Location: Northwest Wenatchee
Latitude: 47.49640
Longitude -120.34315
Elevation: 441 m
Boulder Height: 1 m
Lithology: Granodiorite
Shielding: none

Figure C.24: Wenatchee Bar Sample: WEN-13
^{10}Be age: 14413 ± 761 (years; internal error; 2σ)
Location: Wenatchee Bar
Latitude: 47.56591
Longitude -120.26270
Elevation: 235 m
Boulder Height: 1.5 m
Lithology: Granite
Shielding: none

Figure C.25: Wenatchee Bar Sample: WEN-14
^{10}Be age: 14604 ± 662 (years; internal error; 2σ)
Location: Wenatchee Bar
Latitude: 47.56591
Longitude -120.26270
Elevation: 235 m
Boulder Height: 2 m
Lithology: Granite
Shielding: none

Figure C.26: Wallula Gap Ice Rafted Sample: WAL-1
^{10}Be age: 17200 ± 846 (years; internal error; 2σ)
Location: Wallula Gap
Latitude: 46.04585
Longitude -118.96192
Elevation: 341 m
Boulder Height: 0.9 m
Lithology: Granite
Shielding: none